

Surface Activity and Bulk Defect Chemistry of Solid Oxide Fuel Cell Cathodes

Thesis by
Robert Ezra Usiskin

In Partial Fulfillment of the Requirements for the Degree of
Doctor of Philosophy



CALIFORNIA INSTITUTE OF TECHNOLOGY

Pasadena, California

2015

(Defended July 24, 2014)

Acknowledgments

I owe thanks to a number of collaborators who made important contributions to this work. Shingo Maruyama prepared several initial samples for the scanning impedance probe. Chris Kucharczyk turned my Matlab data reduction routine from a functional tool into a tour de force. Tim Fister and Kee-Chul Chang at Argonne National Laboratory provided invaluable support for the synchrotron measurements. Richard Wang helped with the SCN measurements.

I'm grateful to the Resnick Sustainability Institute at Caltech for the fellowship they provided me and for the many interesting people they helped bring together. Additional funding was provided by the National Science Foundation, the California Institute of Technology Summer Undergraduate Research Fellowship program, and the National Central University of Taiwan.

Many thanks to my research advisor Sossina Haile for sharing her scientific talent and judgment and for being such an eminently reasonable advisor. Northwestern will be lucky to have you.

I dedicate this thesis to my parents, Zalman and Karen Usiskin. This work would never have happened without their devotion and support and the high value they placed on intellectual excellence. I love you, Mom and Dad.

Abstract

In the first half of this thesis, a new robotic instrument called a *scanning impedance probe* is presented that can acquire electrochemical impedance spectra in automated fashion from hundreds of thin film microelectrodes with systematically varied properties. Results from this instrument are presented for three catalyst compositions that are commonly considered for use in state-of-the-art solid oxide fuel cell cathodes. For $(\text{La}_{0.8}\text{Sr}_{0.2})_{0.95}\text{MnO}_{3+\delta}$ (LSM), the impedance spectra are well fit by a through-the-film reaction pathway. Transport rates are extracted, and the surface activity towards oxygen reduction is found to be correlated with the number of exposed grain boundary sites, suggesting that grain boundaries are more surface-active than grains. For $\text{La}_{0.5}\text{Sr}_{0.5}\text{CoO}_{3-\delta}$ (LSC), the surface activity degrades $\sim 50\times$ initially and then stabilizes at a comparable activity to that of previously measured $\text{Ba}_{0.5}\text{Sr}_{0.5}\text{Co}_{0.8}\text{Fe}_{0.2}\text{O}_{3-\delta}$ films. For $\text{Sr}_{0.06}\text{Nb}_{0.06}\text{Bi}_{1.87}\text{O}_3$ (SNB), an example of a doped bismuth oxide, the activity of the metal-SNB boundary is measured.

In the second half of this thesis, $\text{SrCo}_{0.9}\text{Nb}_{0.1}\text{O}_{3-\delta}$ is selected as a case study of perovskites containing Sr and Co, which are the most active oxygen reduction catalysts known. Several bulk properties are measured, and synchrotron data are presented that provide strong evidence of substantial cobalt-oxygen covalency at high temperatures. This covalent bonding may be the underlying source of the high surface activity.

Table of Contents

CHAPTER 1 OVERVIEW	1
1.1 SUMMARY.....	1
1.2 WHY STUDY SOLID OXIDE FUEL CELL (SOFC) MATERIALS?.....	1
1.3 WHY STUDY THIN FILMS OF SOCF CATALYSTS?.....	2
1.4 WHY STUDY BULK DEFECT CHEMISTRY?.....	5
1.5 WHY FOCUS ON THE BULK DEFECT CHEMISTRY OF $\text{SrCo}_{0.9}\text{Nb}_{0.1}\text{O}_{3-\delta}$?.....	7
CHAPTER 2 HIGH THROUGHPUT CHARACTERIZATION OF $(\text{La}_{0.8}\text{Sr}_{0.2})_{0.95}\text{MnO}_{3+\delta}$ THIN FILM MICROELECTRODES.....	8
2.1 INTRODUCTION	8
2.2 OVERVIEW OF THE SCANNING IMPEDANCE PROBE.....	11
2.3 EXPERIMENTAL PROCEDURES.....	12
2.4 RESULTS OF PHYSICAL CHARACTERIZATION	15
2.5 RESULTS OF ELECTROCHEMICAL CHARACTERIZATION.....	20
2.6 DISCUSSION	36
2.7 CONCLUSION.....	38
CHAPTER 3 HIGH THROUGHPUT CHARACTERIZATION OF TWO OTHER MATERIAL SYSTEMS: $\text{La}_{0.5}\text{Sr}_{0.5}\text{CoO}_{3+\delta}$ AND PLATINUM - $\text{Sr}_{0.06}\text{Nb}_{0.06}\text{Bi}_{1.87}\text{O}_3$.....	52
3.1 SUMMARY.....	52
3.2 TWO MATERIAL SYSTEMS	52
3.2.1 $\text{La}_{0.5}\text{Sr}_{0.5}\text{CoO}_3$	53
3.2.2 $\text{Sr}_{0.06}\text{Nb}_{0.06}\text{Bi}_{1.87}\text{O}_3$	54
3.3 EXPERIMENTAL DETAILS.....	56

3.3.1	<i>Target preparation</i>	56
3.3.2	<i>Film preparation</i>	56
3.3.3	<i>Impedance characterization</i>	57
3.4	ELECTROCHEMICAL MODELS.....	58
3.5	LA _{0.5} SR _{0.5} CO ₃ RESULTS.....	60
3.5.1	<i>Structural characterization</i>	60
3.5.2	<i>Impedance data</i>	65
3.6	SR _{0.06} NB _{0.06} BI _{1.87} O ₃ RESULTS.....	73
3.6.1	<i>Structural characterization</i>	73
3.6.2	<i>Impedance spectra</i>	74
3.7	CONCLUSIONS.....	79
CHAPTER 4 MORE DETAIL ABOUT THE SCANNING IMPEDANCE PROBE.....		82
4.1	SUMMARY.....	82
4.2	PARALLEL CHARACTERIZATION.....	82
4.3	PARALLEL FABRICATION.....	84
4.4	SCANNING IMPEDANCE PROBE: DETAILS.....	88
4.4.1	<i>Mechanical</i>	88
4.4.2	<i>Thermal</i>	90
4.4.3	<i>Gas Control</i>	92
4.4.4	<i>Electronic</i>	93
4.4.5	<i>Software</i>	93
4.5	SOME OBSTACLES TO OBTAINING GOOD DATA, AND HOW TO OVERCOME THEM.....	94
4.5.1	<i>Tip Cooling</i>	94
4.5.2	<i>Tip scratching</i>	96

4.5.3	<i>Electronic noise and artifacts</i>	97
4.5.4	<i>Contamination</i>	99
4.5.5	<i>Sheet resistance</i>	99
CHAPTER 5 BULK PROPERTIES OF SCN		101
5.1	SUMMARY.....	101
5.2	WHY STUDY THE BULK DEFECT CHEMISTRY OF $\text{SrCo}_{0.9}\text{Nb}_{0.1}\text{O}_{3-\Delta}$ (SCN)?	101
5.3	EXPERIMENTAL DETAILS.....	102
5.4	RESULTS AND DISCUSSION	104
5.5	CONCLUSIONS.....	115
CHAPTER 6 ELECTRONIC BEHAVIOR OF $\text{SrCo}_{0.9}\text{Nb}_{0.1}\text{O}_{3-\delta}$		117
6.1	SUMMARY.....	117
6.2	BACKGROUND.....	117
6.3	EXPERIMENTAL DETAILS.....	119
6.3.1	<i>Synthesis</i>	119
6.3.2	<i>Quenching</i>	120
6.3.3	<i>Initial characterization</i>	121
6.3.4	<i>X-ray absorption spectroscopy</i>	121
6.3.5	<i>Non-resonant inelastic x-ray scattering</i>	122
6.4	RESULTS AND DISCUSSION	124
6.4.1	<i>Quenching</i>	124
6.4.2	<i>X-ray photoelectron spectra</i>	127
6.4.3	<i>X-ray absorption fine structure</i>	128
6.4.4	<i>Non-resonant inelastic x-ray scattering</i>	132
6.5	DISCUSSION	135

6.5.1 Appendix: $La_{0.6}Sr_{0.4}FeO_{3-\delta}$137

List of Figures

FIGURE 2.1. SCHEMATIC OF THE TEST CONFIGURATION IN THE SCANNING IMPEDANCE PROBE. DIMENSIONS ARE NOT TO SCALE.	11
FIGURE 2.2. X-RAY DIFFRACTION PATTERNS ACQUIRED FROM VARIOUS REGIONS OF TWO $(\text{La}_{0.8}\text{Sr}_{0.2})_{0.95}\text{MnO}_{3+\Delta}$ THIN FILM LIBRARIES: (A) LIBRARY #1, 30 - 300 NM THICKNESS, 650 °C GROWTH TEMPERATURE, 10 MTORR O_2 GROWTH PRESSURE, 1 HZ LASER PULSE RATE. (B) LIBRARY #3, 135 NM THICKNESS, 555 - 725 °C GROWTH TEMPERATURE, 30 MTORR O_2 GROWTH PRESSURE, 5 HZ LASER PULSE RATE. THE ORIENTATION OF EACH LSM REFLECTION IS INDICATED. REFLECTIONS MARKED WITH AN ASTERISK ARE FROM THE YSZ SUBSTRATE.....	16
FIGURE 2.3. TYPICAL LIBRARY OF $(\text{La}_{0.8}\text{Sr}_{0.2})_{0.95}\text{MnO}_{3+\Delta}$ THIN FILM MICROELECTRODES GROWN ON A 5 MM X 10 MM $\text{Y}_{0.15}\text{Zr}_{1.85}\text{O}_{1.93}$ SUBSTRATE. LEFT: SCHEMATIC LAYOUT. RIGHT: OPTICAL PHOTO OF LIBRARY #1 DURING IMPEDANCE MEASUREMENTS.....	17
FIGURE 2.4. ATOMIC FORCE MICROGRAPHS ACQUIRED AFTER PATTERNING FROM A THICKNESS LIBRARY OF $(\text{La}_{0.8}\text{Sr}_{0.2})_{0.95}\text{MnO}_{3+\Delta}$ MICROELECTRODES (LIBRARY #1, UNIFORM 650 °C GROWTH TEMPERATURE). THE CORRESPONDING THICKNESS AND ROOT-MEAN-SQUARED ROUGHNESS ARE LISTED UNDER EACH MICROGRAPH.	18
FIGURE 2.5. ATOMIC FORCE MICROGRAPHS ACQUIRED AFTER PATTERNING FROM A GROWTH TEMPERATURE LIBRARY OF $(\text{La}_{0.8}\text{Sr}_{0.2})_{0.95}\text{MnO}_{3+\Delta}$ MICROELECTRODES (LIBRARY #3, UNIFORM 135 NM THICKNESS). THE CORRESPONDING GROWTH TEMPERATURE AND ROOT-MEAN-SQUARED ROUGHNESS ARE LISTED UNDER EACH MICROGRAPH.	19
FIGURE 2.6. FIB-SEM CROSS-SECTION ACQUIRED FROM A GROWTH TEMPERATURE LIBRARY OF $(\text{La}_{0.8}\text{Sr}_{0.2})_{0.95}\text{MnO}_{3+\Delta}$ FILMS (LIBRARY #3) AFTER IMPEDANCE TESTING. THE SAMPLE WAS COATED WITH CONDUCTIVE AND PROTECTIVE LAYERS OF CARBON AND PLATINUM PRIOR TO FIB MILLING TO FACILITATE IMAGING. THIS IMAGE WAS ACQUIRED USING A TILT ANGLE OF 52° OFF NORMAL.	20
FIGURE 2.7. SCHEMATIC OF A THROUGH-THE-FILM REACTION PATHWAY.	21

FIGURE 2.8. EQUIVALENT CIRCUIT CORRESPONDING TO THE REACTION PATHWAY SHOWN IN FIGURE 2.7.	
FIGURE 2.9. TYPICAL IMPEDANCE SPECTRA (A), ZOOMED VIEW OF THE SAME SPECTRA (B), AND GAIN/PHASE PLOTS (C, D) PLOTS ACQUIRED FROM $(\text{La}_{0.8}\text{Sr}_{0.2})_{0.95}\text{MnO}_{3+\Delta}$ MICROELECTRODES. SPECIFIC PARAMETERS FOR THESE SPECTRA: LIBRARY #1, 200 MM DIAMETER, 192 NM THICKNESS, MEASURED AT ~ 710 °C OVER THE FREQUENCY RANGE 10 KHz - 32 MHz. FOR THE 1 ATM O_2 DATA, THE RESULTS FROM A FULL 7-PARAMETER FIT TO EQUATION 1 (DASHED RED LINE) AND A 6-PARAMETER FIT HOLDING R_{ION} FIXED (SOLID BLACK LINE) ARE SHOWN; THEY FALL SO CLOSELY ON TOP OF EACH OTHER IN THESE PLOTS AS TO BE INDISTINGUISHABLE.	24
FIGURE 2.10. (A) IMPEDANCE SPECTRA MEASURED AT ~ 710 °C AND 0.01 ATM O_2 FROM $(\text{La}_{0.8}\text{Sr}_{0.2})_{0.95}\text{MnO}_{3+\Delta}$ MICROELECTRODES OF VARIOUS THICKNESSES IN LIBRARY #1. (B) ZOOMED VIEW OF A SUBSET OF THE SAME SPECTRA.	25
FIGURE 2.11. DIAMETER DEPENDENCE OF THE SIX FIT PARAMETERS MEASURED FROM A THICKNESS LIBRARY OF $(\text{La}_{0.8}\text{Sr}_{0.2})_{0.95}\text{MnO}_{3+\Delta}$ FILMS (LIBRARY #1) AT ~ 710 °C UNDER VARIOUS OXYGEN PARTIAL PRESSURES WITH 246 NM MICROELECTRODE THICKNESS. THE LINES ARE LINEAR FITS, THE SLOPES OF WHICH ARE INDICATED NEXT TO THE LEGEND. 95% CONFIDENCE INTERVALS FROM THE FITS ARE SHOWN, EXCEPT WHERE THEY ARE SMALLER THAN THE DATA POINTS.	27
FIGURE 2.12. THICKNESS DEPENDENCE OF THE SIX FIT PARAMETERS MEASURED FROM A THICKNESS LIBRARY OF $(\text{La}_{0.8}\text{Sr}_{0.2})_{0.95}\text{MnO}_{3+\Delta}$ FILMS, LIBRARY #1, AT ~ 710 °C AND THE INDICATED OXYGEN PARTIAL PRESSURES. WHEN FITTING THE SPECTRA ACQUIRED UNDER 0.2 ATM O_2 AND 1 ATM O_2 , R_{ION} WAS HELD FIXED AT THE VALUE DETERMINED BY AVERAGING THE R_{ION} VALUES OBTAINED FROM THE FITS TO IMPEDANCE SPECTRA ACQUIRED FROM THE SAME MICROELECTRODE AT 0.01 ATM O_2 , 0.03 ATM O_2 , AND 0.1 ATM O_2 . 95% CONFIDENCE INTERVALS FOR THE FITS ARE SHOWN, EXCEPT WHERE THEY ARE SMALLER THAN THE DATA POINTS.	30
FIGURE 2.13. AMBIPOLAR DIFFUSIVITY D_{CHEM} (LEFT) AND VOLUME-NORMALIZED CHEMICAL CAPACITANCE C_{CHEM} (RIGHT) OF $(\text{La}_{0.8}\text{Sr}_{0.2})_{0.95}\text{MnO}_{3+\Delta}$ AT ~ 710 °C. THE ORANGE BOX BOUNDS THE RANGE OF VALUES FOR D_{CHEM} PREVIOUSLY MEASURED FROM BULK SAMPLES OF $\text{La}_{0.8}\text{Sr}_{0.2}\text{MnO}_{3+\Delta}$. ²⁹ COMPARABLE LITERATURE DATA IS ALSO SHOWN FOR C_{CHEM} . ^{10,30}	31

FIGURE 2.14. IMPEDANCE SPECTRA ACQUIRED FROM THE TEMPERATURE-GRADIENT $(\text{La}_{0.8}\text{Sr}_{0.2})_{0.95}\text{MnO}_{3+\Delta}$ LIBRARY UNDER 0.2 ATM O_2 , $\sim 710^\circ\text{C}$, 200 MM DIAMETER ELECTRODES, OVER THE FREQUENCY RANGE 10 KHZ - 32 MHZ. POINTS ARE RAW DATA, CURVES ARE FITS TO EQUATION 1.	33
FIGURE 2.15. FIT PARAMETERS MEASURED FROM THE GROWTH TEMPERATURE LIBRARY OF $(\text{La}_{0.8}\text{Sr}_{0.2})_{0.95}\text{MnO}_{3+\Delta}$ FILMS, LIBRARY #3, AT $\sim 710^\circ\text{C}$ AND THE INDICATED PO_2 . THE MICROELECTRODE DIMENSIONS WERE 200 MM DIAMETER AND 135 NM THICKNESS THROUGHOUT. LINES CONNECT THE POINTS AS GUIDES FOR THE EYE. 95% CONFIDENCE INTERVALS ARE SHOWN, EXCEPT WHERE THEY ARE SMALLER THAN THE DATA POINTS.....	34
FIGURE 2.16. ELECTROCHEMICAL ACTIVITY MEASURED AT $\sim 710^\circ\text{C}$ UNDER 0.01 ATM O_2 FROM LIBRARIES OF $(\text{La}_{0.8}\text{Sr}_{0.2})_{0.95}\text{MnO}_{3+\Delta}$ MICROELECTRODES WITH 200 MM DIAMETER AND VARIOUS GROWTH TEMPERATURE (BLUE SQUARES, 10 MTORR O_2 GROWTH) OR VARIOUS THICKNESSES (ORANGE, TRIANGLES AND CIRCLES ARE SAMPLES GROWN IN 30 MTORR O_2 AND 10 MTORR O_2 , RESPECTIVELY).	36
FIGURE S17. PRIMARY CHAMBER OF THE SCANNING IMPEDANCE PROBE. LEFT: EXTERNAL PHOTO. RIGHT: COMPUTER MODEL CROSS-SECTION SHOWING THE CHAMBER INTERIOR.	40
FIGURE S18. OPTICAL PHOTO OF THE STAGE USED TO ASYMMETRICALLY HEAT SUBSTRATES DURING PREPARATION OF THE LIBRARY OF GROWTH TEMPERATURES.....	40
FIGURE S19. SEEBECK VOLTAGE MEASURED BETWEEN THE COUNTER ELECTRODE AND AN OXIDE MICROELECTRODE CONTACTED BY A PALINEY7 PROBE TIP. RESCALING THE VOLTAGE BY THE SEEBECK COEFFICIENT OF YSZ YIELDS AN ESTIMATE FOR THE ASSOCIATED TEMPERATURE DROP BETWEEN THE ELECTRODES, ALSO SHOWN. CURVES ARE POWER-LAW FITS TO THE DATA AT EACH TEMPERATURE.....	42
FIGURE S20. XRD PATTERNS ACQUIRED FROM A THICKNESS LIBRARY OF $(\text{La}_{0.8}\text{Sr}_{0.2})_{0.95}\text{MnO}_{3+\Delta}$ MICROELECTRODES, LIBRARY #2, GROWN AT 650°C UNDER 10 MTORR O_2 . THE CORRESPONDING FILM THICKNESS IS LISTED TO THE RIGHT OF EACH PATTERN. THE ORIENTATION OF EACH LSM REFLECTION IS ALSO INDICATED. REFLECTIONS MARKED WITH AN ASTERISK ARE FROM THE YSZ SUBSTRATE.	44
FIGURE S21. LEFT: TYPICAL ROCKING CURVE ACQUIRED FROM THE $(\text{La}_{0.8}\text{Sr}_{0.2})_{0.95}\text{MnO}_{3+\Delta}$ GROWTH TEMPERATURE LIBRARY IN A REGION WHERE $T_{\text{GROWTH}} = 725^\circ\text{C}$. THE TWO FIT COMPONENTS ARE SHOWN IN RED AT BOTTOM; THE FIT RESIDUAL IS SHOWN IN GREEN AT TOP. RIGHT: FULL WIDTH AT HALF MAXIMUM (FWHM) VALUES EXTRACTED FROM THE ROCKING CURVES.....	45

FIGURE S22. AFM IMAGES ACQUIRED AFTER PATTERNING FROM A FOLLOW-UP THICKNESS LIBRARY OF $(\text{La}_{0.8}\text{Sr}_{0.2})_{0.95}\text{MnO}_{3+\Delta}$ MICROELECTRODES GROWN AT 650 °C UNDER 10 MTORR O_2 . THE CORRESPONDING FILM THICKNESS AND ROOT-MEAN-SQUARED ROUGHNESS ARE LISTED UNDER EACH MICROGRAPH.	45
FIGURE S23. SEM IMAGES FROM THE $(\text{La}_{0.8}\text{Sr}_{0.2})_{0.95}\text{MnO}_{3+\Delta}$ GROWTH TEMPERATURE LIBRARY AFTER EXPOSURE FOR 2 DAYS AT ~ 710 °C IN THE SCANNING IMPEDANCE PROBE. SOME OF THE OBSERVED CONTRAST IS DUE TO MILD SAMPLE CHARGING.....	46
FIGURE S24. EXPONENT OF THE CONSTANT PHASE ELEMENT USED TO REPRESENT THE SURFACE CAPACITANCE (C_{ION}^s) WHEN FITTING IMPEDANCE SPECTRA ACQUIRED FROM THE THICKNESS LIBRARY AT ~ 710 °C, 200 MM DIAMETER TO THE MODEL SHOWN IN EQUATION 1. 95% CONFIDENCE INTERVALS ARE SHOWN.....	47
FIGURE S25. THICKNESS DEPENDENCE OF THE FIT PARAMETER R_{ION} MEASURED FROM THE $(\text{La}_{0.8}\text{Sr}_{0.2})_{0.95}\text{MnO}_{3+\Delta}$ THICKNESS LIBRARY AT ~ 710 °C AT VARIOUS OXYGEN PARTIAL PRESSURES. THIS PLOT IS IDENTICAL TO THE PLOT OF R_{ION} IN FIGURE 2.12, EXCEPT HERE ALL SEVEN PARAMETERS WERE FREE TO VARY IN ALL FITS, INCLUDING THE 0.2 ATM AND 1 ATM FITS. 95% CONFIDENCE INTERVALS ARE SHOWN.....	47
FIGURE S26. THICKNESS DEPENDENCE OF THE AMBIPOLAR DIFFUSIVITY D_{CHEM} CALCULATED FROM THE $(\text{La}_{0.8}\text{Sr}_{0.2})_{0.95}\text{MnO}_{3+\Delta}$ THICKNESS TRENDS SHOWN IN FIGURE 2.12 FOR ~ 710 °C. 95% CONFIDENCE INTERVALS ARE SHOWN. (THEY ARE ARTIFICIALLY SMALL FOR THE 0.2 ATM AND 1 ATM ISOBARS, SINCE R_{ION} WAS HELD FIXED IN THOSE FITS.).....	48
FIGURE S27. TYPICAL IMAGES USED TO ESTIMATE THE SURFACE GRAIN BOUNDARY LENGTH. FILMS GROWN AT TWO DIFFERENT TEMPERATURES ARE SHOWN. LEFT: AFM MICROGRAPHS. RIGHT: SAME MICROGRAPHS AFTER IMAGE PROCESSING. THE SURFACE GRAIN BOUNDARY LENGTH WAS ESTIMATED BY SUMMING THE LENGTH OF THE BORDERS BETWEEN THE GREEN REGIONS.....	49
FIGURE S28. SURFACE ROUGHNESS AND OUT-OF-PLANE (110) PLANE SPACING MEASURED FROM THE AS-GROWN $(\text{La}_{0.8}\text{Sr}_{0.2})_{0.95}\text{MnO}_{3+\Delta}$ TEMPERATURE LIBRARY USING AFM, XRD, AND AFM, RESPECTIVELY.	49
FIGURE S29. SURFACE GRAIN BOUNDARY LENGTH ESTIMATED USING AFM IMAGES FROM THE GROWTH TEMPERATURE LIBRARY (BLUE) AND TWO THICKNESS LIBRARIES GROWN AT 10 MTORR O_2 (CIRCLES) AND 30 MTORR O_2 (TRIANGLES).....	50

FIGURE S30. EXAMPLE EDGE PROFILE OF AN LSM MICROELECTRODE PREPARED BY DRY ETCHING. THIS PARTICULAR PROFILE WAS ACQUIRED FROM AN 80 MM DIAMETER MICROELECTRODE IN LIBRARY #1..50	50
FIGURE S31. SURFACE RESISTANCE R_{ion}^s EXTRACTED FROM IMPEDANCE SPECTRA AT 710 °C IN 0.2 ATM O ₂ USING 200 MM DIAMETER MICROELECTRODES FROM TWO THICKNESS-GRADIENT LIBRARIES GROWN ON DIFFERENT SUBSTRATES AND MEASURED SEPARATELY. 95% CONFIDENCE INTERVALS ARE SHOWN. LINES ARE LINEAR FITS.	51
FIGURE 3.1. POSSIBLE ELECTROCHEMICAL PATHWAYS. (A) MIXED CONDUCTING PELLETT, (B) MIXED CONDUCTING MICROELECTRODE, (C) ELECTRONICALLY CONDUCTING MICROELECTRODE WITH SURFACE DIFFUSION ON ELECTROLYTE, AND (D) ELECTRONICALLY CONDUCTING MICROELECTRODE WITH ELECTRON MIGRATION THROUGH ELECTROLYTE.....	59
FIGURE 3.2. EQUIVALENT CIRCUITS FOR (A) MIXED CONDUCTING PELLETT, (B) LA _{0.5} SR _{0.5} CO ₃ MICROELECTRODE, (C) (LA _{0.8} SR _{0.2}) _{0.95} MNO ₃ MICROELECTRODE, AND (D) PT MICROELECTRODE ON SR _{0.06} NB _{0.06} BI _{1.87} O ₃	59
FIGURE 3.3. XRD PATTERNS ACQUIRED FROM A SINGLE YSZ SUBSTRATE CONTAINING LA _{0.5} SR _{0.5} CO ₃ FILMS WITH THICKNESSES IN THE RANGE 30 NM - 300 NM. COURTESY OF SHINGO MARUYAMA.....	60
FIGURE 3.4 LA _{0.5} SR _{0.5} CO ₃ FILMS AS GROWN BY PLD WITH THICKNESSES OF 30 NM (UPPER LEFT), 84 NM (UPPER RIGHT), LOWER LEFT (192 NM), AND LOWER RIGHT (300 NM). COURTESY OF SHINGO MARUYAMA.	61
FIGURE 3.5. OPTICAL PHOTOS OF TYPICAL LSC SAMPLES. FROM LEFT TO RIGHT: VARIOUS THICKNESSES RANGING FROM 300 NM - 30 NM; A SAMPLE CONTAINING EXACTLY TWO FILM THICKNESSES, 300 NM AND 30 NM; AND UNIFORM 200 NM THICKNESS. SOME DARK SMUDGES ARE VISIBLE; THIS IS RESIDUAL SILVER PASTE ON THE BACKSIDE OF THE TRANSPARENT SUBSTRATE (USED TO AFFIX THE SUBSTRATE DURING DEPOSITION).....	61
FIGURE 3.6. AFM PROFILE SCAN OF AN LSC MICROELECTRODE WITH 300 NM NOMINAL THICKNESS, 30 UM NOMINAL DIAMETER. COURTESY OF SHINGO MARUYAMA.	62
FIGURE 3.7. EDGE QUALITY OF LSC FILMS AFTER PATTERNING BY ION MILLING. LEFT: SEM MICROGRAPH, TAKEN FROM A SAMPLE WITHOUT CARBON COATING. RIGHT: AFM PROFILE SCAN, COURTESY OF SHINGO MARUYAMA.	63

FIGURE 3.8. SURFACE AND CROSS-SECTION SEM MICROGRAPHS OF A REPRESENTATIVE $\text{La}_{0.5}\text{Sr}_{0.5}\text{CoO}_{3-x}$ FILM WITH 100 NM THICKNESS THAT DID NOT UNDERGO IMPEDANCE TESTING. SAMPLE IS TILTED 52° IN THE CENTER AND RIGHT IMAGES.....	64
FIGURE 3.9 SEM MICROGRAPHS ACQUIRED AFTER IMPEDANCE TESTING OF $\text{La}_{0.5}\text{Sr}_{0.5}\text{CoO}_{3-x}$ FILMS WITH THICKNESSES OF 30 NM (LEFT), 165 NM (MIDDLE), AND 300 NM (RIGHT).	64
FIGURE 3.10. TYPICAL IMPEDANCE SPECTRA ACQUIRED FROM THIN FILM $\text{La}_{0.5}\text{Sr}_{0.5}\text{CoO}_{3-x}$ MICROELECTRODES OVER THE FREQUENCY RANGE 10 KHZ - 20 MHZ. POINTS ARE THE RAW DATA; CURVES ARE FITS TO THE EQUIVALENT CIRCUIT SHOWN IN SECTION 3.4. THE DATA SHOWN HERE WERE ACQUIRED FROM MICROELECTRODES WITH 200 MM DIAMETER AT THE INDICATED TEMPERATURES AND OXYGEN PARTIAL PRESSURE.	65
FIGURE 3.11. OFFSET RESISTANCE R_0 EXTRACTED FROM IMPEDANCE SPECTRA MEASURED FROM $\text{La}_{0.5}\text{Sr}_{0.5}\text{CoO}_{3-x}$ FILMS OF VARIOUS THICKNESSES AT THE INDICATED TEMPERATURES AND OXYGEN PARTIAL PRESSURES.	66
FIGURE 3.12. SURFACE RESISTANCE R_s EXTRACTED FROM IMPEDANCE SPECTRA MEASURED FROM $\text{La}_{0.5}\text{Sr}_{0.5}\text{CoO}_{3-x}$ FILMS OF VARIOUS THICKNESSES AT THE INDICATED TEMPERATURES AND OXYGEN PARTIAL PRESSURES.	67
FIGURE 3.13. TOTAL CAPACITANCE C_{CHEM} EXTRACTED FROM IMPEDANCE SPECTRA MEASURED FROM $\text{La}_{0.5}\text{Sr}_{0.5}\text{CoO}_{3-x}$ FILMS OF VARIOUS THICKNESSES AT THE INDICATED TEMPERATURES AND OXYGEN PARTIAL PRESSURES.	67
FIGURE 3.14. SURFACE RESISTANCE MEASURED ON A SECOND SAMPLE OF LSC MICROELECTRODES WITH THICKNESSES OF 30 NM AND 300 NM, PROBED AT $\sim 520^\circ\text{C}$ IN 0.01 ATM O_2	68
FIGURE 3.15. AREA-NORMALIZED SURFACE RESISTANCE R_s (UPPER LEFT), TOTAL CAPACITANCE C_{TOTAL} (LOWER LEFT), AND OFFSET RESISTANCE R_0 (UPPER RIGHT) OF (200 MM DIAMETER) $\text{La}_{0.5}\text{Sr}_{0.5}\text{CoO}_{3-x}$ MICROELECTRODES OF VARIOUS THICKNESSES AT 615°C . LINES ARE LINEAR FITS TO THE RAW DATA POINTS. THE FIT RESIDUALS ARE PLOTTED AS A SUBPLOT BELOW THE MAIN PLOT.....	70
FIGURE 3.16. COMPARISON OF THE VOLUME-NORMALIZED CHEMICAL CAPACITANCE OF THIN FILMS (THIS WORK) AND BULK SAMPLES ⁵⁹ OF $\text{La}_{0.5}\text{Sr}_{0.5}\text{CoO}_{3-x}$. LINES CONNECTING THE DATA POINTS ARE GUIDES FOR THE EYE.	72
FIGURE 3.17. SURFACE RESISTANCE R_s OF $\text{La}_{0.5}\text{Sr}_{0.5}\text{CoO}_{3-x}$ FILMS AFTER DWELLING SEVERAL HOURS AT EACH GIVEN TEMPERATURE AND OXYGEN PARTIAL PRESSURE, PLOTTED VERSUS OXYGEN PARTIAL PRESSURE (LEFT) AND IN	

ARRHENIUS FORM (RIGHT). POINTS WERE CALCULATED BY AVERAGING THE VALUES MEASURED FROM SEVERAL FILM THICKNESSES. FOR COMPARISON, DATA AT 0.2 ATM FOR $\text{Ba}_{0.5}\text{Sr}_{0.5}\text{Co}_{0.8}\text{Fe}_{0.2}\text{O}_{3-\delta}$ FILMS (GROWN ON SDC (100) ON YSZ (100)) ARE SHOWN AT RIGHT IN LIGHT GRAY (FRANCISCO BARROSO, HAILE GROUP UNPUBLISHED)..... 72

FIGURE 3.18. OPTICAL (LEFT) AND SEM (RIGHT) IMAGES OF PLATINUM MICROELECTRODES ON AN SNB SUBSTRATE, BEFORE IMPEDANCE TESTING. 74

FIGURE 3.19. SEM IMAGES OF THE SNB SURFACE (LEFT) AND A PLATINUM MICROELECTRODE (RIGHT) AFTER SEVERAL DAYS OF IMPEDANCE TESTING AT $575^{\circ}\text{C} - 650^{\circ}\text{C}$ UNDER $\text{pO}_2 = 10^{-3} - 1$ ATM. 74

FIGURE 3.20. IMPEDANCE SPECTRA ACQUIRED FROM PLATINUM MICROELECTRODES OF VARIOUS DIAMETERS ON SNB AT $\sim 625^{\circ}\text{C}$ IN 0.2 ATM O_2 . POINTS ARE RAW DATA; LINES ARE FITS TO THE EMPIRICAL EQUIVALENT CIRCUIT DESCRIBED IN SECTION 3.4. 75

FIGURE 3.21. OVERALL ARC WIDTH $R_{\text{dc}}-R_0$ (TOP) AND OFFSET RESISTANCE R_0 (BOTTOM) MEASURED OVER TIME AT THE INDICATED TEMPERATURES AND OXYGEN PARTIAL PRESSURES FROM PLATINUM MICROELECTRODES OF VARIOUS DIAMETERS ON SNB. POINTS WERE EXTRACTED FROM THE IMPEDANCE SPECTRA; LINES CONNECT THE POINTS AS GUIDES FOR THE EYE. 76

FIGURE 3.22. OVERALL ARC WIDTH $R_{\text{dc}}-R_0$ MEASURED FROM PLATINUM MICRODOTS ON SNB AT $\sim 625^{\circ}\text{C}$ AS A FUNCTION OF DIAMETER (LEFT) AND OXYGEN PARTIAL PRESSURE (RIGHT). POINTS WERE EXTRACTED FROM THE IMPEDANCE SPECTRA; LINES ARE LINEAR FITS ON A DOUBLE-LOGARITHMIC SCALE. 77

FIGURE 3.23. ARRHENIUS PLOT OF THE ELECTROCHEMICAL REACTION RESISTANCE. THE FILM TEMPERATURES WERE CORRECTED APPROXIMATELY FOR TIP COOLING. POINTS ARE EXTRACTED FROM THE IMPEDANCE SPECTRA; LINES ARE LINEAR FITS TO THE POINTS. THE ACTIVATION ENTHALPY EXTRACTED FROM THE LINE SLOPES IS SHOWN BESIDE THE LEGEND. 79

FIGURE 4.1. SCHEMATIC OF THE TEST CONFIGURATION IN THE SCANNING IMPEDANCE PROBE. 83

FIGURE 4.2. EXAMPLE LAYOUTS OF MICROELECTRODES ON A SAMPLE. LEFT: $17 \times 21 = 357$ MICROELECTRODES (INCLUDING 11 DIFFERENT DIAMETERS) ON A 5 MM X 10 MM SUBSTRATE. RIGHT: $23 \times 23 = 529$ MICROELECTRODES ON A 10 MM X 10 MM SUBSTRATE. 85

FIGURE 4.3. EXAMPLES OF PROPERTIES THAT CAN BE SYSTEMATICALLY VARIED ALONG THE ROWS AND/OR COLUMNS OF A MICROELECTRODE ARRAY.....	86
FIGURE 4.4. SCHEMATIC OF A QUATERNARY LIBRARY THAT COULD BE MADE FROM FOUR BINARY TARGETS (BaFeO_x , SrFeO_x , BaCoO_x , AND SrCoO_x) TO SPAN THE FAMILY OF COMPOSITIONS $\text{Ba}_{1-x}\text{Sr}_x\text{Co}_{1-y}\text{Fe}_y\text{O}_{3-\delta}$, WHERE $x, y \in [0,1]$	88
FIGURE 4.5. SCANNING IMPEDANCE PROBE SYSTEM.	89
FIGURE 4.6. PRIMARY CHAMBER OF THE SCANNING IMPEDANCE PROBE. LEFT: EXTERNAL PHOTO. RIGHT: COMPUTER MODEL CROSS-SECTION, SHOWING THE CHAMBER INTERIOR.	89
FIGURE 4.7. TYPICAL SAMPLE CONFIGURATIONS INSIDE THE SCANNING IMPEDANCE PROBE. LEFT: AT ROOM TEMPERATURE WITH ADDED ILLUMINATION. RIGHT: A DIFFERENT SAMPLE AT $\sim 800^\circ\text{C}$ SAMPLE TEMPERATURE WITH NO ADDED ILLUMINATION.	90
FIGURE 4.8. CALIBRATION OF THE SAMPLE SURFACE TEMPERATURE. LEFT: MEASUREMENT CONFIGURATION. RIGHT: MEASURED "FILM" TEMPERATURE PLOTTED VS. THE STAGE (A.K.A. ELEMENT) TEMPERATURE.	92
FIGURE 4.9. MEASURED VOLTAGE DROP $V_{\text{FILM}} - V_{\text{COUNTER ELECTRODE}}$ ACROSS THE YSZ SUBSTRATE USING AN $\text{La}_{0.5}\text{Sr}_{0.5}\text{CoO}_{3-\delta}$ MICROELECTRODE AND A TIP MADE OF PALINEY7 (A NOBLE METAL ALLOY CONTAINING PRIMARILY PALLADIUM).....	95
FIGURE 4.10. LEFT: SPURIOUS INDUCTANCE AT HIGH FREQUENCIES, CAUSED BY IMPROPER CHOICE OF CURRENT RANGE. RIGHT: SPURIOUS JUMP IN THE DATA UPON CHANGING CURRENT RANGES FOR LOW CAPACITANCE SAMPLES.	98
FIGURE 5.1. X-RAY POWDER DIFFRACTION PATTERNS FOR SCN AFTER CALCINATION AT 1200°C (RED), AFTER A SUBSEQUENT ANNEAL AT 750°C IN AIR FOR 10 D (GREEN), AND AFTER A SUBSEQUENT ADDITIONAL ANNEAL AT 1200°C IN AIR FOR 10 H (BLUE).	105
FIGURE 5.2. OXYGEN STOICHIOMETRY $3-\delta$ OF BSCF AND SCN MEASURED BY THERMOGRAVIMETRY, PLOTTED FOR COMPARISON WITH DATA FROM OTHER REPORTS ON $\text{La}_{0.1}\text{Sr}_{0.9}\text{Co}_{0.8}\text{Fe}_{0.2}\text{O}_{3-\delta}$ (LSCF 1982) ⁷⁰ , $\text{SrCo}_{0.8}\text{Fe}_{0.2}\text{O}_{3-\delta}$ (SCF 082) ⁷¹ , SCN ⁷² , AND BSCF ^{63,67,69}	106
FIGURE 5.3. IMPEDANCE SPECTRUM OF $\text{Ba}_{0.5}\text{Sr}_{0.5}\text{Co}_{0.8}\text{Fe}_{0.2}\text{O}_{3-\delta}$ AT 600°C IN 2×10^{-5} ATM O_2	108

FIGURE 5.4. ELECTRONIC CONDUCTIVITY Σ . (A) BSCF ISOTHERMS, (B) BSCF ISOBARS, (C) SCN ISOTHERMS, AND (D) SCN ISOBARS, PLOTTED WITH COMPARABLE LITERATURE DATA. ^{72,73}	109
FIGURE 5.5. ELECTRONIC CONDUCTIVITY Σ OF BSCF AND SCN PLOTTED AS ISO-STOICHIOMETRIC CURVES. LINES CONNECT THE DATA POINTS AS GUIDES FOR THE EYE.	111
FIGURE 5.6. LATTICE PARAMETER A_0 OF EQUILIBRATED SCN MEASURED BY <i>IN SITU</i> X-RAY DIFFRACTION. CURVES SHOWN ARE LINEAR FITS TO THE DATA. ALSO PLOTTED ARE COMPARABLE LITERATURE DATA FOR EQUILIBRATED BSCF TAKEN BY NEUTRON DIFFRACTION. ⁶⁸	112
FIGURE 5.7. LATTICE PARAMETER A_0 OF EQUILIBRATED SCN, PLOTTED AS A FUNCTION OF OXYGEN NON-STOICHIOMETRY Δ . CURVES SHOWN ARE LINEAR FITS TO THE DATA. ERROR BARS FOR Δ ARE ESTIMATED AS ± 0.10 (ABSOLUTE) AND ± 0.02 (RELATIVE).	113
FIGURE 5.8. LINEAR EXPANSIVITY A_L OF SCN PLOTTED WITH COMPARABLE LITERATURE DATA FOR BSCF. ⁶⁸	114
FIGURE 5.9. LINEAR CHEMICAL EXPANSIVITY A_C OF SCN PLOTTED WITH COMPARABLE LITERATURE DATA FOR BSCF. ⁶⁸	115
FIGURE 6.1. SCHEMATIC OF THE BEAMPATH IN THE NRIXS EXPERIMENT.	122
FIGURE 6.2. THE LERIX SPECTROMETER USED IN THE NRIXS MEASUREMENTS AND LOCATED AT BEAMLINE 20-ID AT THE ADVANCED PHOTON SOURCE. TOP: OVERALL CONFIGURATION. LEFT: MOUNTING OF THE HIGH-TEMPERATURE CHAMBER DURING THE NRIXS MEASUREMENT. RIGHT: SCN POWDER COMPACT USED IN THE MEASUREMENT, BEFORE INSTALLATION INTO THE HIGH-TEMPERATURE CHAMBER.	123
FIGURE 6.3. TYPICAL MASS PROFILE OF AN SCN PELLET EQUILIBRATED IN THE TGA AT HIGH TEMPERATURE AND THEN QUENCHED. SEE PELLET #5 IN TABLE 6.1 FOR PROCESSING PARAMETERS.	125
FIGURE 6.4. XRD PATTERNS TAKEN FROM THE SIX PELLETS SHORTLY AFTER QUENCHING. A VERTICAL BLACK LINE WAS ADDED AT 67° TO MAKE THE PEAK SHIFTS BETWEEN SPECTRA EASIER TO SEE.	127
FIGURE 6.5. X-RAY PHOTOELECTRON SPECTRA MEASURED FROM SCN QUENCHED PELLETS WITH VARIOUS OXYGEN STOICHIOMETRIES 3- Δ , SHOWING THE NIOBIUM $3D_{3/2-5/2}$ PEAKS (LEFT) AND COBALT $2P_{1/2-3/2}$ PEAKS (RIGHT).	128

FIGURE 6.6. STRONTIUM (UPPER LEFT), NIOBIUM (UPPER RIGHT), AND COBALT (LOWER LEFT AND RIGHT) K EDGES FOR SCN PELLETS QUENCHED WITH VARIOUS OXYGEN STOICHIOMETRIES. INSET PLOTS SHOW AN ENLARGED VIEW OF THE EDGES AT THRESHOLD.....	130
FIGURE 6.7. QUASI-CUBIC LATTICE PARAMETER A_0 AND COBALT K EDGE THRESHOLD ENERGY AS A FUNCTION OF OXYGEN STOICHIOMETRY.....	131
FIGURE 6.8. OXYGEN K EDGES TAKEN BY NON-RESONANT INELASTIC X-RAY SCATTERING (NRIXS) ON SCN. DATA INDICATED BY CIRCLES ARE A REPEAT RUN.	133
FIGURE 6.9. COBALT K EDGES FOR SCN TAKEN USING XAFS. GREEN = QUENCHED PELLET AT 25°C WITH 3-Δ OF 2.55, RED = QUENCHED POWDER AT 25°C WITH 3-Δ OF 2.57, PURPLE/BLUE = POWDER COMPACT EQUILIBRATED AT 1000°C WITH 3-Δ OF 2.45.....	135
FIGURE 6.10. OXYGEN K EDGES ACQUIRED FROM $La_{0.6}Sr_{0.4}FeO_{3-\Delta}$ BY NON-RESONANT INELASTIC X-RAY SCATTERING (NRIXS). OXYGEN STOICHIOMETRIES LISTED IN THE LEGEND WERE CALCULATED FROM LITERATURE DATA ⁸⁶ AND IN-HOUSE THERMOGRAVIMETRY.....	138
FIGURE 6.11. ⁵⁷ Fe MÖSSBAUER SPECTRUM FROM $La_{0.6}Sr_{0.4}FeO_{2.98}$ POWDER AT 25°C.	138

List of Tables

TABLE 6.1. SUMMARY OF PARAMETERS FROM THE PELLETT QUENCHING RUNS. 126

CHAPTER 1 OVERVIEW

1.1 Summary

This thesis is divided into two halves. The first half describes a high throughput approach for characterizing the electrochemical activity of *thin film* samples of solid oxide fuel cell (SOFC) catalysts. The second half contains investigations of *bulk* samples that yield insight into the defect chemistry and electronic behavior of a model catalyst, $\text{SrCo}_{0.9}\text{Nb}_{0.1}\text{O}_{3-\delta}$ (SCN). The two halves are linked by a common motivation to understand the electrochemical properties of the most important SOFC cathode materials. This motivation is explained below in more detail.

1.2 Why study solid oxide fuel cell (SOFC) materials?

Solid oxide fuel cells (SOFCs) are the most efficient devices yet invented for converting fuel into electricity. Industrial systems that cogenerate electricity and heat using SOFCs have projected efficiencies of up to $\sim 75\%$, exceeding what is possible in combustion systems.¹ SOFC systems are also fuel flexible; they can generate electricity from natural gas, hydrogen, ethanol, propane, biofuels, and more. Furthermore, when operated in reverse, SOFCs are the most efficient electrolyzers known, i.e., when supplied with electricity, an SOFC can efficiently split water to generate hydrogen fuel. Despite the enormous promise of this technology, commercial SOFC development has been hampered by inadequate catalyst performance, coupled with a lack of understanding of how the catalyst can

be improved. These technological capabilities and challenges are described in detail elsewhere.^{1,2}

The study of SOFC electrodes is also intricately linked to a number of fundamental scientific questions in catalysis: What intrinsic material parameters determine the rate of electrochemical charge transfer at an interface? What are the reaction pathways? What chemical changes cause catalysts to improve or degrade with time? These questions have been discussed in recent reviews pertaining to SOFC cathode³⁻⁵ and SOFC anode^{5,6} materials. Among other conclusions, these reviews make clear the importance of electrochemical impedance measurements on dense patterned thin film electrodes for elucidating the redox activity and catalytic pathways at the surfaces of these materials.

1.3 Why study thin films of SOCF catalysts?

The motivation for measuring dense patterned thin films is that in porous catalyst microstructures, a consequence of porosity is that the intrinsic surface activity of the catalyst is convoluted with extrinsic factors like surface area, microstructure interconnectedness, tortuosity, length of the so-called "triple phase boundary" (the boundary between the catalyst, the electrolyte, and the gas phase, where the rate-limiting step is often thought to occur), and so on. It can be quite difficult to characterize and deconvolute these geometry-dependent factors. The task has been helped by recent advances in 3D characterization techniques like x-ray tomography and focused ion beam milling in combination with scanning electron

microscopy. However, these methods remain fairly slow and expensive and often include significant uncertainty. On the other hand, by using dense samples with well-characterized geometries, it becomes easier to normalize by geometry (e.g., scaling catalytic activity by surface area) to obtain intrinsic material properties.

A second common difficulty is that in typical electrochemical methods for measuring activity (which involve current and voltage measurements and which go by various names, including a.c. impedance spectroscopy and d.c. voltammetry), it is challenging to decoupling the rates of the anode and cathode reactions, since they occur simultaneously and both contribute to the overall measurement. In electrochemical systems with a *liquid* electrolyte, this common problem is usually resolved by using a reference electrode, i.e., a third electrode that is placed in the liquid electrolyte to help decouple the potential changes at the two electrodes.

Numerous workers have also tried to use a reference electrode to decouple the anode and cathode overpotentials in systems with a *solid* electrolyte. However, papers by Adler and others have shown quantitatively that "minor errors in the alignment of the anode and cathode can create significant errors in the measured half-cell overpotential... [including] cross-contamination of anode and cathode frequency response... [and] even if electrodes are perfectly aligned, differences [in kinetics]... may cause inherent distortion of the impedance, including frequency dispersion and inductive artifacts."⁷ For this reason, reference electrodes have largely fallen out of favor in studies of the activity of SOFC catalysts.

As an alternative, microelectrodes have emerged over the last fifteen years as a reference-less way to decouple the anode and cathode behavior. In this approach, the two electrodes are fabricated with vastly different surface areas: a small area working electrode ($\sim 10^{-4}$ cm²) is dwarfed by a large area counter electrode (~ 1 cm²). In such a configuration, the measured electrochemical response can often be attributed entirely to the small area electrode, a.k.a. the microelectrode, with negligible error. The conditions under which this attribution is sufficiently accurate have been estimated previously.⁸

These sample requirements --- dense, geometrically well-defined, and having tiny area --- motivate the use of patterned thin film microelectrodes. First reported in 2000,⁹ such films are typically grown by physical vapor deposition (usually pulsed laser deposition or sputtering) and then patterned into the desired shapes by photolithography and subsequent dry etching (milling with argon ions) or wet etching (dissolution in acid). The area/perimeter of the microelectrodes can be systematically varied within a single pattern, which helps to identify scaling relations and interpret the electrochemical results. Roughly 25 papers using this approach have been published since 2000.

Despite its success, a number of issues have constrained the microelectrode approach. First, sample preparation is slowed by the need to synthesize a different target for each composition prior to physical vapor deposition. Studying tens or

hundreds of compositions can thus be quite cumbersome. (This constraint is not unique to the microelectrode approach.) Varying other parameters besides composition --- film thickness, surface decoration, growth conditions, substrate orientation, and so on --- has also required growing numerous films one at a time, in series. Acquiring impedance spectra from these samples also had to be done in series, further adding to the experiment time. This time constraint likely explains why studies typically report results for only two or three film thicknesses, even in cases where film thickness appears to be a critical parameter.^{10,11} Another issue is that subtle differences between samples prepared or characterized in series can introduce experimental errors that mask trends of interest. Surface activity may be sensitive to small changes in impurity content, for example. Also, prior to this work, the acquisition of each of hundreds or potentially thousands of impedance spectra required the cumbersome operator task of manually contacting each microelectrode with a tiny metal probe tip every few minutes. Perhaps in part because of the repetitive nature of this task, the stability and repeatability of impedance measurements from microelectrodes are not always clearly reported in the literature. Indeed, sometimes the stability is not mentioned at all,^{10,11} leaving the reader to assume(perhaps incorrectly) that the material properties are entirely stable over time.

1.4 Why study bulk defect chemistry?

The surface activity is arguably the single most important property of a catalyst, but there are many reasons why understanding the bulk defect chemistry may also be extremely useful:

First, bulk thermodynamic instability of a material can explain why its surface properties change with time. Second, correlations between surface and bulk transport rates (specifically, the oxygen tracer surface exchange coefficient k^* and the oxygen tracer bulk diffusion coefficient D^*) have been observed over a wide range of oxygen-conducting materials,^{12,13} suggesting that the surface and bulk properties are closely linked. Third, in $\text{SrTi}_{1-x}\text{Fe}_x\text{O}_{3-\delta}$ a strong correlation has been observed between the surface activity and the Fermi level in bulk samples, again suggesting that the surface catalysis and the bulk electronic structure can be closely linked.¹⁴ Fourth, a knowledge of bulk properties helps with experimental design. For example, the results of thin film studies of surface activity can be distorted if electronic sheet resistance contributes significantly to the measured impedance, and knowing the electronic conductivity helps in predicting and avoiding this distortion.¹⁵ Fifth, a knowledge of bulk properties also helps with device fabrication. For example, a nearly ubiquitous concern in developing practical solid oxide fuel cell devices is that if the thermochemical expansivities of the cathode and electrolyte are not well-matched, mechanical stresses can crack the electrolyte and ruin the device.

1.5 Why focus on the bulk defect chemistry of $\text{SrCo}_{0.9}\text{Nb}_{0.1}\text{O}_{3-\delta}$?

As described further in Section 3.2, a large number of state-of-the-art SOFC cathode catalysts are materials with the perovskite structure that contain the elements Sr and Co. This category of materials includes such compositions as $\text{Ba}_{0.5}\text{Sr}_{0.5}\text{Co}_{0.8}\text{Fe}_{0.2}\text{O}_{3-\delta}$ (BSCF), $\text{La}_{1-x}\text{Sr}_x\text{Co}_{1-y}\text{Fe}_y\text{O}_{3-\delta}$ (LSCF), $\text{La}_{1-x}\text{SrCoO}_{3-\delta}$ (LSC), $\text{Sm}_x\text{Sr}_{1-x}\text{CoO}_3$ (SSC), and others. The composition $\text{SrCo}_{0.9}\text{Nb}_{0.1}\text{O}_{3-\delta}$ (SCN)¹⁶ also exhibits extraordinary performance as a fuel cell cathode,¹⁷ yet its defect chemistry is likely simpler than many of the above compositions, since it contains only three cations, and the niobium cation is in relatively low concentration and is fixed-valent (as shown in Chapter 6).¹⁸ For these reasons SCN is a reasonable choice as a "model material" for fundamental studies of perovskites containing Sr and Co; thus SCN is the focus of the bulk defect chemistry investigations in Chapter 5 and Chapter 6.

CHAPTER 2 HIGH THROUGHPUT CHARACTERIZATION OF $(\text{La}_{0.8}\text{Sr}_{0.2})_{0.95}\text{MnO}_{3+\delta}$ THIN FILM MICROELECTRODES

This chapter introduces the scanning impedance probe, a robotic instrument that can rapidly measure the electrochemical impedance response of hundreds of thin film electrodes in automated fashion. This instrument is combined with a parallel fabrication method that produces libraries containing hundreds of thin film electrodes with systematically varied properties on a single substrate. Results are presented from libraries of $(\text{La}_{0.8}\text{Sr}_{0.2})_{0.95}\text{MnO}_{3+\delta}$ (LSM) microelectrodes with systematically varied area, thickness, and growth temperature. The measured impedance spectra are well fit by a physically derived electrochemical model, and all trends are consistent with a pathway involving oxygen reduction over the entire surface of the LSM microelectrode followed by diffusion through the film and into the YSZ electrolyte. The surface activity is found to be correlated with the number of exposed grain boundary sites, suggesting that grain boundaries are more active than grains towards the rate-limiting surface process.

2.1 Introduction

As described in Chapter 1, in recent years many studies have probed patterned thin film electrodes using electrochemical impedance spectroscopy to yield rich insights into the behavior of mixed ionic and electronic conductors (MIECs),

including accurate measurements of the intrinsic surface activity of such materials towards oxygen electro-reduction.⁵ This chapter builds on the success of the patterned thin film electrode approach by adding two innovations that increase throughput and reliability. First, a scanning impedance probe is described that can perform data acquisition and processing with higher throughput. Second, libraries of thin film microelectrodes with systematically varied film thickness or growth temperature are fabricated and characterized on a single solid electrolyte substrate. This parallel fabrication method helps to further improve throughput, and it helps avoid unintended differences that can arise when samples are prepared or measured in series. Such differences can mask trends with the parameters of interest.

In the specific case of $(\text{La}_{1-x}\text{Sr}_x)_{1-y}\text{MnO}_{3+\delta}$, a heavily studied cathode material that is commonly used in commercial applications,^{2,3} both patterned and unpatterned thin film studies have reached agreement that the three phase boundary pathway, wherein oxygen incorporation into the electrolyte occurs at the boundary of the LSM, electrolyte, and gas phases, is not always dominant, but can be outcompeted by a through-the-film pathway, wherein oxygen ions incorporate at the LSM surface, diffuse through the LSM film, and then cross into the electrolyte.^{9,10,19,20} Moreover, the shapes of the impedance spectra reported in these studies are broadly similar; the typical spectrum includes a high frequency feature that exhibits relatively little change with film thickness, and a low frequency semicircle

with a characteristic resistance that scales approximately linearly with increasing film thickness.

However, there is substantial disagreement in the interpretation of these spectra and in the conclusions drawn about the rates of the surface and bulk steps. In light of the thickness trends just described, several studies suggested that the high-frequency feature corresponds to the surface incorporation process, and that the low frequency semicircle corresponds to bulk diffusion through the film.²⁰⁻²² However, these reports do not mention the possibility that surface properties (like the number of exposed grain boundaries) may depend on thickness.

On the other hand, using fits by an equivalent circuit based on a physically derived model for MIECs, Fleig et al. assigned the high frequency feature to bulk diffusion and the low frequency semicircle to surface incorporation.¹⁰ These authors noted that the resulting surface exchange rate increased somewhat with increasing thickness, and they commented that there may be a "thickness-dependent film structure and chemistry".

The present study seeks to resolve this disagreement, which is important because of its direct implications for how to improve surface activity in an LSM-based cathode. In particular, if the largest contribution to the electrode resistance comes from surface incorporation, then modifying the LSM surface (e.g., by decoration with catalyst particles) could be a fruitful strategy. In contrast, if the largest

resistance contribution comes from diffusion through the film, then alternate strategies would be more beneficial.

2.2 Overview of the scanning impedance probe

The configuration of the scanning impedance probe is shown schematically in Figure 2.1 and to scale in Figure S17.

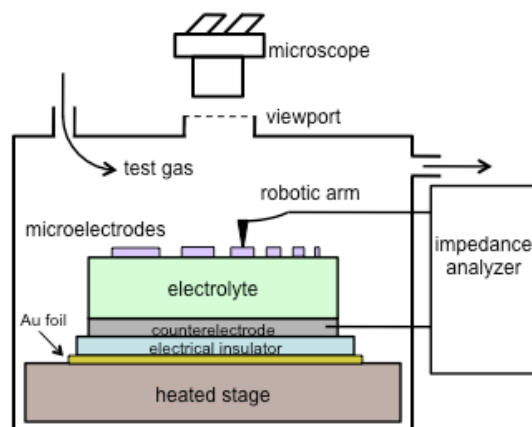


Figure 2.1. Schematic of the test configuration in the scanning impedance probe. Dimensions are not to scale.

Compared to previously reported instruments for probing microelectrodes,^{9,23} the most significant new feature here is the scanning capability: the position of the alumina arm holding the metal probe tip is determined by three orthogonal lead screws connected to stepper motors (Figure S17). Thus the metal probe tip can be touched to a microelectrode simply by entering the coordinates of that microelectrode in the control software. The temperature and gas environment are also controlled in software. Moreover, the dimensional tolerances associated with

the patterning process are small enough that the relative spacing of the microelectrodes on the substrate surface can be accurately predicted, and three points are sufficient to define the plane of that surface. Consequently, once the user manually finds the coordinates of three reference microelectrodes in a library, the coordinates of all the other microelectrodes can be readily computed. Hundreds of microelectrodes can then be probed in any desired sequence over a range of environmental conditions in automated fashion.

2.3 Experimental procedures

A sintered pellet of $(\text{La}_{0.8}\text{Sr}_{0.2})_{0.95}\text{MnO}_3$ (LSM) was prepared for use as a pulsed laser deposition target as follows. First, a dense compact was prepared from 20 g commercial powder (Fuel Cell Materials, 99.5% pure) with 1 wt% polyvinylpyrrolidone added to serve as a binder. The powder was subjected to uniaxial pressure under 20 MPa for 10 min in a 32 mm diameter die, followed by isostatic pressure under 350 MPa for 20 min. The edges and faces of this powder compact were shaved using a razor to remove any surface contamination from the die, then this powder compact was placed on an alumina support with excess powder spread below the compact to avoid reactivity with the alumina. The compact was then sintered at 1450 °C for 5 h in stagnant air in a dedicated alumina tube. The resulting pellet was polished on all sides with sandpaper down to 600 grit, sonicated in water and isopropanol to remove the residual grit, and finally measured as having 26 mm diameter and 6 mm thickness. X-ray diffraction (XRD, Philips X'Pert Pro, Cu Ka) patterns acquired from both faces of the pellet showed good agreement with patterns reported in the Inorganic Crystal Structure Database for a virtually identical composition ($\text{La}_{0.8}\text{Sr}_{0.2}\text{MnO}_3$).

Using this target, $(\text{La}_{0.8}\text{Sr}_{0.2})_{0.95}\text{MnO}_3$ films were grown on (100)-oriented single crystal $\text{Y}_{0.15}\text{Zr}_{1.85}\text{O}_{1.93}$ substrates (YSZ, 8 mol% Y_2O_3 -stabilized ZrO_2 , 5 mm x 10 mm x 0.5 mm, MTI Corporation) by pulsed laser deposition with a KrF excimer laser (248 nm, 0.8 J/cm², 1 Hz). During film growth, each substrate was adhered to a heated stage with silver paste, which was subsequently scraped off.

On two substrates, the *thickness* of the LSM film was systematically varied by using a motor to slowly draw an Inconel shutter across the deposition plume during growth. This procedure created two "thickness libraries" in which the film thickness varied continuously from 30 nm to 300 nm across the substrate. The

deposition parameters for Library #1 were as follows: 650 °C growth temperature, 10 mtorr O₂ working pressure, 1 Hz ablation laser pulse frequency, 0.7 nm/min deposition rate, and 100 °C/min cooling rate. For Library #2, all conditions were identical with the exception of the working pressure, which was held at 30 mtorr O₂.

On a third substrate, the *growth temperature* of the LSM film was systematically varied using an asymmetric stage geometry (shown in Figure S18) heated at one end with infrared radiation. This procedure created a "growth temperature library", Library #3, in which the growth temperature varied continuously from 555 °C to 725 °C across the substrate. The substrate temperature was measured in numerous places during growth using an optical pyrometer. Other deposition parameters for Library #3 were as follows: uniform 135 nm thickness, 30 mtorr O₂ pressure, 5 Hz ablation laser pulse frequency, 2.7 nm/min deposition rate (calibrated in advance by acquiring atomic force microscopy (AFM, Digital Instruments Nanoscope III) profiles from test films prepared with the same target and deposition parameters), and 20 °C/min cooling rate.

After growth, XRD patterns, rocking curves, and AFM micrographs were acquired from each film in several regions (Bruker D8 Discover, Cu K α). Each film was then patterned into a library of microelectrodes using photolithography and ion milling. Specifically, two coats of photoresist (Shipley 1813) were applied by spin coating on top of each film, exposure to UV radiation through a photomask, and then development. The film then underwent ion milling for 45 min resulting in a milling depth of ~350 nm. The residual photoresist was then chemically stripped. In this way, each film was converted into a library of 337 circular microelectrodes. Each library included nine different values of microelectrode diameter spanning the range 50 μ m - 500 μ m. The "growth temperature library" included twenty-one different values of growth temperature, unevenly spaced from 555 °C - 725 °C, while the thickness libraries included twenty-one different values of film thickness, evenly spaced from 30 nm - 300 nm. Because the thickness or growth temperature varied continuously across each library it also varied slightly across each microelectrode. However, the microelectrodes had small enough diameter that a single value of thickness or growth temperature (the local average value) could be assigned to each microelectrode with minimal loss of accuracy. Specifically, for Libraries #1 and #2 the difference in thickness across the largest microelectrode probed (500 μ m) is 15 nm, while for Library #3 the difference in growth temperature across the largest microelectrode probed (200 μ m) was ~ 5 °C.

After patterning the libraries were characterized by optical microscopy and again by AFM. In preparation for impedance measurements, each substrate was then adhered to a ~ 10 mm x 20 mm x 0.6 mm alumina sheet using silver paste (DAD-87, Shanghai Research Institute). Heat treatment in a quartz tube under stagnant

air at 600 °C - 700 °C for 1 h induced sintering of the paste into a porous counter electrode.

Thus prepared, Library #1 was installed in the scanning impedance probe and heated to a stage temperature of 750 °C, which corresponded to a microelectrode temperature during probing of ~710 °C. A more detailed discussion of the temperature calibration is given in the Supplemental Information. The oxygen partial pressure (pO_2) in the chamber was varied over the range 10^{-3} atm - 1 atm by flowing bottled oxygen or oxygen-nitrogen mixtures through the chamber and then past a zirconia-based oxygen sensor (Setnag) housed in a quartz tube in a separate furnace. The pO_2 was allowed to stabilize at each condition prior to the acquisition of impedance measurements; typical stabilization times were 0.5 h - 3 h. The total pressure in the chamber was always 1 atm. The microelectrodes were contacted using a probe tip made of Paliney7, a commercial alloy containing 35% Pd, 30% Ag, 14% Cu, 10% Au, 10% Pt, 1% Zn (American Probe & Technologies, 20 μ m tip radius). Several measurements were repeated using a probe tip made of $Pt_{0.7}Ir_{0.3}$ (Moser, 10 μ m tip radius); identical impedance results were obtained. The former probe material was preferred because it did not scratch the microelectrodes.

Impedance spectra were acquired using a frequency response analyzer (Solartron Modulab) with an applied a.c. voltage of 30 mV, no applied d.c. bias, and a typical frequency range of 10 kHz - 16 MHz. As described in the Supplemental Information, cooling of the sample by the probe tip generated a temperature drop between the electrodes that has an associated 5 mV - 25 mV Seebeck voltage (with the exact value depending on the microelectrode diameter (Figure S19)), so in fact each impedance spectrum was effectively measured under 5 mV - 25 mV anodic d.c. bias, which was verified to be negligibly small for this material system. The analyzer calibration was verified in advance by acquiring impedance spectra from test circuits containing precision megaohm resistors and nanofarad capacitors; fits to these spectra reproduced the resistance and capacitance values with < 3% error. Impedance spectra acquired from the LSM microelectrodes were fit by an expression first suggested by Fleig et al.¹⁰ and described in detail below.

Morphological features were reexamined after impedance measurements. The sample surfaces were coated with a conductive layer of ~ 10 nm carbon (Cressington 108) and/or ~ 10 nm osmium and then characterized by scanning electron microscopy (SEM, Zeiss 1550 VP) and energy dispersive spectroscopy (EDS, Oxford X-Max SDD). Additionally, a protective layer of several hundred nm platinum was deposited in a few regions of each sample, and then cross-sections of these regions were prepared and imaged using focused ion beam (FIB) milling and SEM (FEI Helios Nanolab 600). The libraries were then characterized by optical profiling (New View 6000).

2.4 Results of Physical Characterization

X-ray diffraction patterns acquired after growth and prior to patterning are shown below. Figure 2.2a and Figure S20 show the results from the thickness libraries, Libraries #1 and #2. The patterns exhibit reflections that correspond primarily to (110)-oriented grains. Some intensity from (012) or (202) reflections is also evident. Figure 2.2b corresponds to Library #3, the growth temperature library. At growth temperatures of ~ 580 °C and lower, the XRD patterns show no reflections from the film, indicating those regions of the film are mostly amorphous. The possibility of slower film growth at those temperatures was ruled out by subsequent optical profiling, which indicated the film thickness was uniform throughout the sample. Moreover, the film color appeared uniform across the sample by visual inspection, consistent with a uniform thickness, whereas in other samples, decreased thickness gave rise to a lighter color. At growth temperatures of ~ 615 °C and higher, the films appear crystalline with similar orientations as measured from the thickness library.

Rocking curves obtained from Library #3 were best fit using two Voigt peaks, yielding two sets of FWHM values (Figure S21) and suggesting that the films had a thin epitaxial layer adjacent to the substrate and a thicker non-epitaxial layer elsewhere.

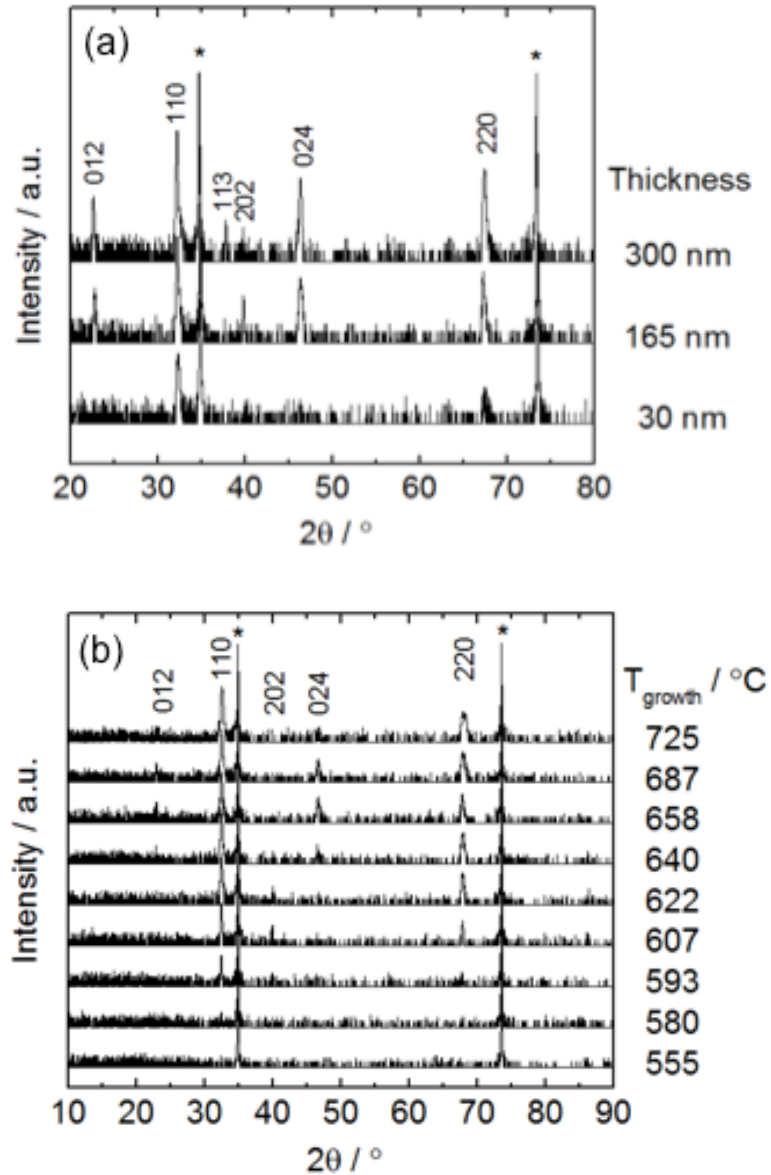


Figure 2.2. X-ray diffraction patterns acquired from various regions of two $(\text{La}_{0.8}\text{Sr}_{0.2})_{0.95}\text{MnO}_{3+\delta}$ thin film libraries: (a) Library #1, 30 - 300 nm thickness, 650 °C growth temperature, 10 mtorr O_2 growth pressure, 1 Hz laser pulse rate. (b) Library #3, 135 nm thickness, 555 - 725 °C growth temperature, 30 mtorr O_2 growth pressure, 5 Hz laser pulse rate. The orientation of each LSM reflection is indicated. Reflections marked with an asterisk are from the YSZ substrate.

After patterning each film, the layout shown in Figure 2.3 was obtained. The microelectrode diameters were measured by digital optical microscopy and found to be within 5% of the nominal diameters. As the microelectrode thickness increases from 30 nm to 150 nm, the microelectrodes become discernibly darker in color. Thickness increases past 150 nm are not discernible by eye. This effect is visible in Figure 2.3.

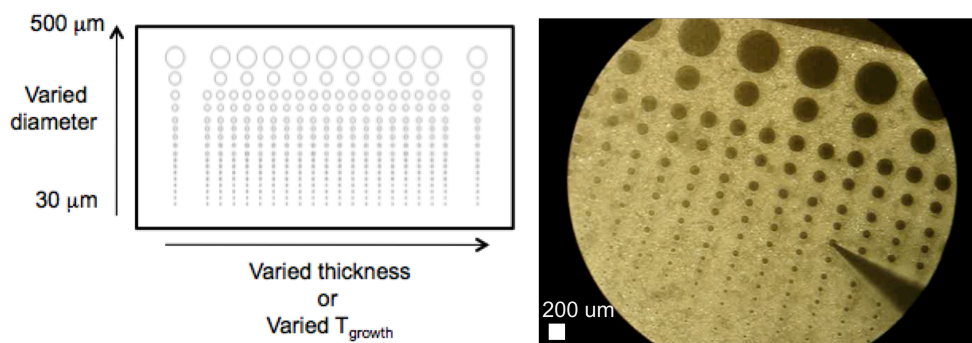


Figure 2.3. Typical library of $(\text{La}_{0.8}\text{Sr}_{0.2})_{0.95}\text{MnO}_{3+\delta}$ thin film microelectrodes grown on a 5 mm x 10 mm $\text{Y}_{0.15}\text{Zr}_{1.85}\text{O}_{1.93}$ substrate. Left: schematic layout. Right: optical photo of Library #1 during impedance measurements.

The microelectrode surfaces were characterized by AFM before and after patterning. No changes were observed due to the patterning. Micrographs taken after patterning are shown in Figure 2.4 and Figure S22 (for Libraries #1 and #2) and in Figure 2.5 (for Library #3). The grain size is seen to increase with increasing thickness (Figure 2.4 and Figure S22) or increasing growth temperature (Figure

2.5). Equivalently, the area density of exposed grain boundary length decreases with either increasing growth temperature or increasing thickness. These trends are consistent with findings from previous studies of oxide film growth.^{24,25}

Importantly, these grain size differences persisted throughout the impedance experiments. For example, the smaller grain sizes obtained from growth at 555 °C were retained even after days of subsequent annealing at 710 °C (Figure S23). This finding has two important implications. First, cation mobility is evidently faster during film growth at a certain temperature (in 10 mtorr O₂) than during subsequent anneals at the same temperature (in 1 torr O₂ - 760 torr O₂). Second, the thickness libraries and growth temperature library prepared in this work were also effectively "grain size libraries" with grain sizes that remained stable during the electrochemical impedance measurements.

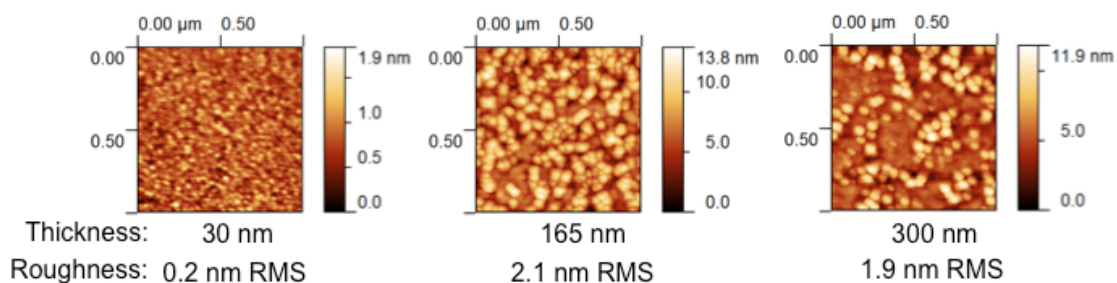


Figure 2.4. Atomic force micrographs acquired after patterning from a thickness library of $(\text{La}_{0.8}\text{Sr}_{0.2})_{0.95}\text{MnO}_{3+\delta}$ microelectrodes (Library #1, uniform 650 °C growth temperature). The corresponding thickness and root-mean-squared roughness are listed under each micrograph.

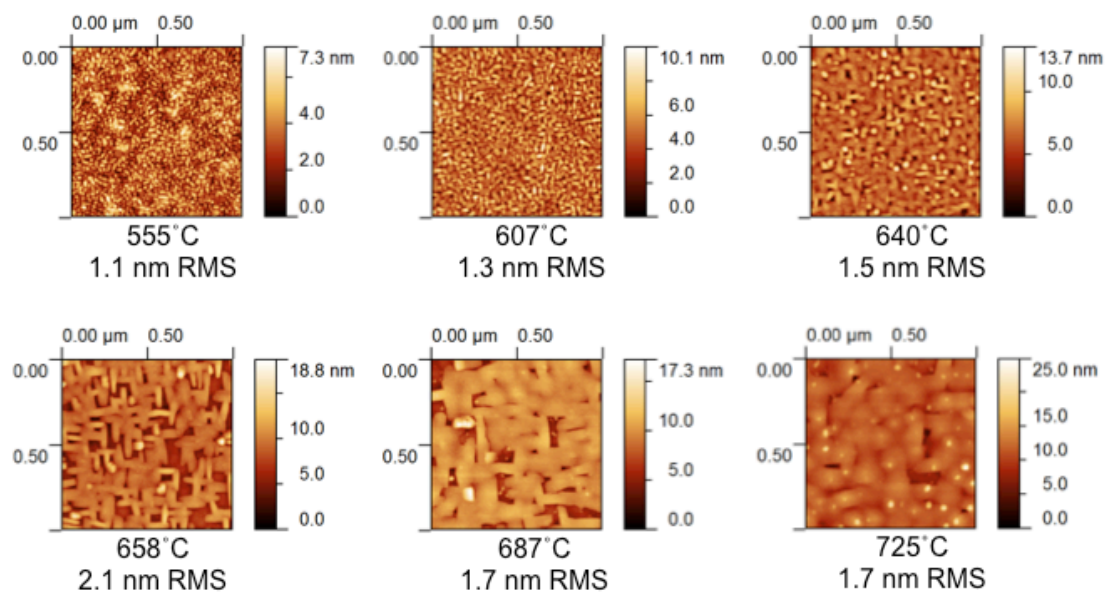


Figure 2.5. Atomic force micrographs acquired after patterning from a growth temperature library of $(\text{La}_{0.8}\text{Sr}_{0.2})_{0.95}\text{MnO}_{3+\delta}$ microelectrodes (Library #3, uniform 135 nm thickness). The corresponding growth temperature and root-mean-squared roughness are listed under each micrograph.

Cross-sectional FIB-SEM images (acquired after impedance testing from multiple regions in the libraries) indicated that the films were dense. A representative image is shown in Figure 2.6.

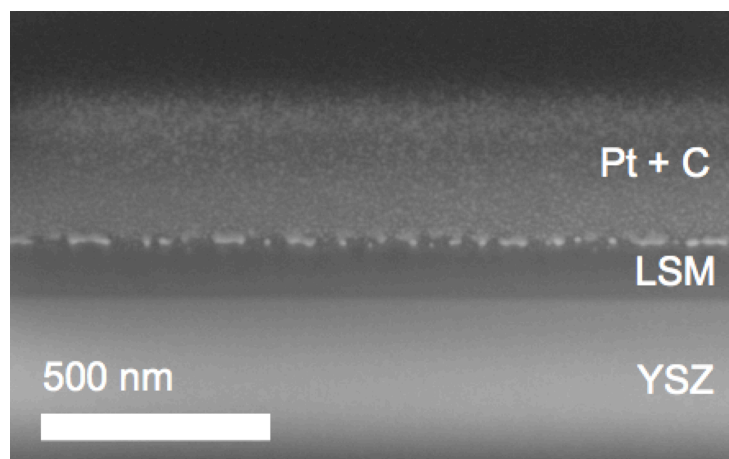


Figure 2.6. FIB-SEM cross-section acquired from a growth temperature library of $(\text{La}_{0.8}\text{Sr}_{0.2})_{0.95}\text{MnO}_{3+\delta}$ films (Library #3) after impedance testing. The sample was coated with conductive and protective layers of carbon and platinum prior to FIB milling to facilitate imaging. This image was acquired using a tilt angle of 52° off normal.

2.5 Results of Electrochemical Characterization

The reaction pathway posited in this study is shown in Figure 2.7. This pathway involves oxygen electro-reduction over the entire surface of the film, followed by ion diffusion through the film and into the electrolyte substrate.

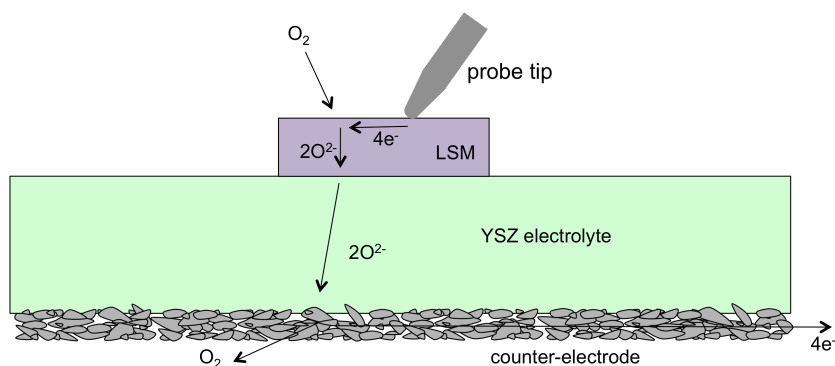


Figure 2.7. Schematic of a through-the-film reaction pathway.

It has been shown elsewhere that the electrochemical impedance response arising from 1D diffusion through a mixed ionic and electronic conductor (MIEC) can be rigorously mapped to an equivalent circuit based on a generalized transmission model.^{26,27} Here that result is modified to apply to the configuration in Figure 2.7 as follows: the LSM microelectrode film is treated as a MIEC; the resistance to bulk electron migration normal to the substrate is neglected in recognition of the high electronic conductivity of LSM; the LSM/YSZ interface is assumed to be reversible to ions and blocking to electrons, and thus is modeled by a simple (double-layer) electronic capacitance; and an additional resistance is added in series to account for bulk ion diffusion through the YSZ electrolyte and lateral electron migration (sheet resistance) from the probe tip to the surface reaction sites. Additionally, the impedance arcs measured at the lower frequencies in this study were consistently observed to be depressed relative to ideal semi-circles, suggesting a dispersion of time constants; this dispersion was accounted for by replacing the surface ionic capacitance with a constant phase element.

With these modifications in hand, the effective equivalent circuit is shown in Figure 2.8. This circuit is virtually identical to the one presented previously by Fleig et al.,¹⁰ except in that study a constant phase element was substituted for the interfacial electronic capacitance rather than the surface ionic capacitance. In the current study, that alternative circuit yielded poorer fits and unreasonably large confidence intervals.

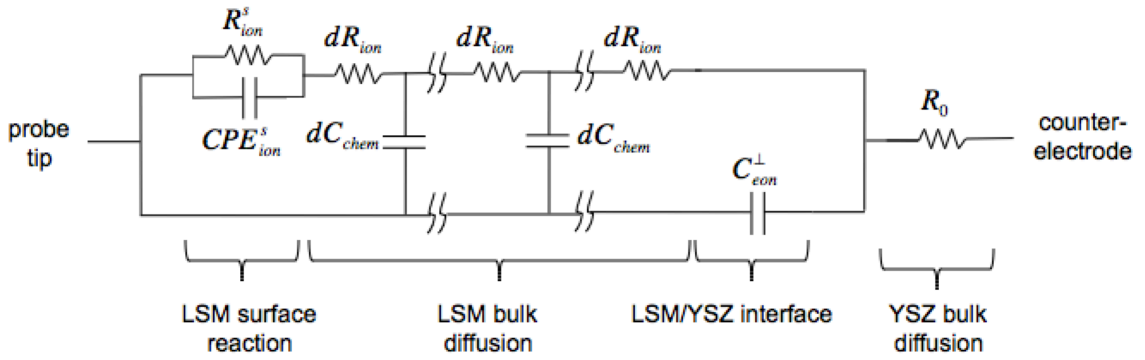


Figure 2.8. Equivalent circuit corresponding to the reaction pathway shown in Figure 2.7.

An analytical expression for the complex impedance of the equivalent circuit in Figure 2.8 can be derived using Kirchoff's Laws, as described previously.⁹ The result is:

$$Z = \frac{Z_1 Z_D + Z_D Z_A a \cdot \coth(a)}{Z_1 + Z_A Z_D a^2 / Z_1 + (Z_A + Z_D) a \cdot \coth(a)} + R_0 \quad (1)$$

where $Z_1 = R_{ion}$, $Z_D = \frac{1}{j\omega C_{eon}}$, $Z_A = \frac{R_{ion}^s}{1 + R_{ion}^s Y_{ion}^s (j\omega)^n}$, $a = \sqrt{j\omega R_{ion} C_{chem}}$, ω is the radial frequency, and $j = \sqrt{-1}$. The seven fit parameters in this model are R_{ion}^s , Y_{ion}^s , n , R_{ion} , C_{chem} , C_{eon} , and R_0 , which correspond to the LSM surface exchange resistance, the LSM surface ionic capacitance (in the form of a constant phase element magnitude and exponent), the LSM through-film oxygen ion diffusion resistance, the LSM chemical capacitance, the LSM/YSZ interfacial electronic capacitance, and the YSZ oxygen ion diffusion resistance. The other variables (Z_1 , Z_D , Z_A , and a) are merely placeholders that facilitate algebraic manipulations. After fitting, the effective surface ionic capacitance C_{ion}^s was calculated from the standard expression $C_{ion}^s = (Y_{ion}^s)^{1/n} R^{(1/n)-1}$. The data were fit by Equation 1 using complex nonlinear least squares, implemented in a custom Matlab routine. In the fitting routine, the residual of each complex impedance datum was weighted by the complex modulus of the datum. The initial values for the fit parameters were selected as described in the Supplemental Information.

Raw impedance spectra and the corresponding fit curves from a thickness library, Library #1, are shown in Figure 2.9. In the complex-plane plot, a large arc is observed at lower frequencies, and an additional smaller feature is observed at higher frequencies. These spectra appear quite similar to those observed by Fleig et al.¹⁰, and they are broadly similar to the spectra observed in other reports as well.²⁰⁻²² Note that at lower oxygen pressures, the two features are more distinct, while at higher oxygen pressures they begin to merge. Additional spectra and fits

from Library #1 are shown in Figure 2.10 as a function of film thickness. The low frequency arc clearly grows with increasing thickness, as observed by previous workers.

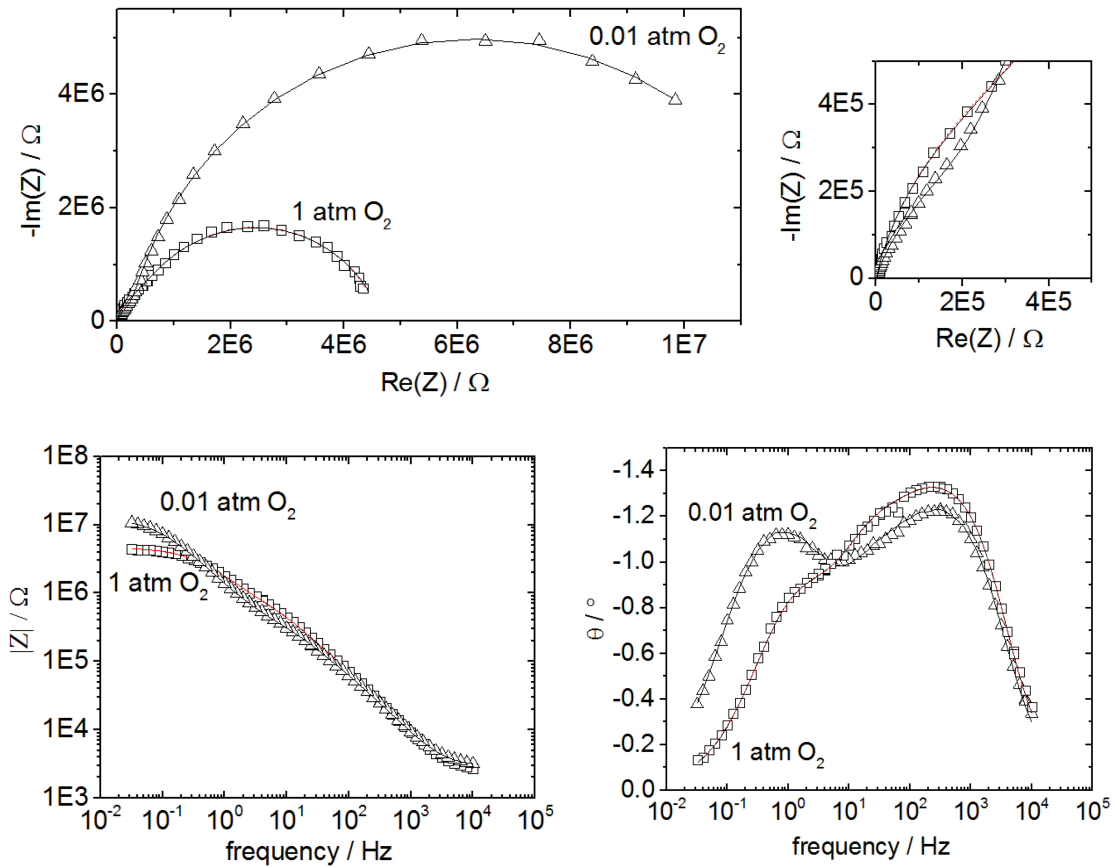


Figure 2.9. Typical impedance spectra (a), zoomed view of the same spectra (b), and gain/phase plots (c, d) plots acquired from $(\text{La}_{0.8}\text{Sr}_{0.2})_{0.95}\text{MnO}_{3+\delta}$ microelectrodes. Specific parameters for these spectra: Library #1, 200 μm diameter, 192 nm thickness, measured at $\sim 710^\circ\text{C}$ over the frequency range 10 kHz - 32 mHz. For the 1 atm O_2 data, the results from a full 7-parameter fit to Equation 1 (dashed red line) and a 6-parameter fit holding R_{ion} fixed (solid black line) are shown; they fall so closely on top of each other in these plots as to be indistinguishable.

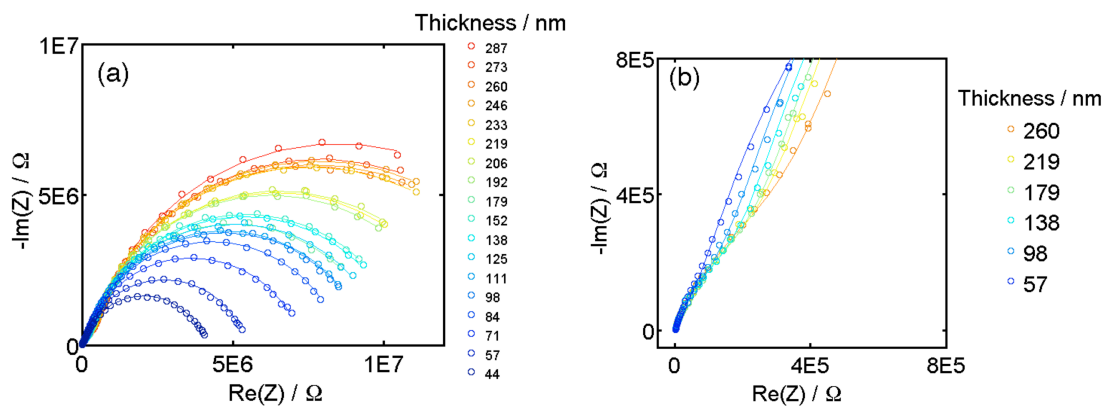


Figure 2.10. (a) Impedance spectra measured at ~ 710 °C and 0.01 atm O_2 from $\text{La}_{0.8}\text{Sr}_{0.2})_{0.95}\text{MnO}_{3+\delta}$ microelectrodes of various thicknesses in Library #1. (b) Zoomed view of a subset of the same spectra.

The exponent parameter of the constant phase element used to model the surface ionic capacitance was found to be ~ 0.7 and exhibited no trend with thickness or diameter (Figure S8). The diameter dependence of the other six fit parameters acquired from microelectrodes in the thickness library is shown in Figure 2.11. Considering first the parameter R_0 , Figure 2.11e, it is seen to scale approximately linearly with the inverse of the microelectrode diameter (log-log slope of -1), as expected if R_0 corresponds primarily to bulk diffusion of oxygen ions from a small working electrode through a (solid) electrolyte to a large counter electrode.²⁸ The slopes are actually slightly steeper than -1; this is attributed to the tip cooling effect discussed in the Supplemental Information. From the expression $\sigma = 1/(2dR_0)$, where d is the microelectrode diameter, the oxygen ion conductivity σ of the YSZ was estimated and found to be in reasonable agreement with the actual value.

The three capacitance parameters are seen to scale with the square of diameter, while the two other resistances scale approximately with the inverse square of diameter. This scaling behavior was observed previously¹⁰ and is consistent with the electrochemical pathway posited above, in which surface exchange occurs over the entire LSM surface and oxygen ion diffusion occurs primarily through the film. In contrast, a pathway mediated by the triple-phase-boundary (where the LSM, YSZ, and gas phases intersect) at the edge of the LSM would be expected to exhibit different scaling behavior.

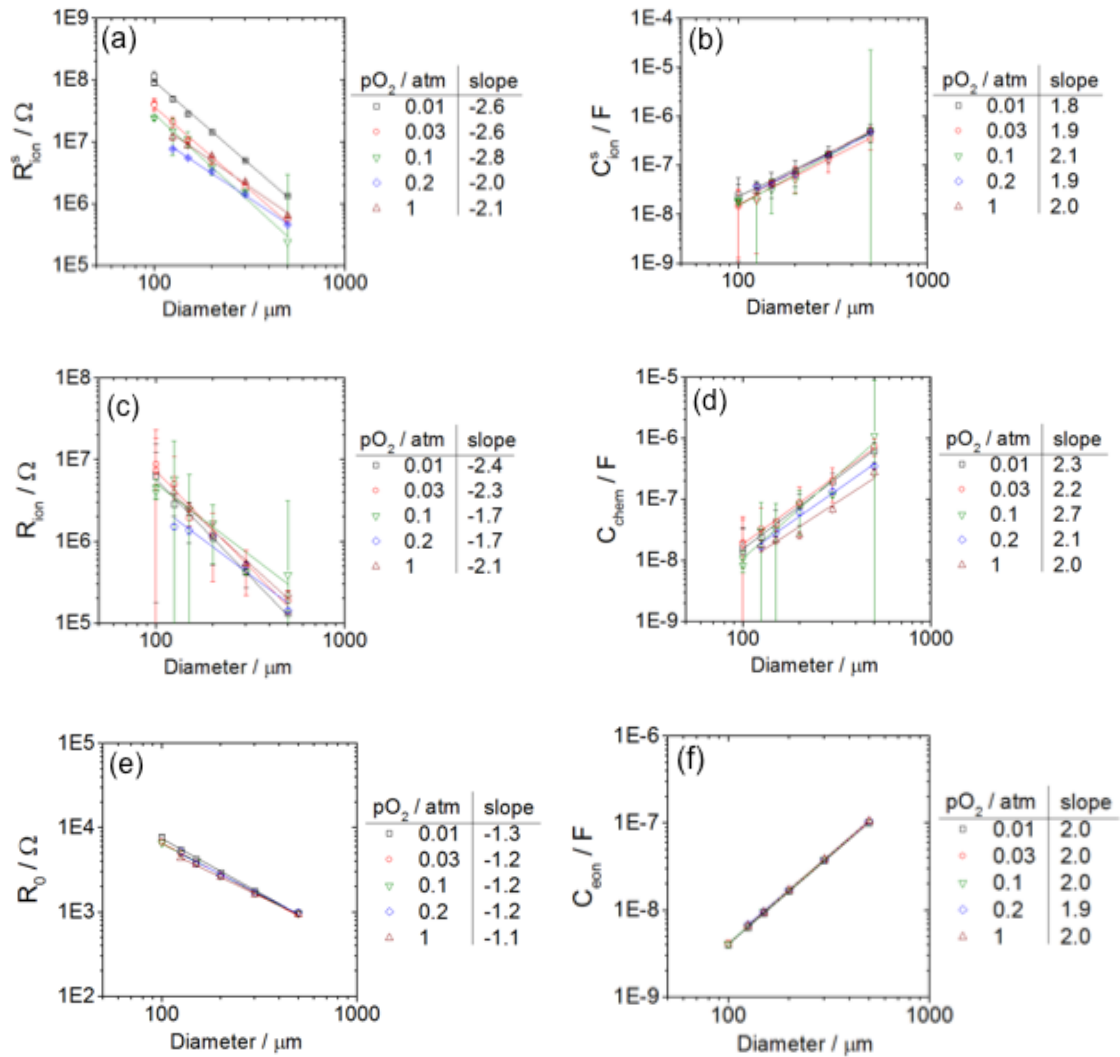


Figure 2.11. Diameter dependence of the six fit parameters measured from a thickness library of $(\text{La}_{0.8}\text{Sr}_{0.2})_{0.95}\text{MnO}_{3+\delta}$ films (Library #1) at ~ 710 °C under various oxygen partial pressures with 246 nm microelectrode thickness. The lines are linear fits, the slopes of which are indicated next to the legend. 95% confidence intervals from the fits are shown, except where they are smaller than the data points.

Further validation of the electrochemical model can be obtained by considering the thickness dependence of the fit parameters. In a preliminary set of fits, all seven parameters were allowed to vary, however the results obtained for R_{ion} and C_{chem} were unreasonably scattered at 0.2 atm and 1 atm (Figure S25). This increased scatter was also observed by other workers at ~ 800 °C, and it can be attributed to the increased overlap of the lower and higher frequency arcs.¹⁰ In other words, the characteristic frequencies of the surface exchange and bulk diffusion processes are close enough at 0.2 atm and 1 atm that the processes begin to be difficult to decouple by impedance spectroscopy. However, at the other pressures R_{ion} was seen to be insensitive to $p\text{O}_2$ (Figure S25), so taking advantage of this insensitivity, the fits at 1 atm O_2 and 0.2 atm O_2 were performed using a value of R_{ion} fixed at the average R_{ion} obtained for the same microelectrode at the lower oxygen pressures (0.01 atm, 0.03 atm, and 0.1 atm). The results are shown in Figure 2.12.

The fit results are physically reasonable. C_{eon} is seen to be essentially independent of thickness, as expected for an interfacial quantity. R_0 is largely independent of thickness, also as expected; the slight increase in R_0 for the thinnest films is attributed to a small contribution from electronic sheet resistance. This sheet resistance is expected to have a negligible impact on the other fit parameters, because those parameters correspond to processes whose characteristic frequencies are orders of magnitude slower.¹⁵ R_{ion} and C_{chem} are also seen to scale

linearly with thickness, as expected since these parameters correspond to the diffusion resistance through the film and the film's bulk chemical capacitance. The ambipolar diffusivity can be calculated from the expression $D_{\text{chem}} = L^2/(R_{\text{ion}}*C_{\text{chem}})$.²⁶ The calculated values were found to be nearly independent of thickness (Figure S26), so the values were averaged over all thicknesses. As shown in Figure 2.13a, the resulting values for D_{chem} are consistent with the range of values measured from $\text{La}_{0.8}\text{Sr}_{0.2}\text{MnO}_{3+\delta}$ bulk samples in a previous study.²⁹ This consistency provides further validation of the electrochemical model used in this study.

The volume-normalized chemical capacitance can be found from the slope of each isobaric linear fit in Figure 2.12d; this result is plotted in Figure 2.13b along with comparable values reported for bulk samples of $\text{La}_{0.8}\text{Sr}_{0.2}\text{MnO}_{3+\delta}$ and thin film samples of $(\text{La}_{0.8}\text{Sr}_{0.2})_{0.92}\text{MnO}_{3+\delta}$. The temperatures and compositions in this comparison are not identical, but nevertheless there is a strong indication that the chemical capacitance under the conditions studied is almost two orders of magnitude lower in the thin films than in bulk samples. In other words, the redox thermodynamics of LSM appear to be different in these films compared to bulk samples; the films are less easily reducible.

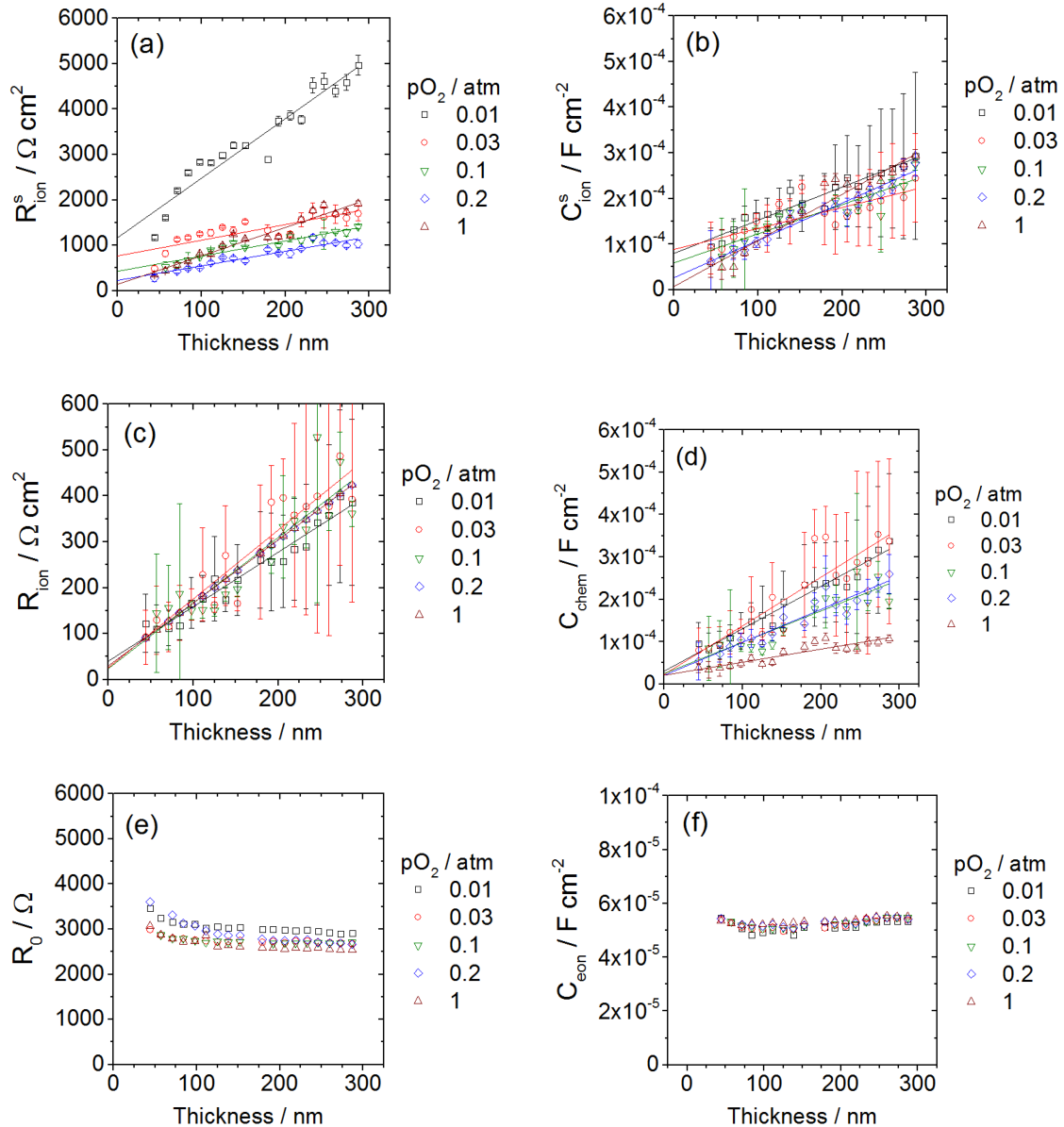


Figure 2.12. Thickness dependence of the six fit parameters measured from a thickness library of $(\text{La}_{0.8}\text{Sr}_{0.2})_{0.95}\text{MnO}_{3+\delta}$ films, Library #1, at ~ 710 °C and the indicated oxygen partial pressures. When fitting the spectra acquired under 0.2 atm O_2 and 1 atm O_2 , R_{ion} was held fixed at the value determined by averaging the R_{ion} values obtained from the fits to impedance spectra acquired from the same microelectrode at 0.01 atm O_2 , 0.03 atm O_2 , and 0.1 atm O_2 . 95% confidence intervals for the fits are shown, except where they are smaller than the data points.

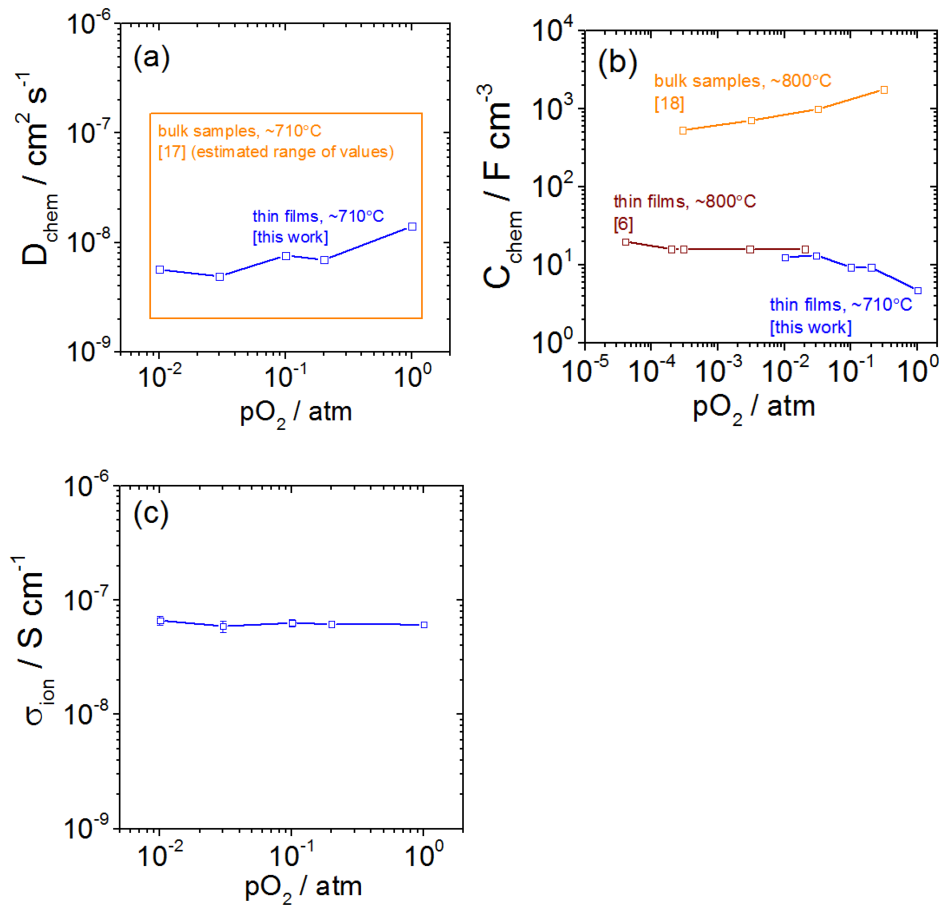


Figure 2.13. Ambipolar diffusivity D_{chem} (left) and volume-normalized chemical capacitance C_{chem} (right) of $(\text{La}_{0.8}\text{Sr}_{0.2})_{0.95}\text{MnO}_{3+\delta}$ at $\sim 710^\circ\text{C}$. The orange box bounds the range of values for D_{chem} previously measured from bulk samples of $\text{La}_{0.8}\text{Sr}_{0.2}\text{MnO}_{3+\delta}$.²⁹ Comparable literature data is also shown for C_{chem} .^{10,30}

Returning to the surface parameters in Figure 2.12, it is striking that the parameters R_{ion}^s and C_{ion}^s --- which represent the surface exchange resistance and the effective surface ionic capacitance --- exhibit a linear dependence on thickness. Apparently the surface is somehow changing with thickness in a way that impacts the surface exchange rate. Since the area density of grain boundaries at the surface is observed to decrease with increasing thickness (Figure 2.4), one can hypothesize that surface grain boundaries are more active than surface grains in these LSM films.

The growth temperature library, Library #3, provides an excellent test for this hypothesis, since in that library the surface density of grain boundaries varies substantially while the thickness is uniform. Impedance spectra acquired from that library are shown in Figure 2.14. Again a large arc is observed at lower frequencies, and an additional smaller arc is observed at higher frequencies. Both arcs increase in magnitude with increasing growth temperature.

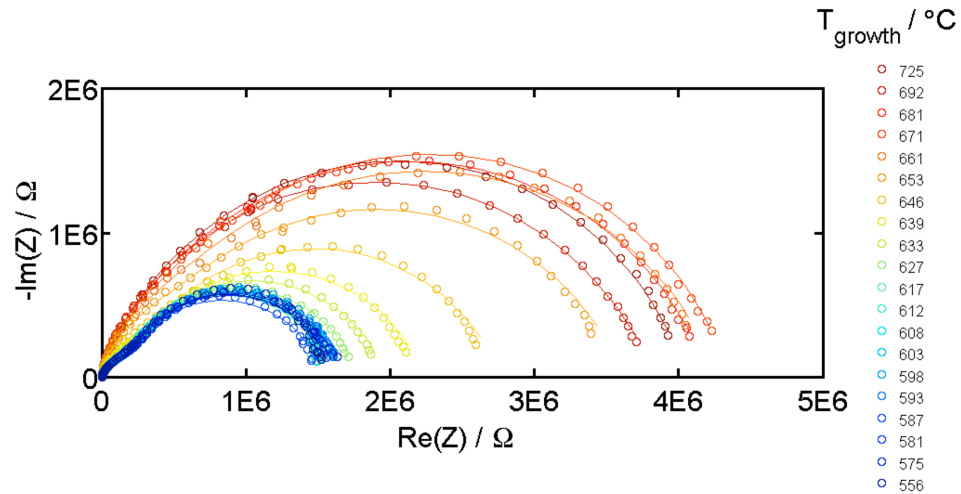


Figure 2.14. Impedance spectra acquired from the temperature-gradient $(\text{La}_{0.8}\text{Sr}_{0.2})_{0.95}\text{MnO}_{3+\delta}$ library under 0.2 atm O_2 , ~ 710 °C, 200 μm diameter electrodes, over the frequency range 10 kHz - 32 mHz. Points are raw data, curves are fits to Equation 1.

Circuit parameters extracted from fitting these spectra are shown in Figure 2.15. The surface exchange resistance R_{ion}^s tends to increase with increasing growth temperature, while the surface ionic capacitance C_{ion}^s tends to decrease, and the changes predominantly occur in the growth temperature range 630 - 680 °C, a range in which the grain size also increases substantially (Figure 2.5).

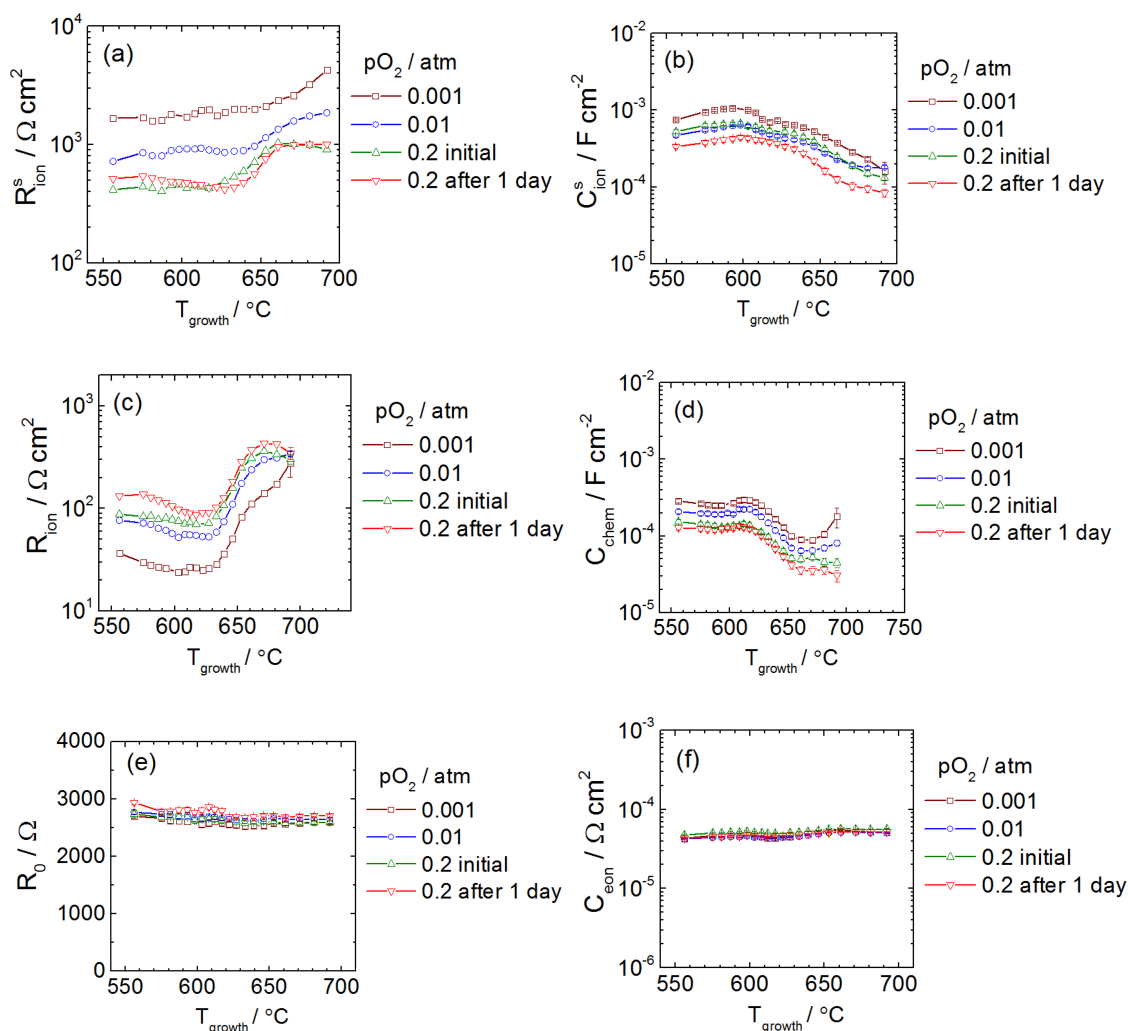


Figure 2.15. Fit parameters measured from the growth temperature library of $(\text{La}_{0.8}\text{Sr}_{0.2})_{0.95}\text{MnO}_{3+\delta}$ films, Library #3, at ~ 710 $^\circ\text{C}$ and the indicated $p\text{O}_2$. The microelectrode dimensions were 200 μm diameter and 135 nm thickness throughout. Lines connect the points as guides for the eye. 95% confidence intervals are shown, except where they are smaller than the data points.

To explore this correlation, the area density of grain boundary length on the film surfaces can be estimated from image analyses of AFM micrographs. Figure S27

shows an example of a processed image, and the extracted values are plotted as a function of growth temperature or thickness in Figure S28. The inverse of the LSM surface exchange resistance (which is a direct measure of surface activity) can then be plotted as a function of the area density of grain boundary length. The results are shown in Figure 2.16. For each library, the surface activity is seen to scale linearly with the area density of grain boundary length, indicating that the grain boundaries are more catalytically active than the grain surfaces. From the slopes of these trends, it can be estimated that the surface activity of an LSM film increases by $10^{-13} \Omega^{-1}$ per micron of added grain boundary length.

It is also notable that R_{ion} tends to increase and C_{chem} tends to decrease with increasing growth temperature (area density of grain boundary length). These trends suggest that the oxygen ion diffusivity may be higher along grain boundaries than through grains. This suggestion is consistent with previous work on bulk samples, in which SIMS measurements of oxygen tracer diffusion in $\text{La}_{0.8}\text{Sr}_{0.2}\text{MnO}_{3+\delta}$ found evidence of short circuit diffusion that was ascribed to fast diffusion along grain boundaries.³¹ However, despite the small confidence intervals obtained in these fits, we cannot entirely rule out the possibility that the R_{ion} and C_{chem} trends with growth temperature are fitting artifacts that arise from the increased overlap in characteristic frequencies of the surface and bulk processes.

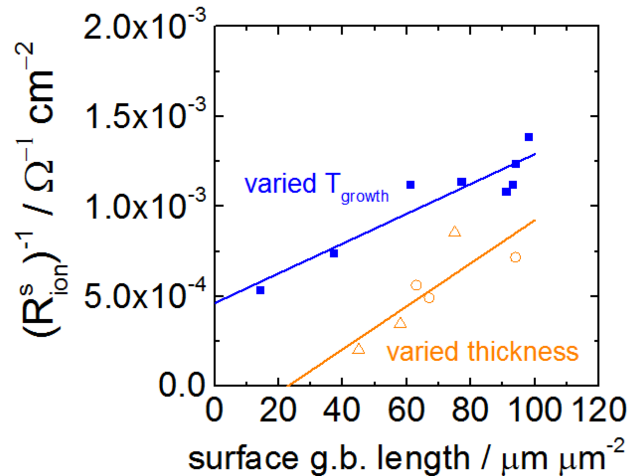


Figure 2.16. Electrochemical activity measured at ~ 710 °C under 0.01 atm O_2 from libraries of $(\text{La}_{0.8}\text{Sr}_{0.2})_{0.95}\text{MnO}_{3+\delta}$ microelectrodes with 200 μm diameter and various growth temperature (blue squares, 10 mtorr O_2 growth) or various thicknesses (orange, triangles and circles are samples grown in 30 mtorr O_2 and 10 mtorr O_2 , respectively).

2.6 Discussion

The finding that grain boundaries are correlated with improved surface activity of LSM films explains how the low frequency arc can correspond to the surface exchange process and simultaneously grow with increasing thickness. It also indicates that ion transport through such films is less limiting than many reports previously suggested.

An additional implication is that patterning LSM films by wet etching may lead to different results than patterning films by dry etching. Wet etchants typically

undercut the photoresist, such that at each etched edge, the film thickness tapers to zero over a tapered region that is roughly 10 μm wide.²³ This tapered region may comprise a significant fraction of the total area, e.g., for a 100 μm circular microelectrode, a tapered edge region of width 10 μm would span roughly one third of the total surface area and, based on the results presented above, the tapered region could have a higher density of exposed grain boundaries and a higher surface activity. A second enhancement may arise because electrodes produced by wet etching are effectively acid etched in the tapered edge region, and acid etching has been observed to significantly improve the activity of MIEC electrodes made of materials like LSM and LSC.^{32,33} These enhancements were avoided in the current study by patterning the films using dry etching (argon ion milling), which yielded a sharper edge with no acid exposure (Figure S30).

Returning to Figure 2.16, it is apparent that although the trends of activity with exposed grain boundary length are similar between the two types of libraries, the trends have different intercepts, such that the absolute magnitude of the surface activity is different by approximately a factor of 2. The origin of this performance difference between the two types of libraries is unclear. Comparable batch-to-batch performance variations have sometimes been observed in previous studies of films grown by pulsed laser deposition.³⁴ To help pin down the origin of this factor of 2, a second thickness library was grown under 30 mtorr O_2 pressure, patterned, and then characterized. The results from this library are plotted in Figure 2.16 and Figure S31 and are quite similar to the thickness library grown

under 10 mtorr O₂, indicating that small differences in oxygen partial pressure during growth are unlikely to be the origin of the factor of 2. The microelectrodes in this second thickness library also exhibited stable surface activity over the ~50 h time period in which the measurements were acquired (Figure S31) so the factor of 2 does not appear to originate from non-stationary behavior of the surfaces during the impedance measurements. It is notable that the growth temperature library was grown with an ablation laser pulse rate of 5 Hz, while the thickness libraries used 1 Hz. One can speculate that the faster growth rate led to the higher surface activity, perhaps by influencing the extent to which cations and impurities were able to segregate to the surface during growth.

2.7 Conclusion

A scanning impedance probe was developed that can measure the electrochemical impedance response of hundreds of thin film microelectrodes in automated fashion. This instrument was used to characterize libraries of LSM microelectrodes with systematically varied diameter and either thickness or growth temperature. The electrochemical impedance response of all microelectrodes at ~710 °C was found to be well fit by a physically derived equivalent circuit, and all trends were consistent with a pathway involving oxygen reduction over the entire surface of the LSM microelectrode followed by diffusion through the film and into the YSZ electrolyte. The surface activity was found to scale linearly with the area density of grain boundary length on the LSM microelectrode surface, suggesting that grain boundaries are more active than grains towards the rate-limiting surface step. This

finding suggests that increasing the area density of exposed grain boundary length in a practical LSM-based electrode could lead to substantial improvements in activity.

Chapter 2 Supplemental Information

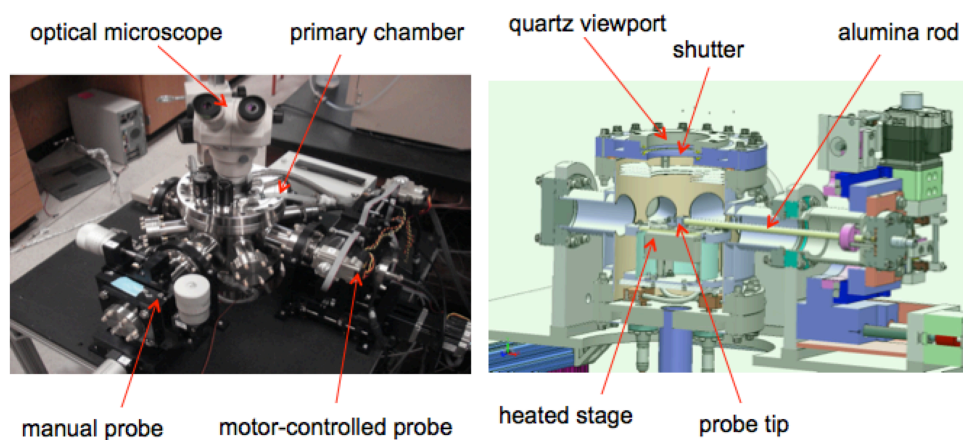


Figure S17. Primary chamber of the scanning impedance probe. Left: external photo. Right: computer model cross-section showing the chamber interior.

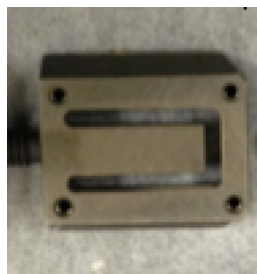


Figure S18. Optical photo of the stage used to asymmetrically heat substrates during preparation of the library of growth temperatures.

Temperature calibration

The samples were heated from below, so the metal probe tip was cooler than the sample and thus the probe tip cooled the microelectrode by conduction during each impedance measurement. The smaller the microelectrode diameter, the more the average microelectrode temperature is expected to be lowered by tip cooling. This effect was first reported by Opitz and Fleig in 2010;³⁵ it appears to have been neglected in many reports using microelectrodes published before then.

Opitz and Fleig also observed that the associated temperature drop between the counter electrode and the microelectrode generates a measurable Seebeck voltage.³⁵ From this temperature drop across the substrate and the substrate Seebeck coefficient (~ 0.5 mV/K for YSZ³⁶), the actual average microelectrode temperature can be estimated. Typical results measured in the current work are shown Figure S19. It is noteworthy that the cooling is not instantaneous; rather, the thermovoltage typically took 5 s - 180 s to stabilize, with the faster times corresponding to the higher temperatures or larger diameters. The observed thermovoltage also varied slightly between measurements, and larger thermovoltages were observed when contacting metal microelectrodes than when contacting the oxide microelectrodes used in this study. These effects are likely both explained by differences in thermomechanical contact and thermal conductivity at the contact point. In addition, besides the temperature drop between the electrodes, there is an additional small temperature drop between the heated stage surface and the sample counter electrode. This drop was measured separately using representative substrates and thin thermocouples.

In summary, with a stage temperature setpoint of 750 °C the average actual temperature of the microelectrodes under test was estimated as ranging from ~700 °C (for 100 μm diameter) up to ~720 °C (for 500 μm diameter).

In Figure 2.11 the deviations in the log-log relationships from the expected slope of -2.0 are attributed primarily to the temperature effects described above. Note that this tip cooling effect is not expected to significantly distort any of the other impedance trends reported in this work, since apart from Figure 2.11 only microelectrodes with 200 μm diameter were measured.

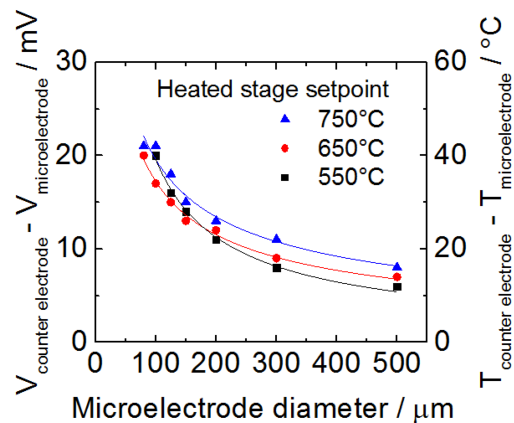


Figure S19. Seebeck voltage measured between the counter electrode and an oxide microelectrode contacted by a Paliney7 probe tip. Rescaling the voltage by the Seebeck coefficient of YSZ yields an estimate for the associated temperature drop between the electrodes, also shown. Curves are power-law fits to the data at each temperature.

Sources of uncertainty in tip position

The total tolerance in tip position that the scanning impedance probe can achieve includes several contributions with the following estimated magnitudes: the photolithography method used to pattern the films ($\pm 5 \mu\text{m}$); the manual process of visually identifying reference points ($\pm 10 \mu\text{m}$); the stepper motor positioning accuracy ($\pm 1 \mu\text{m}$); creep of the Paliney7 probe tip at high temperatures ($\pm 10 \mu\text{m}$); deflection of the tip due to contact forces with the substrate ($\pm 10 \mu\text{m}$). The resulting total tolerance in tip position motivated the use of microelectrodes with sufficiently large diameter ($\geq 100 \mu\text{m}$) so as to ensure that reliable electrical contact could be achieved throughout the study. $\text{Pt}_{0.7}\text{Ir}_{0.3}$ probe tips exhibited reduced creep and deflection but typically scratched the films at elevated temperature. By reducing the above tolerances it should be possible in future studies to reliably contact microelectrodes with smaller diameters.

Fitting routine: Choosing the initial values

Depending on the initial values chosen for the fit parameters, the fitting routine sometimes either failed to converge or converged to a solution with unreasonably large confidence intervals for all parameters. It was found that these convergence problems could mostly be avoided by taking as the initial value of each fit parameter the median result for that parameter from preliminary fits to the same

spectra that were performed using plausible but otherwise somewhat arbitrary initial values.

Additional Figures

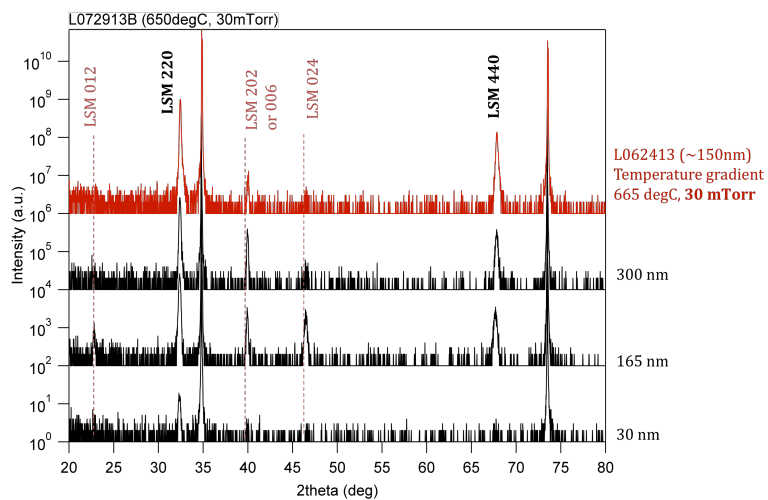


Figure S20. XRD patterns acquired from a thickness library of $(\text{La}_{0.8}\text{Sr}_{0.2})_{0.95}\text{MnO}_{3+\delta}$ microelectrodes, Library #2, grown at 650 °C under 10 mtorr O_2 . The corresponding film thickness is listed to the right of each pattern. The orientation of each LSM reflection is also indicated. Reflections marked with an asterisk are from the YSZ substrate.

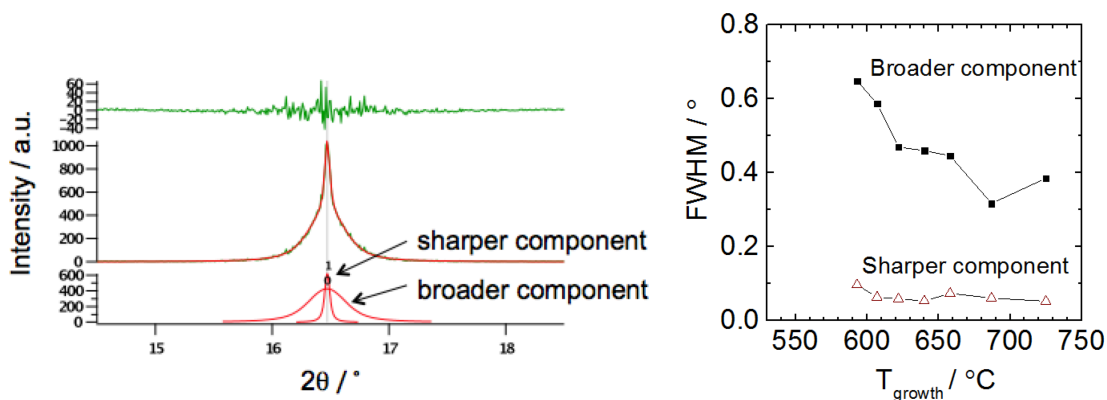


Figure S21. Left: Typical rocking curve acquired from the $(\text{La}_{0.8}\text{Sr}_{0.2})_{0.95}\text{MnO}_{3+\delta}$ growth temperature library in a region where $T_{\text{growth}} = 725 \text{ }^\circ\text{C}$. The two fit components are shown in red at bottom; the fit residual is shown in green at top. Right: Full width at half maximum (FWHM) values extracted from the rocking curves.

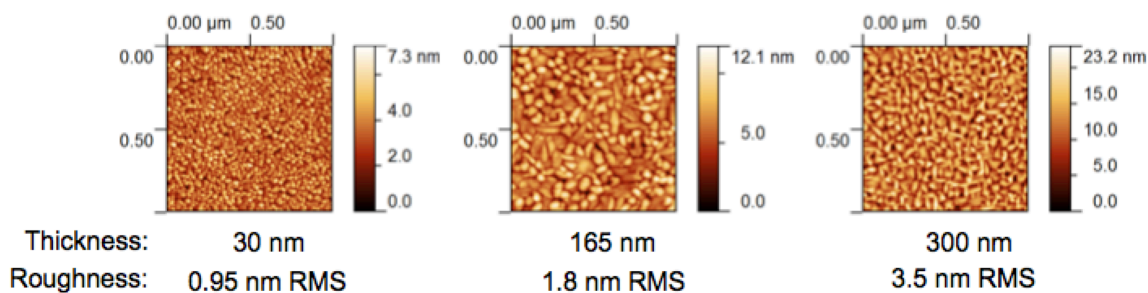


Figure S22. AFM images acquired after patterning from a follow-up thickness library of $(\text{La}_{0.8}\text{Sr}_{0.2})_{0.95}\text{MnO}_{3+\delta}$ microelectrodes grown at $650 \text{ }^\circ\text{C}$ under 10 mtorr O_2 . The corresponding film thickness and root-mean-squared roughness are listed under each micrograph.

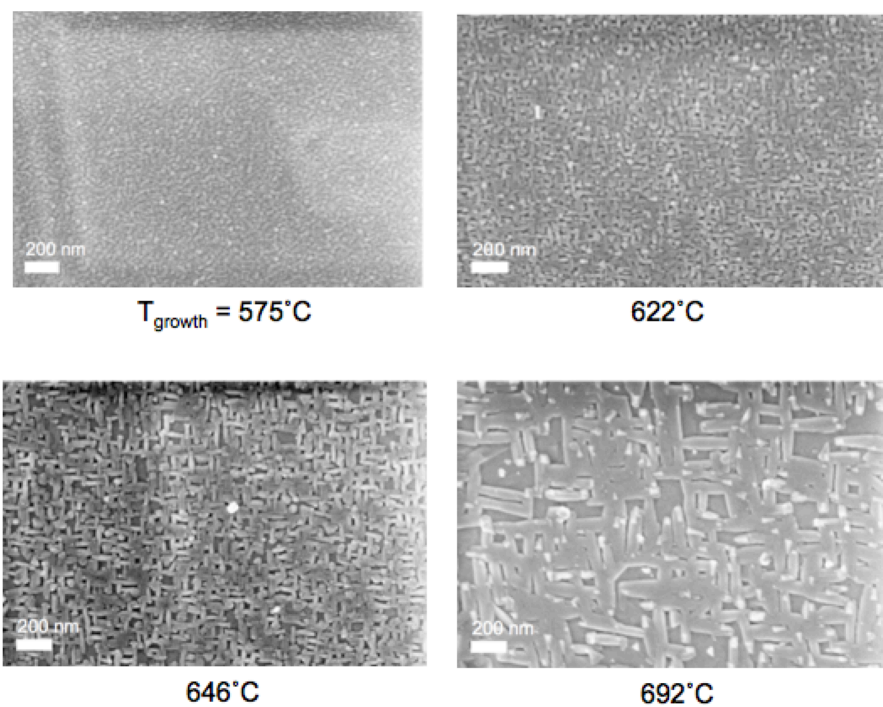


Figure S23. SEM images from the $(\text{La}_{0.8}\text{Sr}_{0.2})_{0.95}\text{MnO}_{3+\delta}$ growth temperature library after exposure for 2 days at $\sim 710^{\circ}\text{C}$ in the scanning impedance probe. Some of the observed contrast is due to mild sample charging.

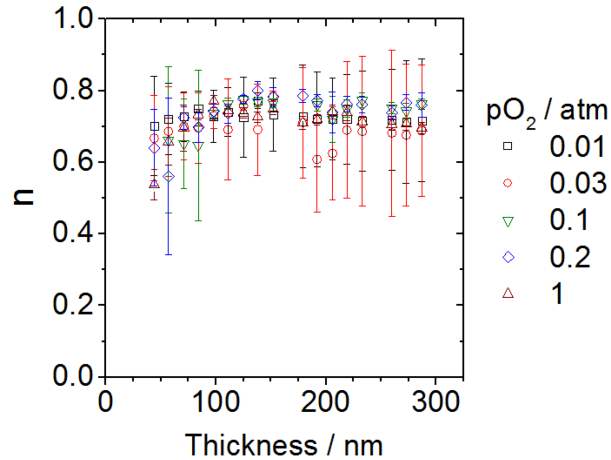


Figure S24. Exponent of the constant phase element used to represent the surface capacitance (C_{ion}^s) when fitting impedance spectra acquired from the thickness library at ~ 710 °C, 200 μm diameter to the model shown in Equation 1. 95% confidence intervals are shown.

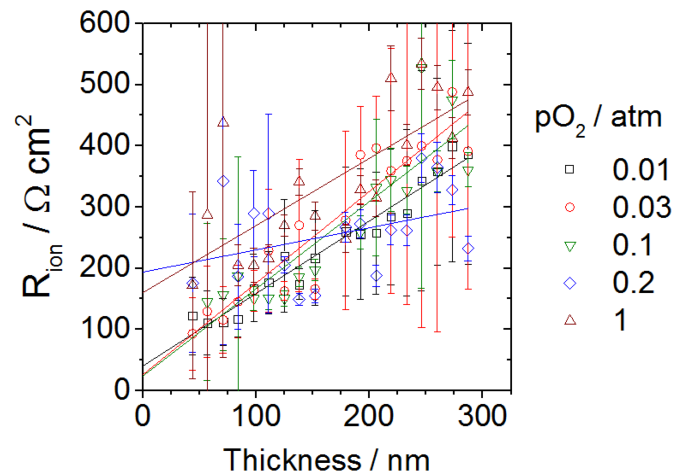


Figure S25. Thickness dependence of the fit parameter R_{ion} measured from the $(\text{La}_{0.8}\text{Sr}_{0.2})_{0.95}\text{MnO}_{3+\delta}$ thickness library at ~ 710 °C at various oxygen partial pressures. This plot is identical to the plot of R_{ion} in Figure 2.12, except here all seven parameters were free to vary in all fits, including the 0.2 atm and 1 atm fits. 95% confidence intervals are shown.

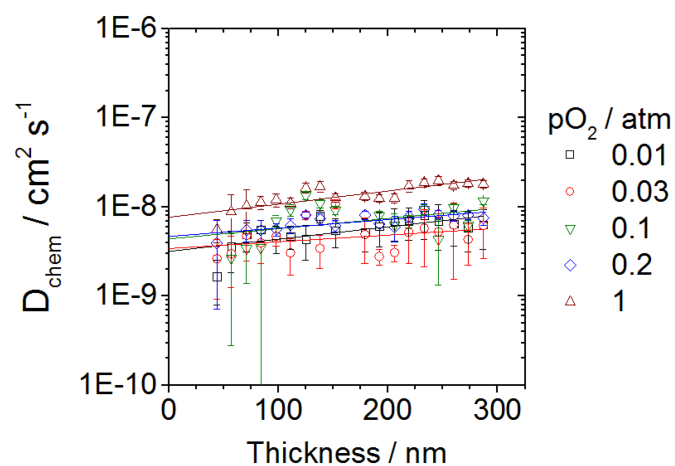


Figure S26. Thickness dependence of the ambipolar diffusivity D_{chem} calculated from the $(\text{La}_{0.8}\text{Sr}_{0.2})_{0.95}\text{MnO}_{3+\delta}$ thickness trends shown in Figure 2.12 for $\sim 710^\circ\text{C}$. 95% confidence intervals are shown. (They are artificially small for the 0.2 atm and 1 atm isobars, since R_{ion} was held fixed in those fits.)

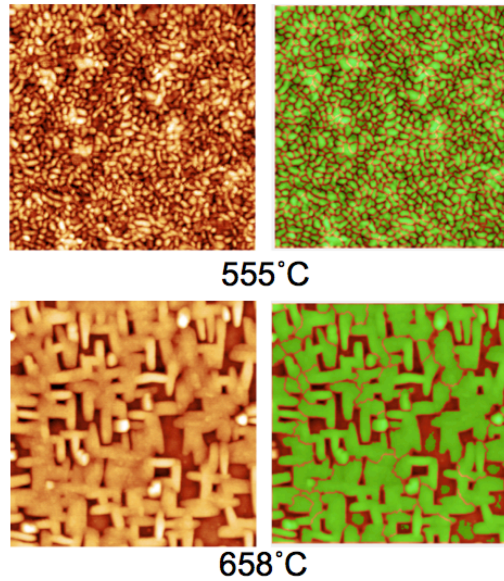


Figure S27. Typical images used to estimate the surface grain boundary length. Films grown at two different temperatures are shown. Left: AFM micrographs. Right: Same micrographs after image processing. The surface grain boundary length was estimated by summing the length of the borders between the green regions.

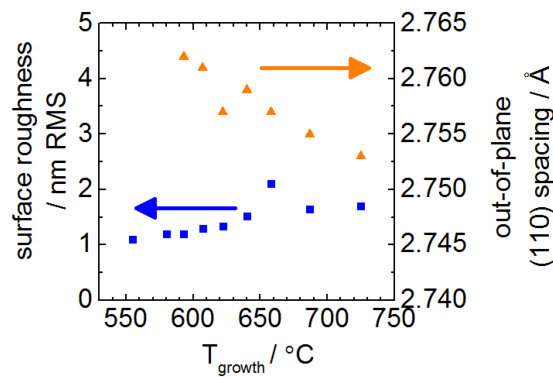


Figure S28. Surface roughness and out-of-plane (110) plane spacing measured from the as-grown $(\text{La}_{0.8}\text{Sr}_{0.2})_{0.95}\text{MnO}_{3+\delta}$ temperature library using AFM, XRD, and AFM, respectively.

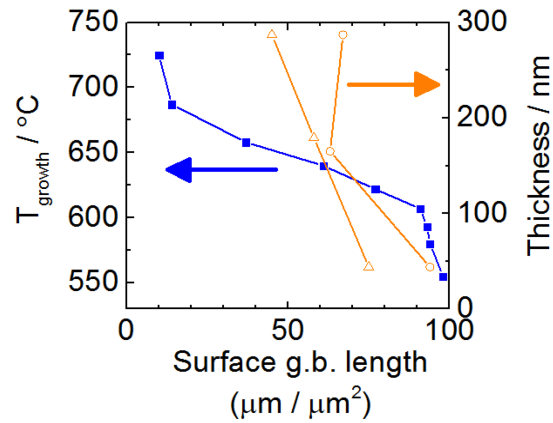


Figure S29. Surface grain boundary length estimated using AFM images from the growth temperature library (blue) and two thickness libraries grown at 10 mtorr O₂ (circles) and 30 mtorr O₂ (triangles).

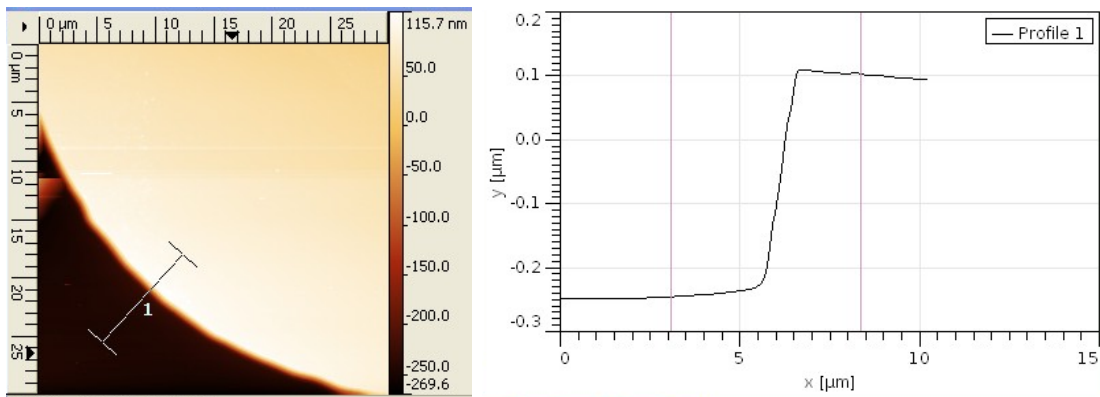


Figure S30. Example edge profile of an LSM microelectrode prepared by dry etching. This particular profile was acquired from an 80 μm diameter microelectrode in Library #1.

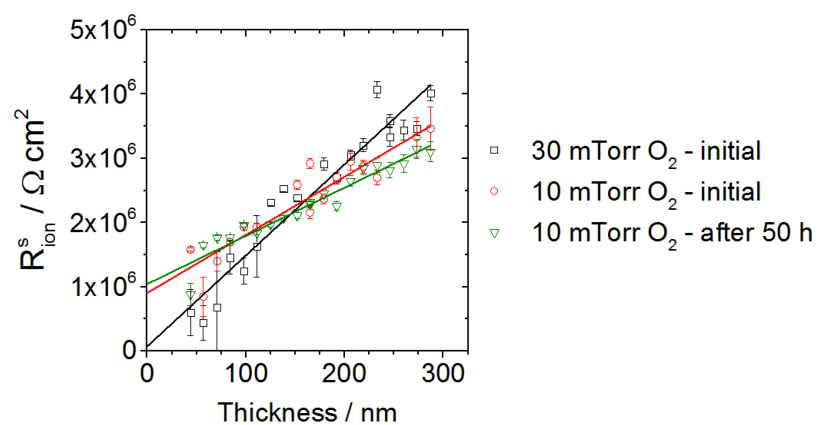


Figure S31. Surface resistance R_{ion}^s extracted from impedance spectra at 710 °C in 0.2 atm O_2 using 200 μm diameter microelectrodes from two thickness-gradient libraries grown on different substrates and measured separately. 95% confidence intervals are shown. Lines are linear fits.

CHAPTER 3 HIGH THROUGHPUT CHARACTERIZATION OF TWO OTHER MATERIAL SYSTEMS: $\text{La}_{0.5}\text{Sr}_{0.5}\text{CoO}_{3+\delta}$ AND PLATINUM - $\text{Sr}_{0.06}\text{Nb}_{0.06}\text{Bi}_{1.87}\text{O}_3$

3.1 Summary

This chapter describes characterization results obtained from thin film microelectrodes of two other material systems: $\text{La}_{0.5}\text{Sr}_{0.5}\text{CoO}_{3+\delta}$ (LSC), and a composite of metal and doped bismuth oxide (platinum - $\text{Sr}_{0.06}\text{Nb}_{0.06}\text{Bi}_{1.87}\text{O}_3$). Some background about these systems is given in Section 3.2. The experimental preparation of these samples is detailed in Section 3.3. Electrochemical pathways and the corresponding equivalent circuits are described in Section 3.4. Results and discussion are presented for $\text{La}_{0.5}\text{Sr}_{0.5}\text{CoO}_{3+\delta}$ (LSC) in Section 3.5, and for platinum on $\text{Sr}_{0.06}\text{Nb}_{0.06}\text{Bi}_{1.87}\text{O}_3$ in Section 3.6. Overall conclusions are given in Section 3.7.

3.2 Two material systems

The cathode materials used in state-of-the-art solid oxide fuel cells typically fall into three categories:

- (1) $\text{La}_{1-x}\text{Sr}_x\text{MnO}_3$, often with a small amount of A-site deficiency
- (2) Perovskites or double-perovskites that contain Sr and Co
- (3) doped Bi_2O_3

The first category, cathodes based on $\text{La}_{1-x}\text{Sr}_x\text{MnO}_3$ (LSM), was discussed in the previous chapter. In the second category, cells with a peak power density greater

than 1 W/cm² at 600°C (using H₂ as the fuel) have been reported using cathodes containing Ba_{0.5}Sr_{0.5}Co_{0.8}Fe_{0.2}O_{3-δ} (BSCF),^{37,38} Sm_{0.6}Sr_{0.4}CoO_{3-δ} (SSC),³⁹ La_{0.58}Sr_{0.4}CoO_{3-δ} (LSC),⁴⁰ PrBa_{0.5}Sr_{0.5}Co_{1.5}Fe_{0.5}O_{3-δ} (PBSCF),⁴¹ and Sr_{0.5}Co_{0.9}Nb_{0.1}O_{3-δ} (SCN).⁴² In the third category, it is not as widely recognized that doped Bi₂O₃ is electrochemically active for oxygen reduction, however cells with peak power density greater than 1 W/cm² at 650°C have been reported using a composite cathode of Er_{0.4}Bi_{1.6}O₃ - Bi₂Ru₂O₇.⁴³ In light of their high activity and relevance in applications, representative materials from the second and third categories are studied in this chapter. The selected materials are La_{0.5}Sr_{0.5}CoO₃ and metal-Sr_{0.06}Nb_{0.06}Bi_{1.87}O₃.

3.2.1 La_{0.5}Sr_{0.5}CoO₃

There is a general consensus that La_{0.5}Sr_{0.5}CoO₃ (LSC) and similar compositions are quite catalytically active for the oxygen electro-reduction reaction $O_2 + 4e^- = 2O^{2-}$. The absolute magnitude of the surface activity varies substantially between reports, however, and the stability of the activity is also not well-understood. Some studies simply state that the activity of LSC films degrades substantially over a period of tens of hours;^{33,44-46} in other studies stability is implied but not explored.⁴⁷⁻⁴⁹ There is also disagreement about the redox behavior of LSC films. One metric for the reducibility of a non-stoichiometric oxide is the chemical capacitance C_{chem} :

$$C_{chem} = \frac{-8e^2V}{k_B TV_m} \frac{\partial \delta}{\partial (\ln(pO_2/atm))} \quad (3)$$

where e is the charge of an electron, V is sample volume, V_m is molar volume, k_B is Boltzmann's constant, T is temperature, δ is oxygen non-stoichiometry, and pO_2 is oxygen partial pressure. If decreasing the oxygen partial pressure causes a large increase in δ , then C_{chem} is large; thus C_{chem} can be considered a measure of how easily a material is reduced. By this metric, some researchers report that LSC films are less reducible than bulk samples,⁵⁰ while others find the opposite.¹¹

3.2.2 $Sr_{0.06}Nb_{0.06}Bi_{1.87}O_3$

The catalytic activity of doped bismuth oxides towards oxygen reduction is much less widely recognized than in perovskites containing manganese or cobalt. In fact, doped bismuth oxides as cathodes were largely ignored in two recent reviews of solid oxide fuel cell materials.^{51,52} The high activity was first reported in 1983, however, when Verkerk *et al.* observed an electrode resistance "many times lower" for metal- $Er_xBi_{2-x}O_3$ cathodes than for comparable metal- $Gd_{0.10}Ce_{0.90}O_2$ cathodes.⁵³ They also observed that the surface exchange resistance of platinum electrodes on doped zirconia and ceria substrates exhibited a minimum at roughly 10^{-2} atm O_2 , whereas platinum electrodes on doped bismuth oxide substrates exhibited no such minimum. And, they observed that the activation energies obtained from sputtered gold electrodes and sputtered platinum electrodes were comparable on doped bismuth oxide but very different on doped zirconia or doped ceria. Based on these

observations, they concluded that doped bismuth oxide has enough catalytic activity that the catalysis is limited by oxygen adsorption and/or diffusion on the oxide surface, not on adjacent metal surfaces, even if the metal is platinum. Follow-up studies reached similar conclusions.⁵⁴

Many dopants have been explored, because in pure Bi_2O_3 the high-ionic-conductivity (face centered cubic) δ phase is stable only in the range $729^\circ\text{C} - 824^\circ\text{C}$. Above that range the material melts; below that range the material converts to a monoclinic α phase with much lower ionic conductivity, a transition that involves a large volume change that typically leads to severe cracking. In general increasing the dopant concentration lowers both the phase transition temperature and the ionic conductivity.^{55,56}

However, the activity of doped bismuth oxide is not accurately known for any combination of dopants. The stability of these compounds is also not clearly understood, although in many cases, a slow degradation in transport rates has been observed when the materials are annealed for many days, and in some cases this degradation has been correlated with either a slow phase transformation, cation ordering, anion ordering, and/or cation exsolution.⁵⁷

Here a new composition is measured, $\text{Sr}_{0.06}\text{Nb}_{0.06}\text{Bi}_{1.87}\text{O}_3$, to determine its activity and to assess its stability.

3.3 Experimental details

3.3.1 Target preparation

A PLD target with nominal composition $\text{La}_{0.5}\text{Sr}_{0.5}\text{CoO}_3$ was prepared in-house by mixing the appropriate ratios of $\text{La}_2(\text{CO}_3)_2 \cdot 7.8\text{H}_2\text{O}$ (Alfa 99.9%), SrCO_3 (Aldrich 99.9%), and CoO (Alfa 99.998%) using a mortar and pestle and then sintering 10 h at 1250°C .

Substrates (10 mm x 10 mm x 1 mm) and PLD targets (25 mm diameter) with nominal compositions $\text{Y}_{0.5}\text{Bi}_{1.5}\text{O}_3$ (YB) and $\text{Sr}_{0.06}\text{Nb}_{0.06}\text{Bi}_{1.87}\text{O}_3$ (SNB) were prepared by the group of Professor Kuan-Zong Fung at the National Central University of Taiwan. According to that group, the pellets were prepared by mixing the appropriate ratios of Bi_2O_3 , Y_2O_3 , SrCO_3 , and Nb_2O_5 by ball milling for 24 h, sieving with 325 mesh, calcining at 850°C (YB) or 750°C (SNB), ball milling again, uniaxial pressing, isostatic pressing, sintering at 950°C (YB) or 850°C (SNB), and then grinding and polishing to a mirror finish using alumina grit.

No unexpected reflections were detected by XRD for any of these targets. The cation ratio in a representative YB pellet was measured by EDS; it precisely matched the expected ratio. The LSC target appeared to have some porosity, roughly 30% - 50%.

3.3.2 Film preparation

Using the above targets, $\text{La}_{0.5}\text{Sr}_{0.5}\text{CoO}_3$ films were grown on (100) single crystal $\text{Y}_{0.15}\text{Zr}_{1.85}\text{O}_{1.93}$ (YSZ, 8 mol% Y_2O_3 -stabilized ZrO_2) substrates by Shingo Maruyama using pulsed laser deposition at the University of Maryland. For LSC the growth used a KrF excimer laser (248 nm, $\sim 0.5 \text{ J cm}^{-2}$, 5 Hz), a growth pressure of 30 mtorr O_2 , a substrate temperature of 640°C (measured with a pyrometer), a calculated deposition rate of 2.3 nm/min, and a cooling rate of $\sim 100^\circ\text{C}$. During all growth steps, the substrate backsides were adhered to a stage with silver paste, which was subsequently scraped off.

The as-grown LSC films were characterized by x-ray diffraction (XRD, Bruker D8 Discover, $\text{Cu K}\alpha$) and atomic force microscopy (AFM, Digital Instruments Nanoscope III). Patterning was carried out by spin coating photoresist onto the film surface (Microchemicals AZ P4620), then exposing the resist through a photomask, developing the resist, ion milling for ~ 45 min (milling depth of ~ 350 nm), and stripping of the residual resist. The films were characterized again after patterning by AFM and optical microscopy.

Platinum microelectrodes were fabricated on top of an SNB pellet via photolithography and d.c. magnetron sputtering. In the photolithography step, the pellet was rinsed and treated for 3 min with a 150 W oxygen plasma, then exposed

for 5 min to air saturated with the adhesion promoter hexamethyldisilazane (MicroChemicals), dehydration baked at 120°C for 5 min, spin-coated with photoresist (Shipley 1813, 2500 rpm, 30 s), baked at 115°C for 150 s, exposed for 60 s to UV radiation (275 W, 385 nm) through a photomask, developed by immersion in MF-319 (Microposit) for 50 s, rinsed in deionized water, and treated for an additional 3 min with an oxygen plasma. The sputtering system (AJA International, Pt target, 99.99% purity) had a base pressure of 10^{-6} torr, 3 mtorr Ar working pressure, and a d.c. plasma power of 150 W. Deposited metal layers were ~600 nm thick. The microelectrode diameters were varied from 500 μm to 30 μm .

3.3.3 Impedance characterization

Each substrate was adhered to a $\sim 2 \text{ cm}^2 \times 0.6 \text{ mm}$ alumina sheet (McMaster) using silver paste (DAD-87, Shanghai Research Institute), which also served as a counter electrode. The paste was fired in a quartz tube under stagnant air at 600°C - 700°C for 1 h. A given substrate was then installed in the scanning impedance probe, and impedance spectra were acquired using zero bias, an a.c. perturbation voltage of 10 mV - 30 mV, and a frequency range of 10 kHz - 16 mHz. For the LSC measurements, a Paliney7 probe tip (American Probe & Technologies, 20 μm tip radius) was used. For SNB a $\text{Pt}_{0.7}\text{Ir}_{0.3}$ tip (Moser, 10 μm tip radius) was used. The latter tip sometimes created visible scratches in the microelectrodes; when that was observed, no further measurements were performed on the damaged microelectrode. The impedance analyzer calibration was verified before each experiment using Faraday-cage-shielded test circuits comprised of precision megaohm resistors and nanofarad capacitors. After fitting the resulting spectra, the resistance and capacitance values of the circuit components were reproduced with < 3% error.

The film temperature ranges used were 520°C - 615°C (for LSC) and 575°C - 650°C (for SNB). The oxygen partial pressure in the chamber was typically varied over the range 10^{-3} atm - 1 atm by flowing bottled dry oxygen or oxygen-nitrogen mixtures. Often a small number of representative microelectrodes were repeatedly measured at a given condition over a few hours to verify stability, after which many other microelectrodes were measured once. For the primary LSC sample reported below, a total of 680 impedance spectra were acquired over 125 h of measurement time; for SNB, 1,371 impedance spectra were acquired over 240 h.

The acquired impedance spectra were fit to various impedance expressions (derived in Section 3.3) by complex nonlinear least squares using a Matlab routine implemented in collaboration with Chris Kucharczyk. The fit residual of each complex impedance datum was weighted by the complex modulus of that datum, which serves as a proxy for the unknown variance of the datum. A few spectra had unreasonably large confidence intervals for the resulting fit parameters; these spectra were excluded.

After impedance testing, the samples were coated with ~ 10 nm carbon (Cressington 108) and characterized with a scanning electron microscope (SEM, Zeiss 1550 VP) using either in-lens or below-lens secondary electron detectors, as well as an energy dispersive spectrometer (EDS, Oxford X-Max SDD).

3.4 Electrochemical models

Different material systems can have different catalytic pathways for oxygen reduction, and in that case, the appropriate electrochemical models can also be different. Some pathways relevant to this work are shown in Figure 3.1 as pathways (a) through (d), and some relevant equivalent circuits are shown in Figure 3.2 as circuits (a) through (d).

Circuit (a) corresponds to pathway (a) and has been previously derived in detail.²⁶

Circuit (b) was used for LSM in previous chapter, and is shown here for comparison purposes only.

Circuit (c) is used for LSC in this work, and is obtained from circuit (b) by adding the assumption that ion conduction in the mixed conductor is also fast ($R_{ion} \approx 0$). The circuit then simplifies, since the three capacitors can be summed in parallel, such that $C_{total} = C_{chem} + C_{ion}^s + C_{eon}^p$.

Circuit (d) is used for SNB in this work, and is an empirical circuit that corresponds to pathways (c) or (d),

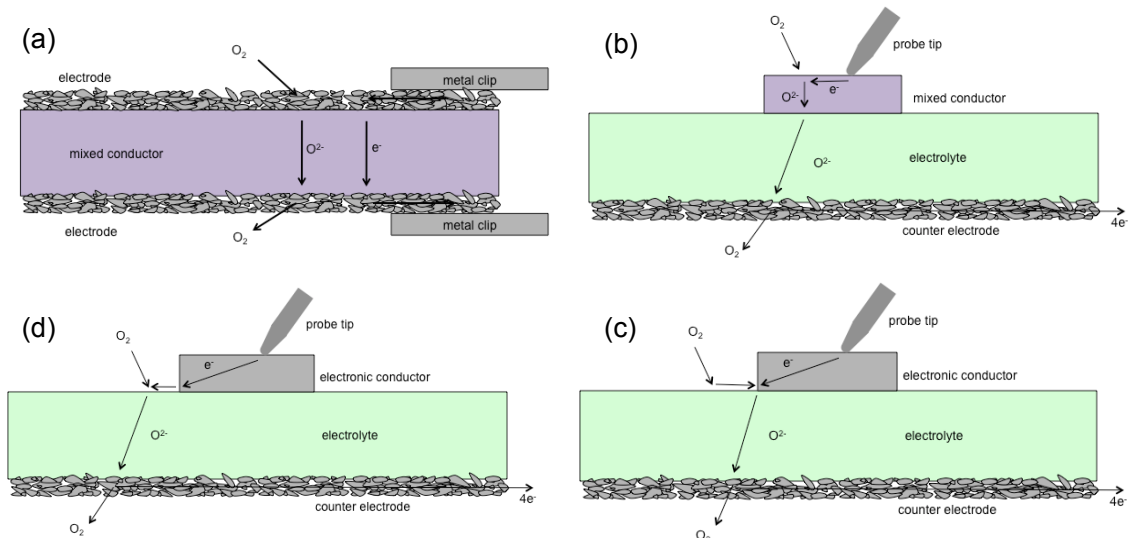


Figure 3.1. Possible electrochemical pathways. (a) mixed conducting pellet, (b) mixed conducting microelectrode, (c) electronically conducting microelectrode with surface diffusion on electrolyte, and (d) electronically conducting microelectrode with electron migration through electrolyte.

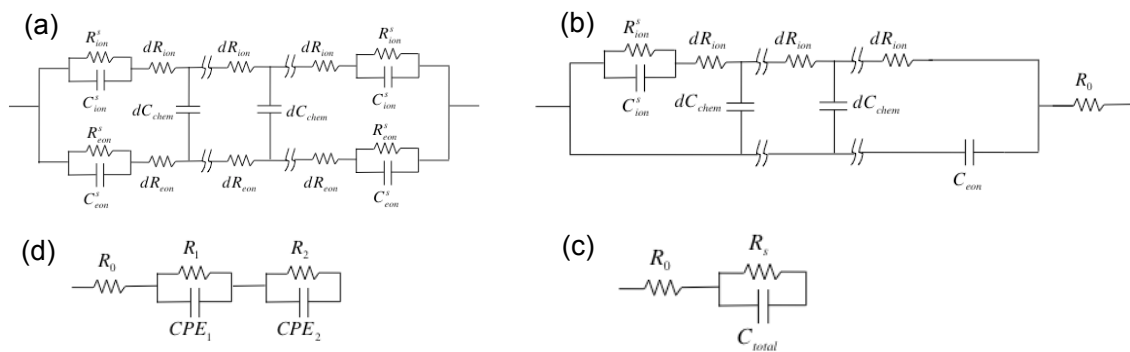


Figure 3.2. Equivalent circuits for (a) mixed conducting pellet, (b) $La_{0.5}Sr_{0.5}CoO_3$ microelectrode, (c) $(La_{0.8}Sr_{0.2})_{0.95}MnO_3$ microelectrode, and (d) Pt microelectrode on $Sr_{0.06}Nb_{0.06}Bi_{1.87}O_3$.

3.5 $\text{La}_{0.5}\text{Sr}_{0.5}\text{CoO}_3$ results

3.5.1 Structural characterization

All LSC films in this work were found by XRD to be (110) oriented as grown, and no additional reflections were visible. A typical set of XRD patterns taken prior to patterning is shown in Figure 3.3. AFM micrographs taken prior to patterning indicated the films have a columnar grain structure with ~ 50 nm - 100 nm column diameters, as shown in Figure 3.4, with a typical r.m.s. surface roughness of 3 nm. After patterning (*i.e.*, photolithography and ion milling), typical samples looked as shown in the optical photos in Figure 3.5.

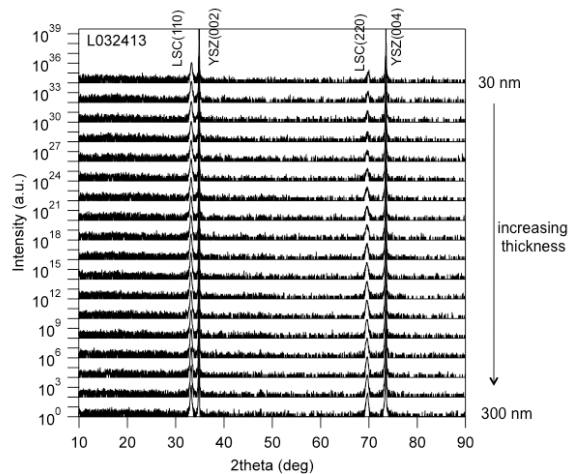


Figure 3.3. XRD patterns acquired from a single YSZ substrate containing $\text{La}_{0.5}\text{Sr}_{0.5}\text{CoO}_3$ films with thicknesses in the range 30 nm - 300 nm. Courtesy of Shingo Maruyama.

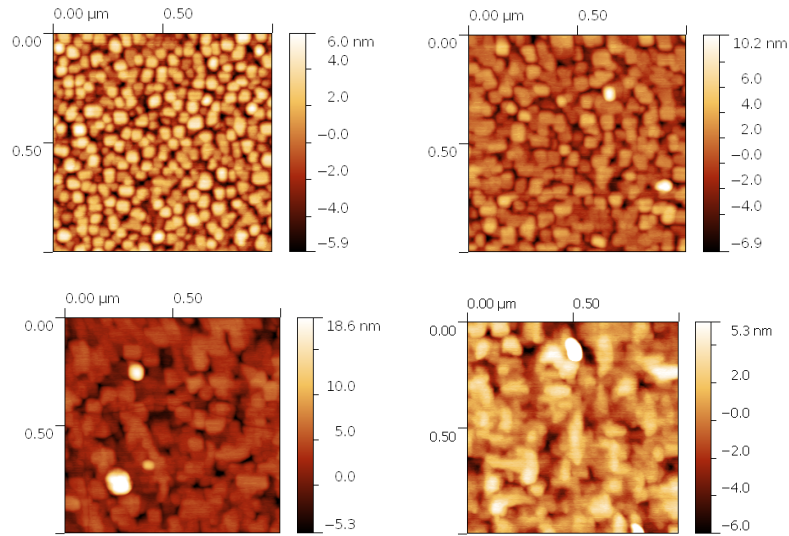


Figure 3.4 $\text{La}_{0.5}\text{Sr}_{0.5}\text{CoO}_{3-\delta}$ films as grown by PLD with thicknesses of 30 nm (upper left), 84 nm (upper right), lower left (192 nm), and lower right (300 nm). Courtesy of Shingo Maruyama.

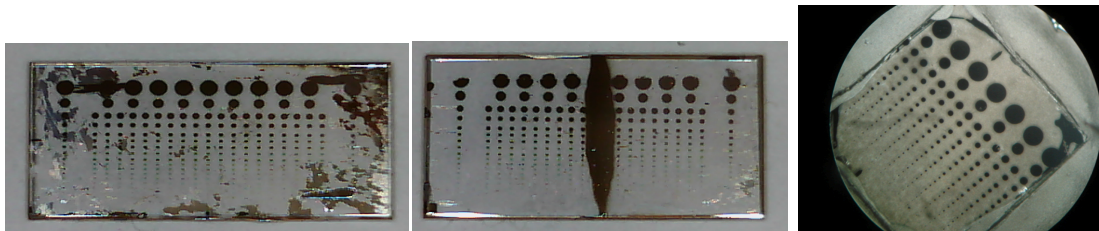


Figure 3.5. Optical photos of typical LSC samples. From left to right: various thicknesses ranging from 300 nm - 30 nm; a sample containing exactly two film thicknesses, 300 nm and 30 nm; and uniform 200 nm thickness. Some dark smudges are visible; this is residual silver paste on the backside of the transparent substrate (used to affix the substrate during deposition).

Optical microscopy, AFM, and SEM indicated that the microelectrode dimensions were precise and repeatable. The microelectrode diameters were consistently a few microns smaller than nominal, and the edges exhibited a few microns of waviness, resulting in $\sim 5\%$ variation in area between nominally identically microelectrodes. The film thickness was uniform within a few nanometers across a given microelectrode. A height "blip" was typically observed by AFM at the edges of a given microelectrode, suggesting that a small amount of material debris collected at the dot edge during the milling process. These findings are illustrated in Figure 3.6.

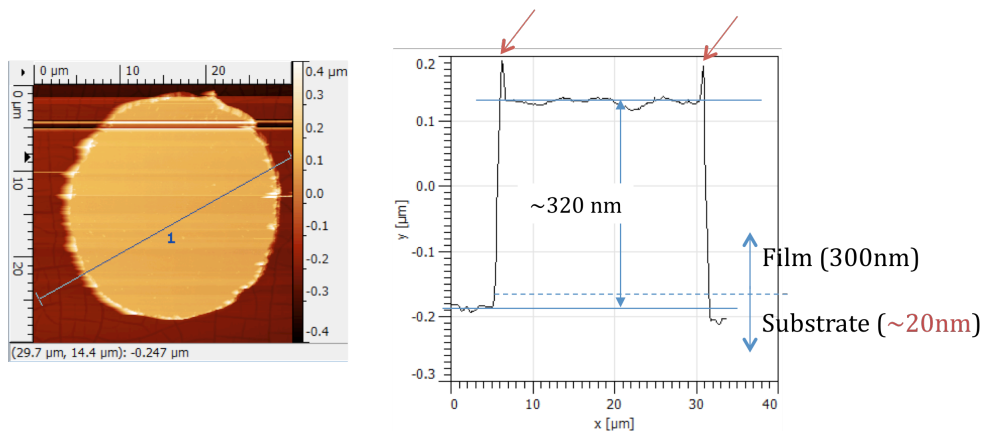


Figure 3.6. AFM profile scan of an LSC microelectrode with 300 nm nominal thickness, 30 μm nominal diameter. Courtesy of Shingo Maruyama.

Some previous reports have used wet etching with hydrochloric acid to pattern oxide films, and these reports find that the acid undercuts the photoresist by ~ 20 μm. By contrast, the dry etching (ion milling) technique used here exhibits only 2

um - 3 um undercutting as illustrated by SEM and AFM in Figure 3.7, resulting in sharper edges and improved thickness uniformity.

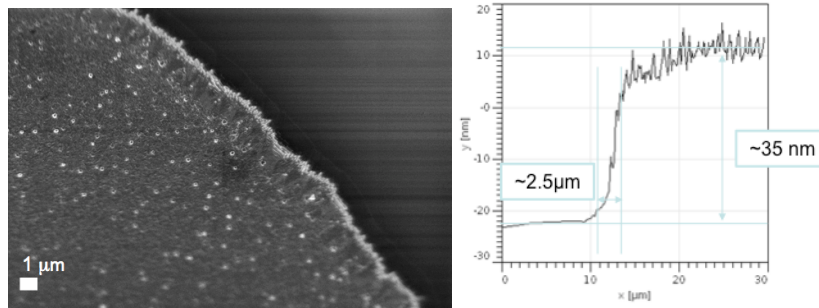


Figure 3.7. Edge quality of LSC films after patterning by ion milling. Left: SEM micrograph, taken from a sample without carbon coating. Right: AFM profile scan, courtesy of Shingo Maruyama.

Two potential problems were revealed by high magnification SEM imaging. First, most of the patterned films had numerous nanoscale cracks, as seen in Figure 3.8. Such cracks were also seen by AFM prior to patterning. These cracks were undoubtedly caused by the fast 100°C/min cooling rate that was used after deposition. Such a fast cooling rate should be avoided when processing films of materials like LSC that exhibit high thermochemical expansivity. Second, as discussed in Chapter 1, SEM images acquired from these films after impedance testing revealed that numerous silver particles had accumulated on the film surfaces during testing. See Figure 3.9. The implications of these two potential problems are addressed below in the interpretation of the impedance results.

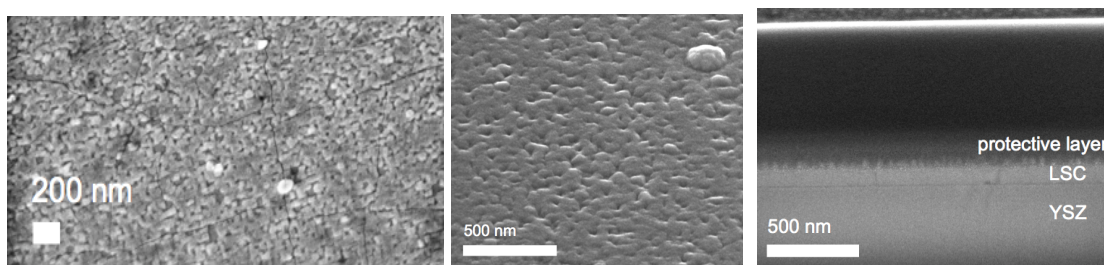


Figure 3.8. Surface and cross-section SEM micrographs of a representative $\text{La}_{0.5}\text{Sr}_{0.5}\text{CoO}_{3-\delta}$ film with 100 nm thickness that did not undergo impedance testing. Sample is tilted 52° in the center and right images.

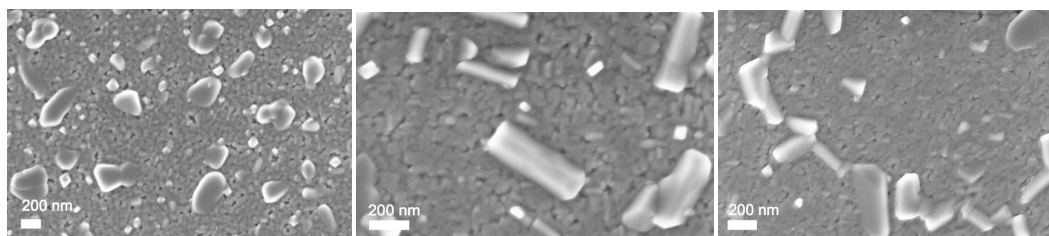


Figure 3.9 SEM micrographs acquired after impedance testing of $\text{La}_{0.5}\text{Sr}_{0.5}\text{CoO}_{3-\delta}$ films with thicknesses of 30 nm (left), 165 nm (middle), and 300 nm (right).

3.5.2 Impedance data

Representative electrochemical impedance spectra acquired from the LSC films are shown in Figure 3.10. Each spectrum consists of a single undepressed arc that coincides with the real axis at high frequencies. The characteristic frequency of the arc (*i.e.*, the frequency at which the imaginary component is most negative) decreased with decreasing temperature, decreasing p_{O_2} , and increasing thickness. Each spectrum was fit to the equivalent circuit described in Section 3.3.

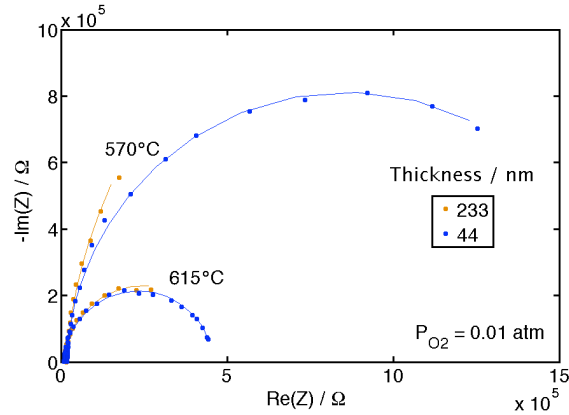


Figure 3.10. Typical impedance spectra acquired from thin film $\text{La}_{0.5}\text{Sr}_{0.5}\text{CoO}_{3-\delta}$ microelectrodes over the frequency range 10 kHz - 20 mHz. Points are the raw data; Curves are fits to the equivalent circuit shown in Section 3.4. The data shown here were acquired from microelectrodes with 200 μm diameter at the indicated temperatures and oxygen partial pressure.

A total of 680 impedance spectra were acquired in this experiment over the course of 5 days. Each spectrum yielded three fit parameters: an offset resistance R_0 , a total capacitance C_{chem} , and a surface resistance R_s . These fit parameters are plotted in Figure 3.11, Figure 3.12, and Figure 3.13.

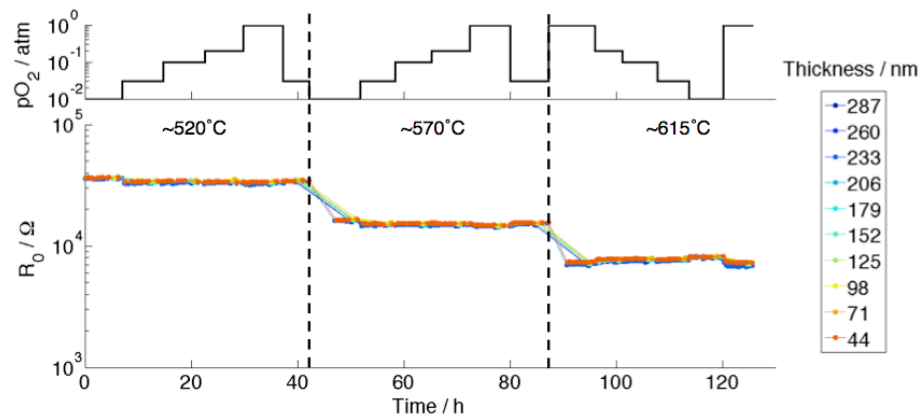


Figure 3.11. Offset resistance R_0 extracted from impedance spectra measured from $\text{La}_{0.5}\text{Sr}_{0.5}\text{CoO}_{3-\delta}$ films of various thicknesses at the indicated temperatures and oxygen partial pressures.

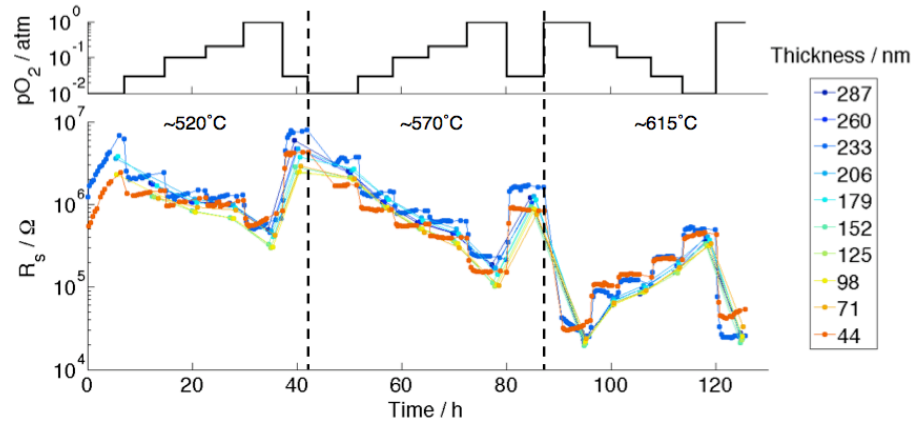


Figure 3.12. Surface resistance R_s extracted from impedance spectra measured from $\text{La}_{0.5}\text{Sr}_{0.5}\text{CoO}_{3-\delta}$ films of various thicknesses at the indicated temperatures and oxygen partial pressures.

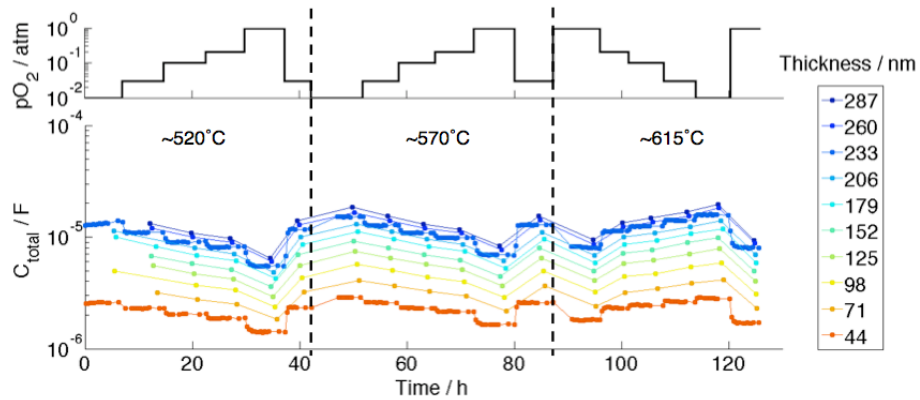


Figure 3.13. Total capacitance C_{chem} extracted from impedance spectra measured from $\text{La}_{0.5}\text{Sr}_{0.5}\text{CoO}_{3-\delta}$ films of various thicknesses at the indicated temperatures and oxygen partial pressures.

The surface resistances R_s were initially unstable. Over the first 40 hours of measurement at $\sim 520^\circ\text{C}$, they increased by more than an order of magnitude. The degradation rate appeared to be independent of film thickness, and it slowed over time, such that the resistances approximately stabilized after several tens of hours. Data from a second sample (see Figure 3.14) confirmed that this initial degradation is approximately linear with time for the first few days, independent of thickness, and independent of how often the microelectrode was probed, indicating that the repeated probing is not causing the degradation. Overall, the surface resistance of the films from both samples degraded by roughly a factor of 50 before stabilizing.

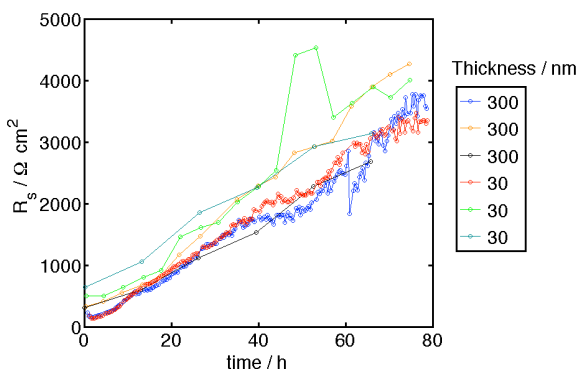


Figure 3.14. Surface resistance measured on a second sample of LSC microelectrodes with thicknesses of 30 nm and 300 nm, probed at $\sim 520^\circ\text{C}$ in 0.01 atm O_2 .

Returning to the primary sample, at first glance the total capacitances C_{chem} appear stable. Close inspection reveals that the total capacitances of the 233 nm and 300 nm films appear to have increased by 10-20% over the first 40 hours, while the

total capacitances of the 30 nm and 44 nm films remained stable. The cause of this difference in stability is unknown.

The offset resistances R_0 were stable, dependent on temperature, and only very weakly dependent on thickness and oxygen partial pressure. These findings are consistent with the attribution of the offset resistance primarily to ion conduction through the YSZ electrolyte.

The thickness dependence of these three fit parameters at 615°C is shown in Figure 3.15. The surface resistance R_s shows no thickness dependence to first order. This finding indicates that the sidewalls of any pores or nanoscale cracks in the films contribute negligibly to the surface activity. The offset resistance R_0 depends slightly on oxygen partial pressure and increases very slightly as thickness decreases, suggesting that sheet resistance (electronic conduction) through the LSC makes a measurable but very small contribution to the offset resistance. The total capacitance C_{total} is proportional to thickness, and by extrapolating to zero thickness, the interfacial capacitance can be estimated as being small, less than 0.01 F/cm².

Two second-order effects are noteworthy. First, the fit residuals for the surface resistance and chemical capacitance share a systematic trend with thickness. This trend is consistent with steady-state temperature variations of an estimated $\pm 8^\circ\text{C}$ across the nominally isothermal stage (estimated from the Arrhenius slopes in

Figure 3.17). Second, the extrapolated total capacitance fits do not coincide at zero thickness. One possible explanation is that the surface divots in the LSC film decrease the volume of the outermost nanometers of the film and effectively introduce error in the film thickness.

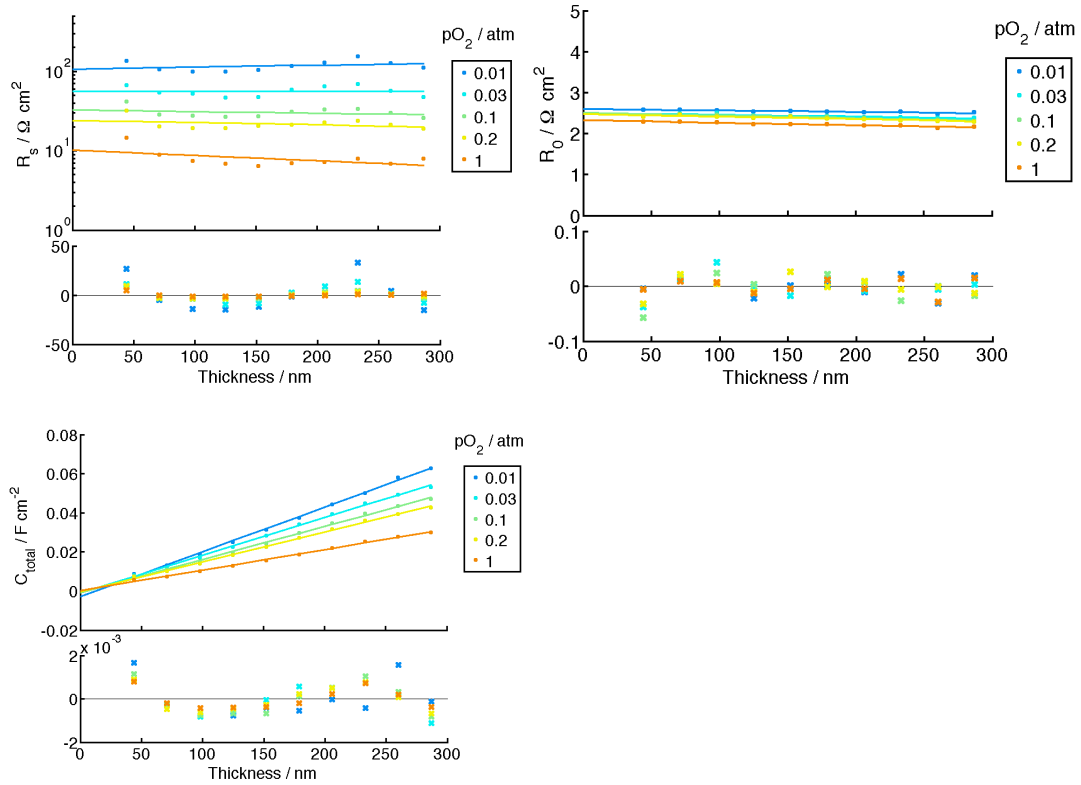


Figure 3.15. Area-normalized surface resistance R_s (upper left), total capacitance C_{total} (lower left), and offset resistance R_0 (upper right) of (200 μm diameter) $\text{La}_{0.5}\text{Sr}_{0.5}\text{CoO}_{3-\delta}$ microelectrodes of various thicknesses at 615°C. Lines are linear fits to the raw data points. The fit residuals are plotted as a subplot below the main plot.

The slope of total capacitance with thickness is equivalent to the volume-normalized chemical capacitance. These values are plotted in Figure 3.16 alongside comparable values reported in the literature for bulk samples of the same LSC composition. The chemical capacitance appears to be significantly lower in the films than in bulk samples. This difference may stem from the fact that grain boundaries occupy a high volume fraction in the films relative to bulk samples. Segregation of Sr to the film surface (as has been observed in LSM⁵⁸) would also be expected to lower the chemical capacitance of the films.

In Figure 3.17, the surface resistance of the films is plotted versus oxygen partial pressure and versus temperature in Arrhenius form. Strikingly, the activation energy between 570°C and 615°C is 2.5 eV, nearly identical to what was measured previously on equilibrated films of $\text{Ba}_{0.5}\text{Sr}_{0.5}\text{Co}_{0.8}\text{Fe}_{0.2}\text{O}_{3-\delta}$ (BSCF) films grown on SDC(100) / YSZ(100) (Francisco Barroso, Haile group unpublished), and the absolute magnitudes of the surface activities are also quite similar.

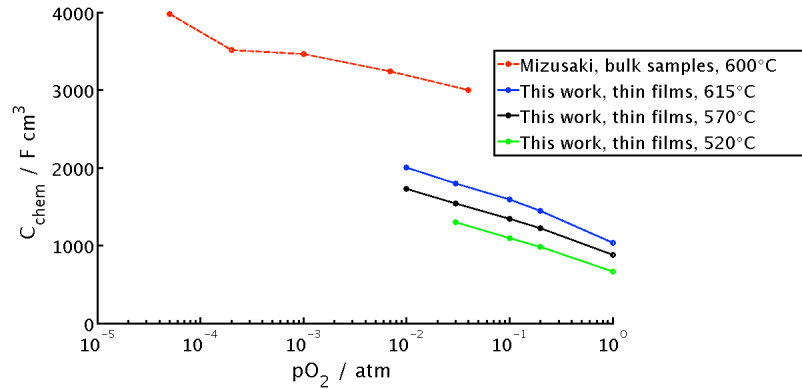


Figure 3.16. Comparison of the volume-normalized chemical capacitance of thin films (this work) and bulk samples⁵⁹ of $\text{La}_{0.5}\text{Sr}_{0.5}\text{CoO}_{3-\delta}$. Lines connecting the data points are guides for the eye.

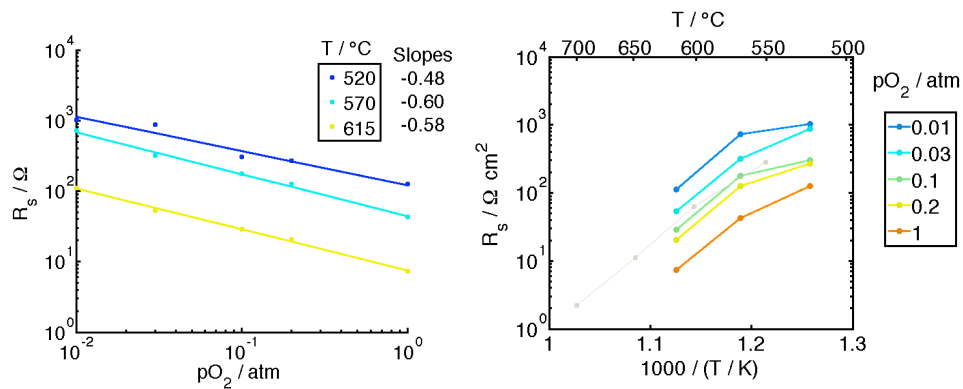


Figure 3.17. Surface resistance R_s of $\text{La}_{0.5}\text{Sr}_{0.5}\text{CoO}_{3-\delta}$ films after dwelling several hours at each given temperature and oxygen partial pressure, plotted versus oxygen partial pressure (left) and in Arrhenius form (right). Points were calculated by averaging the values measured from several film thicknesses. For comparison, data at 0.2 atm for $\text{Ba}_{0.5}\text{Sr}_{0.5}\text{Co}_{0.8}\text{Fe}_{0.2}\text{O}_{3-\delta}$ films (grown on SDC (100) on YSZ (100)) are shown at right in light gray (Francisco Barroso, Haile group unpublished).

3.6 $\text{Sr}_{0.06}\text{Nb}_{0.06}\text{Bi}_{1.87}\text{O}_3$ results

3.6.1 Structural characterization

Optical and SEM images of platinum microelectrodes on an SNB substrate are shown in Figure 3.18. The microelectrodes are ~ 600 nm thick. As a result of the photolithography liftoff process, the outermost ~ 2 microns of each microelectrode are slightly thicker than the rest of the microelectrode. The diameters were measured by optical microscopy and found to be close to the nominal values.

After testing, the surface of the SNB was observed to have become rough and faceted, and bismuth-rich particles were accumulated atop the grain boundaries of the SNB, as shown in Figure 3.19. These findings indicate that SNB is not fully stable under the testing conditions. The platinum microelectrodes exhibited some coarsening as a result of the SNB surface faceting, and some Ag was detected on the platinum. A few microelectrodes that were probed, including the one shown in Figure 3.19, were observed to have blisters. These are attributed to oxygen evolution at the platinum-SNB interface driven by repeated impedance measurements.

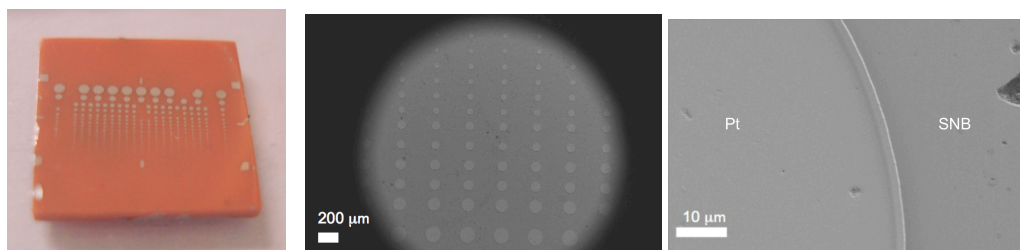


Figure 3.18. Optical (left) and SEM (right) images of platinum microelectrodes on an SNB substrate, before impedance testing.

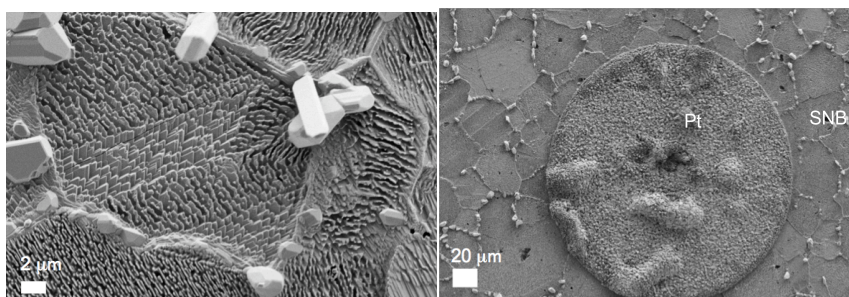


Figure 3.19. SEM images of the SNB surface (left) and a platinum microelectrode (right) after several days of impedance testing at 575°C - 650°C under $pO_2 = 10^{-3} - 1$ atm.

3.6.2 Impedance spectra

Typical impedance spectra acquired from the platinum microelectrodes are shown in Figure 3.20. The spectra are well-fit by the empirical equivalent circuit described in Section 3.4.

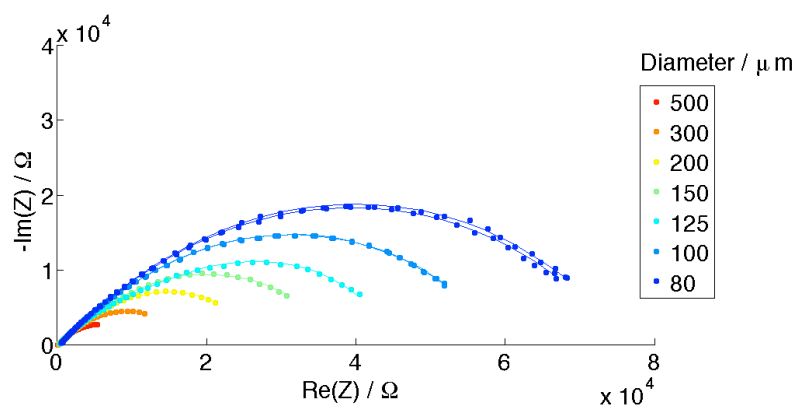


Figure 3.20. Impedance spectra acquired from platinum microelectrodes of various diameters on SNB at $\sim 625^\circ\text{C}$ in 0.2 atm O_2 . Points are raw data; lines are fits to the empirical equivalent circuit described in Section 3.4.

The overall arc width $R_{dc} - R_0$ and the offset resistance R_0 are plotted in Figure 3.21. $R_{dc} - R_0$ (*i.e.*, the overall arc width, $Z(0 \text{ Hz}) - Z(\infty \text{ Hz})$) is equivalent to the electrochemical reaction resistance R_s under the assumption that in SNB the transference number for ions $t_{ion} \geq 0.999$. This assumption is consistent with a previous report on doped bismuth oxide [9] but requires further verification.

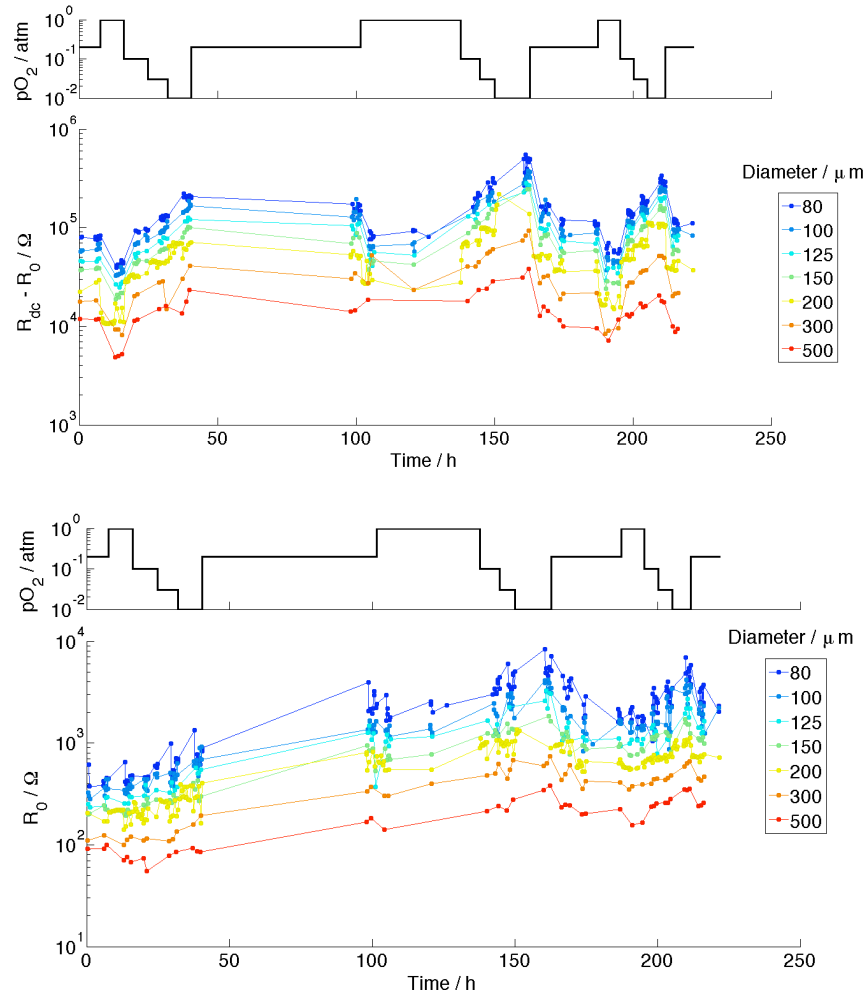


Figure 3.21. Overall arc width $R_{dc}-R_0$ (top) and offset resistance R_0 (bottom) measured over time at the indicated temperatures and oxygen partial pressures from platinum microelectrodes of various diameters on SNB. Points were extracted from the impedance spectra; lines connect the points as guides for the eye.

The diameter dependence of the electrochemical reaction resistance is plotted in Figure 3.22 at left. The slope of close to -1 in the double-logarithmic plot indicates that the electrochemical activity scales with the microelectrode perimeter. This important finding is distinct from the LSC and LSM films discussed above; it indicates that the electrochemical reaction proceeds via a triple phase boundary path. It also rules out dissociative adsorption on the platinum microelectrodes as a rate-limiting step, since that process would be expected to scale with surface area. The same data is plotted versus oxygen partial pressure in Figure 3.22 at right. The slopes here indicate that the electrochemical activity scales with $pO_2^{-0.3}$. This value is close to the -0.25 that would be expected if electron migration at the SNB surface were the rate-limiting step.

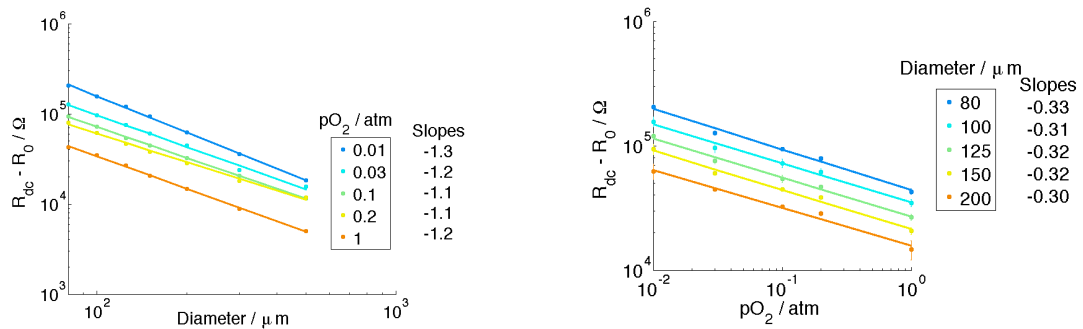


Figure 3.22. Overall arc width $R_{dc} - R_0$ measured from platinum microdots on SNB at $\sim 625^\circ\text{C}$ as a function of diameter (left) and oxygen partial pressure (right). Points were extracted from the impedance spectra; lines are linear fits on a double-logarithmic scale.

Figure 3.20, Figure 3.21, and Figure 3.22 all assume that the microelectrodes are at the same indicated temperature. In practice, tip cooling lowers the average surface temperature of smaller-diameter microelectrodes to a greater extent. As discussed in Chapter 1, a knowledge of the cooling-induced thermovoltage along with the SNB Seebeck coefficient enables the extent of the temperature drop due to tip cooling to be estimated. Using this temperature correction, an Arrhenius plot of the electrochemical reaction resistance is shown in Figure 3.23. Activation enthalpies are calculated from the slope of linear fits to these data, and are shown next to the legend. The measured activation energy of 0.9 eV - 1.0 eV agrees well with the activation energy of 1.1 eV measured by Takahashi for the electronic hole conductivity of a similar doped bismuth oxide composition. On the other hand, the activation energies measured for surface catalysis on platinum are different, 1.6 eV - 2.3 eV. Thus the temperature behavior is also consistent with electron migration through the bismuth oxide being the rate-limiting step.

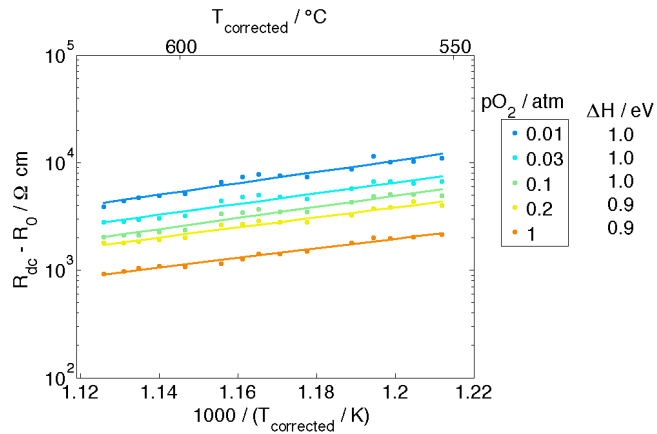


Figure 3.23. Arrhenius plot of the electrochemical reaction resistance. The film temperatures were corrected approximately for tip cooling. Points are extracted from the impedance spectra; lines are linear fits to the points. The activation enthalpy extracted from the line slopes is shown beside the legend.

3.7 Conclusions

For $La_{0.5}Sr_{0.5}CoO_3$ films on (100) YSZ, the impedance spectra in the measured temperature range 520°C - 615°C consisted of a single semi-circle. The measured capacitance and resistance values were unstable for the first ~ 50 h at 520°C, and subsequently stabilized at higher temperatures. This stability suggests that silver particles (which continued to accumulate slowly on the sample surfaces during the high temperature measurements) do not significantly enhance or degrade the film activity. The thickness independence of the arc resistance R_s confirmed that bulk transport makes a negligible contribution, and suggested (since the density of surface grain boundaries exhibited some thickness dependence) that surface grain boundary sites are not significantly more active than other surface sites. The arc

resistance was attributed entirely to the surface process, under the assumption that the LSC-YSZ interface was reversible for ion transport. The chemical capacitance of the LSC films scaled linearly with thickness, was stable over time, and was lower than the chemical capacitance of bulk $\text{La}_{0.5}\text{Sr}_{0.5}\text{CoO}_{3-\delta}$ samples reported in the literature. The strikingly similar activity and activation energy between the $\text{La}_{0.5}\text{Sr}_{0.5}\text{CoO}_3$ films measured in this work and $\text{Ba}_{0.5}\text{Sr}_{0.5}\text{Co}_{0.8}\text{Fe}_{0.2}\text{O}_{3-\delta}$ macroscopic electrodes (1 cm^2) measured previously suggests that these two film compositions are rate-limited by the same process.

For platinum films on a doped bismuth oxide substrate, specifically $\text{Sr}_{0.06}\text{Nb}_{0.06}\text{Bi}_{1.87}\text{O}_3$, fitting the equivalent circuit to an empirical model enables a total resistance to be extracted. Under the assumption that the substrate has an ionic transference number > 0.999 , this resistance could be equated with the electrochemical reaction resistance. The diameter, $p\text{O}_2$, and temperature trends suggest that catalysis proceeds by a pathway involving dissociative adsorption onto the bismuth oxide, followed by diffusion towards the triple phase boundary and/or surface incorporation. The activation energy of the total resistance was quite similar to the previously reported activation energy for electronic hole conduction in yttria-doped bismuth oxide, suggesting that electron migration is rate-limiting. Overall, the high activity near the metal-doped- Bi_2O_3 interface suggests that using such materials in a cathode with a favorable microstructure should be competitive with other state of the art cathodes. These measurements should be repeated in an electron-blocking configuration (*e.g.*, doped bismuth

oxide films on a YSZ substrate) to confirm that electronic leakage through the substrate is not significant.

CHAPTER 4 MORE DETAIL ABOUT THE SCANNING IMPEDANCE PROBE

4.1 Summary

This chapter is intended primarily for future users of the high throughput approach described in the previous chapters; other readers may wish to skip to Chapter 5. Section 4.2 describes the parallel characterization approach in more detail. Section 4.3 describes the pulsed laser deposition system used to fabricate graded samples in this work. Section 4.4 gives specifications for the scanning impedance probe. Section 4.5 describes some obstacles to obtaining high quality data and how to overcome them.

4.2 Parallel characterization

A schematic of the typical test configuration in the scanning impedance probe is shown in Figure 4.1. Many features are similar to existing instruments for probing microelectrodes.⁹ The typical sample consists of a dense solid $Y_xZr_{1-x}O_{2-x/2}$ (YSZ) electrolyte with an array of thin film microelectrodes patterned on the top face. A porous counter electrode is applied over the entire bottom face. The sample is placed on a stage heater with a thin piece of ceramic insulation to provide electrical insulation between the sample and the stage. A metal wire is used to connect the counter electrode to the negative terminal of an external impedance analyzer. The chamber is sealed, and the sample is heated to high temperature while the desired test gas flows continuously through the chamber. A metal probe

tip is touched to an individual microelectrode in order to make an electrical connection to the positive terminal of the impedance analyzer, and an impedance spectrum (or d.c. voltammogram) can then be acquired. The probe tip is moved or the conditions are adjusted, another impedance spectrum is acquired, and so on until the study is completed. An external optical microscope peers through a quartz viewport in the chamber ceiling, enabling the user to view the position of the metal probe tip relative to the micropatterned features on the sample.

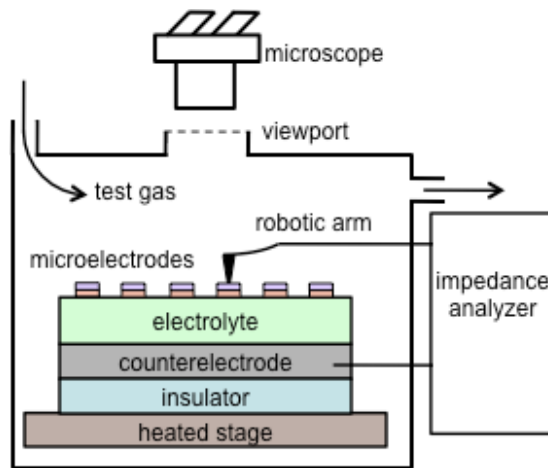


Figure 4.1. Schematic of the test configuration in the scanning impedance probe.

The most significant new feature of the scanning impedance probe is the "scanning" capability: the position of the alumina rod holding the metal probe tip is controlled by three orthogonal lead screws controlled by stepper motors. Thus the metal probe tip can be touched to a microelectrode simply by entering the appropriate (X,Y,Z) coordinates in the control software developed by the author. By extension, hundreds of microelectrodes can be contacted and measured in

sequence simply by listing their coordinates. The control software also allows for automated control of stage temperature, gas flows, and other settings such as wait times between steps, d.c. bias voltage, a.c. perturbation voltage, and so on. Since a single impedance spectrum typically takes 1 min - 15 min to acquire, depending on the chosen frequency range, the scanning impedance probe can measure between 100 and 1500 spectra per day. So for instance, at 5 min per spectrum, a study of 100 microelectrode compositions at five gas pressures and four temperatures can be completed autonomously in about one week.

Automation also facilitates precise vertical positioning of the probe; too high and the tip does not touch the sample at all; too low and the tip is jammed into the sample, which can introduce error in the tip position and damage the tip or the sample. The scanning impedance probe automatically detects the contact by repeatedly measuring the impedance at a single frequency as the tip is slowly lowered.

4.3 Parallel fabrication

Two example layouts for the microelectrode arrays are shown schematically in Figure 4.2. The outer dimensions of these layouts correspond to typical commercially-available substrate sizes of 5 mm x 10 mm (left layout) and 10 mm x 10 mm (right layout). Each circle represents a single microelectrode, and the area between the circles represents exposed substrate. The left layout includes a diameter gradient, while the right layout has a fixed diameter (125 μm). In the

horizontal direction of each layout and in the vertical direction of the right layout, another property besides diameter can be graded.

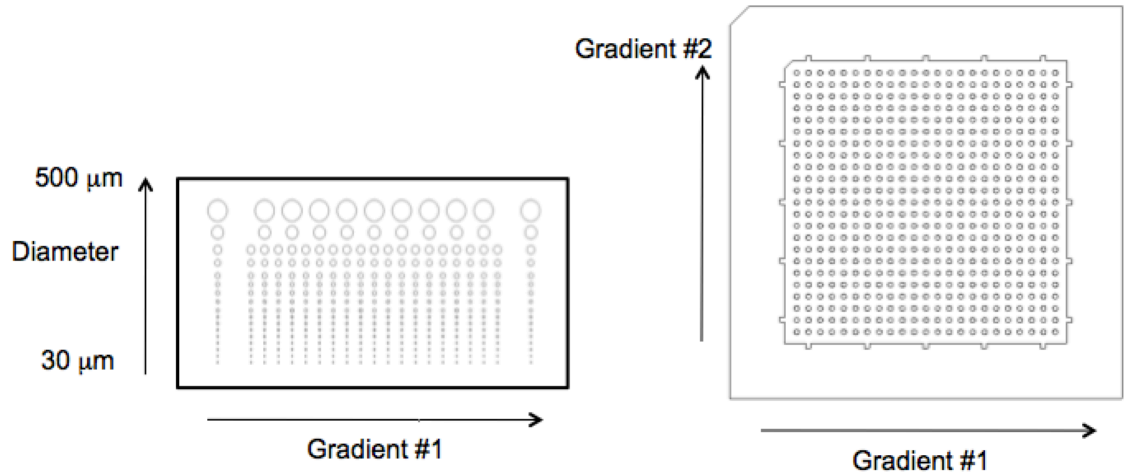


Figure 4.2. Example layouts of microelectrodes on a sample. Left: $17 \times 21 = 357$ microelectrodes (including 11 different diameters) on a 5 mm x 10 mm substrate. Right: $23 \times 23 = 529$ microelectrodes on a 10 mm x 10 mm substrate.

Previous microelectrode studies have not reported gradients of properties other than microelectrode diameter/area. Yet many properties can conceivably be graded, as illustrated in Figure 4.3.

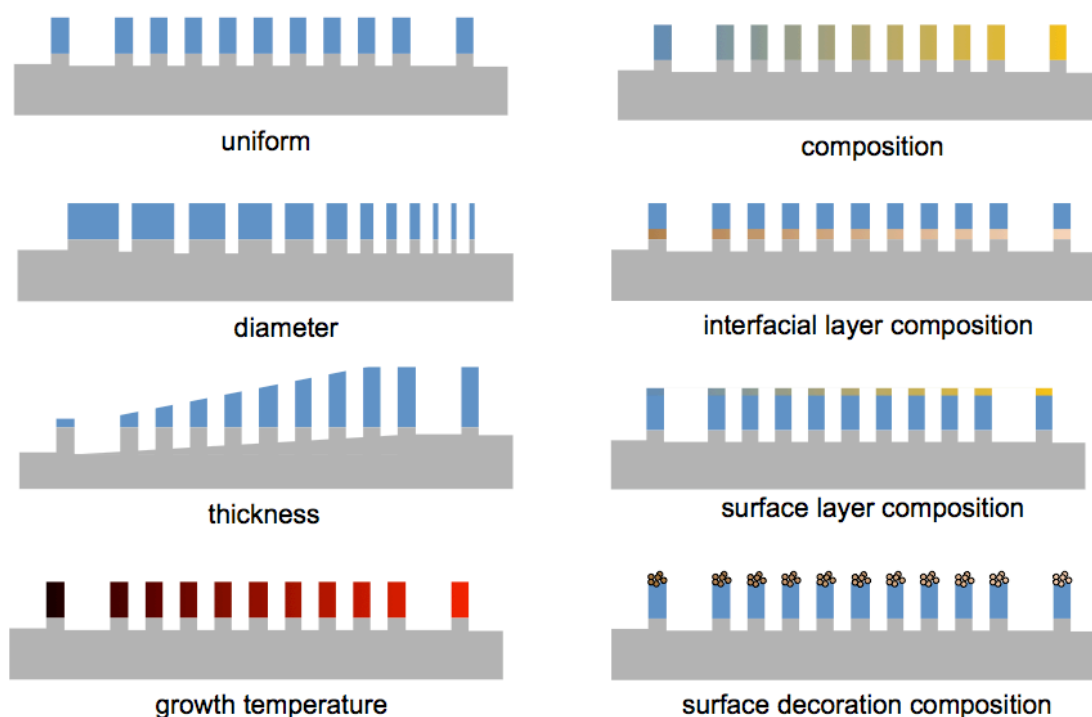


Figure 4.3. Examples of properties that can be systematically varied along the rows and/or columns of a microelectrode array.

This approach of combining graded samples with automated impedance measurement can potentially give insight into a variety of important questions. For example, in the material system $\text{La}_{0.5}\text{Sr}_{0.5}\text{Co}_{1-y}\text{Fe}_y\text{O}_{3-\delta}$ what level of iron doping results in the highest activity towards oxygen electro-reduction? Do all levels of iron doping provide equal long-term stability? Does film thickness matter, or is there facile ion diffusion through the film? Can strain effects be seen by varying the composition of an interfacial layer? Can the activity be influenced by decorating the catalyst surfaces with trace amounts of another substance? And of course, when interesting trends in activity are identified, the graded samples can be probed by numerous other techniques besides impedance spectroscopy, so that

correlations can be investigated between electrochemical activity and properties like film orientation, grain boundary density, surface electronic structure, and so on.

Fabrication of the arrays shown in Figure 4.3 is possible by many routes. In the work described in the previous chapters, the gradient samples were prepared by Shingo Maruyama (a member of the Professor Ichiro Takeuchi's group at the University of Maryland) using pulsed laser deposition in combination with movable shutters and appropriate stages. This method is described elsewhere⁶⁰ and briefly summarized here. Two targets with the end member compositions A and B are used. By frequently altering which target is ablated while drawing a shutter back and forth across the sample, a library with the composition spread A_xB_{1-x} is obtained. At first glance it may appear that the resulting film would have numerous interwoven layers, however the deposition is typically done at high enough temperature that the diffusion length is larger than the layer thickness (~ 1 monolayer) but far smaller than the sample length (1 cm). Thus in terms of composition, the growth achieves out-of-plane homogeneity while retaining in-plane heterogeneity. Alternatively, by using one target and slowly drawing the shutter across the sample a single time, a thickness gradient is achieved in a single composition. Another option is the use of a stage with asymmetric geometry, as described in the last chapter, that can achieve a lateral temperature gradient of $200^\circ\text{C} - 300^\circ\text{C}$ between the ends of a 1 cm substrate. An exciting possibility in development is to fabricate not just binary libraries but ternary or quaternary

libraries. For example, with appropriate shutter motions it should be possible to obtain quaternary library shown in Figure 4.4. Similar libraries have been demonstrated for luminescent and magnetic materials.⁶⁰ In all cases, after the growth, photolithography and ion milling are used to etch away the undesired portions of the film, leaving behind the microelectrode pattern as shown in Figure 4.2.

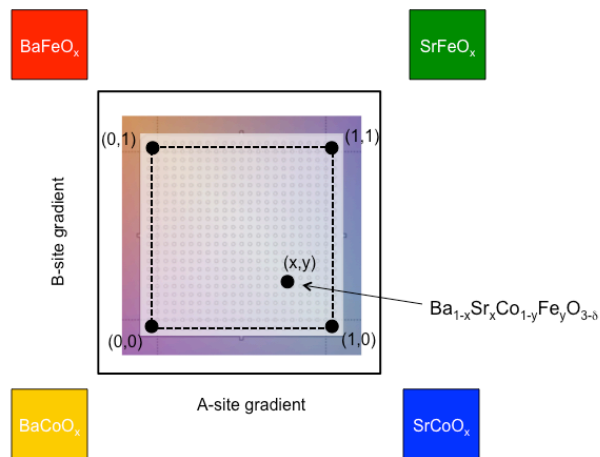


Figure 4.4. Schematic of a quaternary library that could be made from four binary targets ($BaFeO_x$, $SrFeO_x$, $BaCoO_x$, and $SrCoO_x$) to span the family of compositions $Ba_{1-x}Sr_xCo_{1-y}Fe_yO_{3-\delta}$, where $x, y \in [0,1]$.

4.4 Scanning Impedance Probe: Details

4.4.1 Mechanical

Photos of the scanning impedance probe exterior are shown in Figure 4.5 and Figure 4.6. Typical sample installations are shown in Figure 4.7.

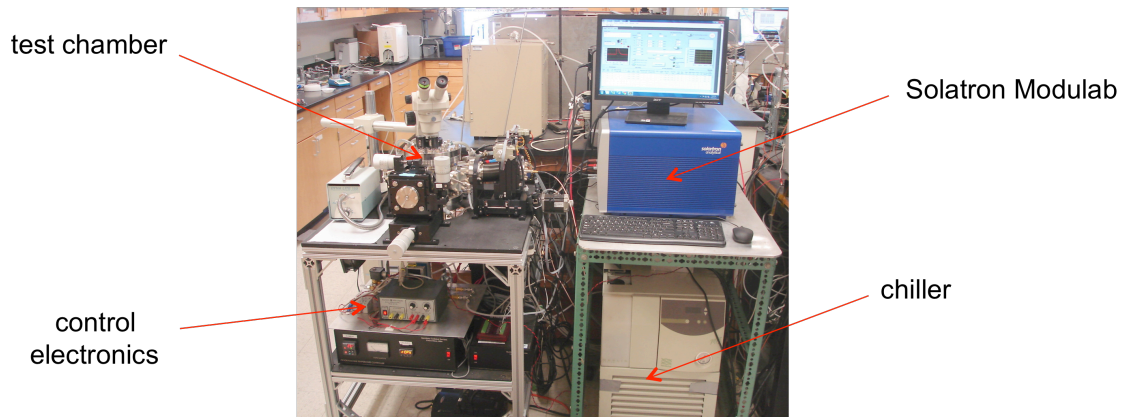


Figure 4.5. Scanning impedance probe system.

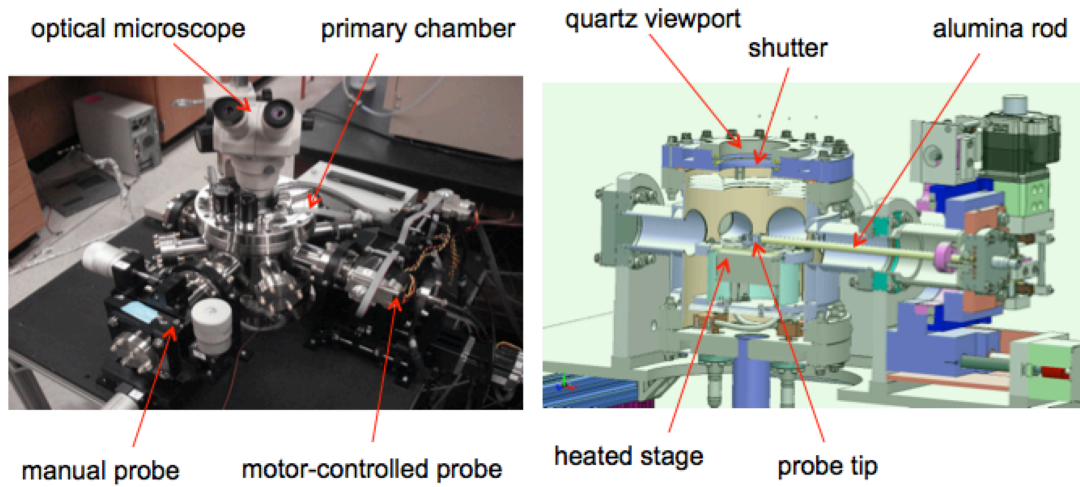


Figure 4.6. Primary chamber of the scanning impedance probe. Left: external photo. Right: computer model cross-section, showing the chamber interior.

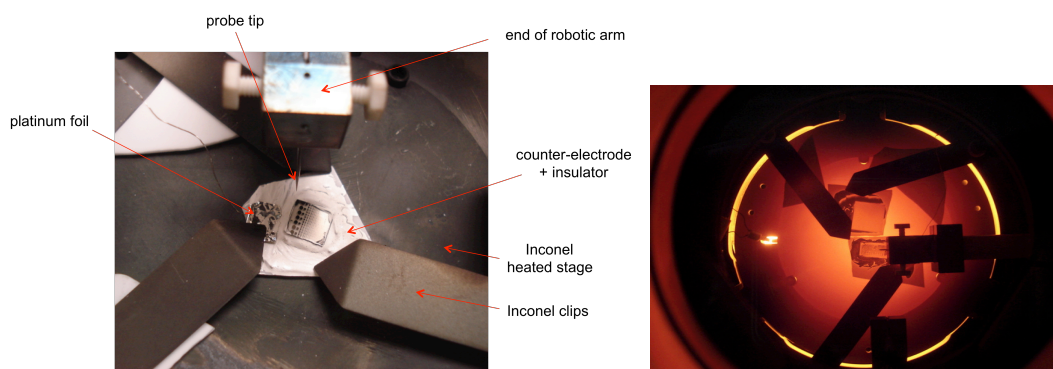


Figure 4.7. Typical sample configurations inside the scanning impedance probe. Left: at room temperature with added illumination. Right: a different sample at $\sim 800^{\circ}\text{C}$ sample temperature with no added illumination.

4.4.2 Thermal

The temperature of the Inconel stage is measured by a K-type thermocouple spot-welded to the stage underside, and can be heated well above 1000°C . In practice, a maximum stage temperature of $\sim 800^{\circ}\text{C}$ is recommended to avoid sample contamination. Green discoloration of a blank white polycrystalline alumina substrate was observed upon annealing with a stage temperature of 1000°C . Separately, Mo was detected on LSM/YSZ samples by both EDS and XPS on samples annealed for several days at a stage temperature of 840°C . No such contamination was observed on samples annealed on a 700°C stage for several days. The chamber walls, floor, and ceiling are protected from corrosion by chilled water that is circulated through internal channels, so the heating element and Inconel stage components are the likely impurity sources at $> 800^{\circ}\text{C}$.

The stage has a diameter of 50 mm, however it is visually evident in Figure 4.7 that only the central region with diameter of ~ 20 mm is heated to a uniform temperature ($< 10^\circ\text{C}$ variation, estimated by probing a representative sample in the stage center with a thermocouple attached to the system's manual probe arm).

At steady state, the stage temperature is maintained constant within $\pm 1\text{-}2^\circ\text{C}$ of the target value. However, radiative and convective cooling cause the sample surface temperature to be lower than the stage temperature. A calibration run was performed with a 0.5 mm diameter thermocouple silver-pasted to a representative YSZ substrate, as shown in Figure 4.8. The results depended slightly on whether the viewport shutter is open or closed. Equations (1) and (2) are the calibration curves. For instance, for a stage temperature of 750°C , the sample surface temperature is $\sim 720^\circ\text{C}$ with the shutter closed.

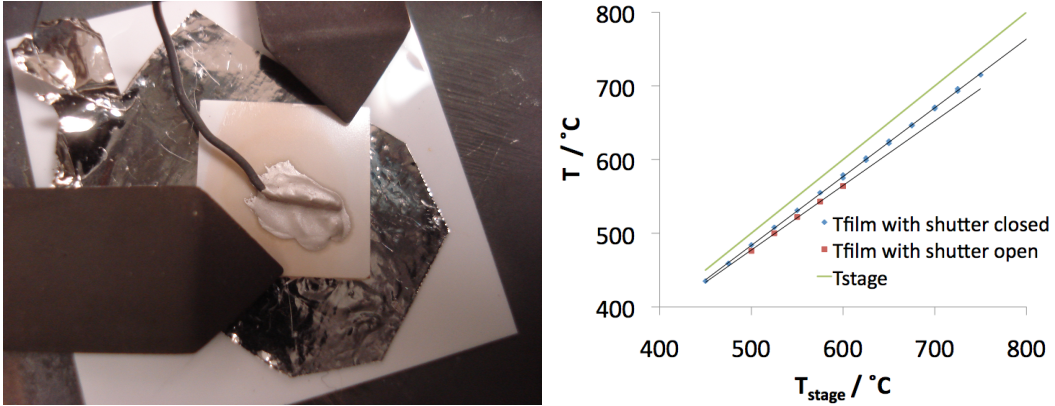


Figure 4.8. Calibration of the sample surface temperature. Left: measurement configuration. Right: Measured "film" temperature plotted vs. the stage (a.k.a. element) temperature.

$$T_{film} = 0.934T_{stage} + 17 \quad \text{shutter closed} \quad (1)$$

$$T_{film} = 0.876T_{stage} + 39 \quad \text{shutter open} \quad (2)$$

4.4.3 Gas Control

The sealed chamber is high vacuum compatible, and leak rates are low enough that using suitable inlet mixtures of nitrogen and oxygen, oxygen partial pressures below 10^{-4} atm can be maintained. All internal chamber components including the MoSi₂ heating element can nominally withstand reducing gases like hydrogen or methane. Gas mixing is accomplished with external mass flow controllers. The purge time for changing the chamber gas environment depends on the initial and final gas compositions; for oxygen-nitrogen mixtures with flow rate greater than 100 sccm, using an external oxygen sensor, the longest observed equilibration time was under 3.5 hours (which occurred when switching from 100% O₂ to 0.01% O₂). Typical purge times are under one hour. Studies under low humidity are possible if

the inlet gas is pre-humidified, and studies under high humidity may be possible if the water circulated through the chamber walls is heated instead of chilled.

4.4.4 Electronic

Either a Solartron Modulab or a Solartron 1260 impedance analyzer can be used to acquire impedance measurements. Detailed specifications for the impedance measurement accuracy can be found in the user manuals for those instruments.

4.4.5 Software

The scanning impedance probe system includes a substantial Labview-based software driver, which reads the program sequence (including which microelectrodes should be measured, and under which conditions) from an Excel spreadsheet and logs all measured data to text files.

Note that upon changing the stage temperature, the various chamber components expand and contract by varying amounts, and thus the microelectrode coordinates are different at every temperature. To account for this effect, three reference points are measured at two reference temperatures. Coordinate transformations are then used to calculate all the microelectrode positions at all temperatures, assuming the expansion effect can be linearly interpolated/extrapolated. The positional errors introduced by this assumption are modest.

4.5 Some obstacles to obtaining good data, and how to overcome them

4.5.1 Tip Cooling

The metal probe is cooler than the sample, so the probe tip has the effect of locally cooling the sample by conduction during each impedance measurement. For large enough electrodes, this local cooling can be neglected. However, as the electrode diameter decreases, a larger fraction of the electrode area will be affected by the cooling. In other words, the smaller the microelectrode diameter, the more the average electrode temperature is expected to be lowered by tip cooling.

This effect was first mentioned by Opitz and Fleig³⁵ in 2010; it appears to have been neglected in the many microelectrode papers using solid electrolytes published before 2010. Opitz and Fleig reported Seebeck voltages of tens of millivolts between the sample electrodes as a result of this cooling. A similar but smaller effect was observed in this work. Specifically, thermovoltages in the presence of tip cooling were measured as a function of stage temperature and dot diameter. The results are plotted in Figure 4.9. These results were independent of gas flow rate up to the max flow rate attempted (300 sccm). Next, the thermovoltage was measured on a relatively large area electrode (0.5 cm²) to assess the temperature drop across the sample when tip cooling is negligible. The large area makes the impact of tip cooling negligible. This Seebeck voltage can thus be attributed to convection/radiation losses only, and is shown for different temperatures as horizontal lines in Figure 4.9.

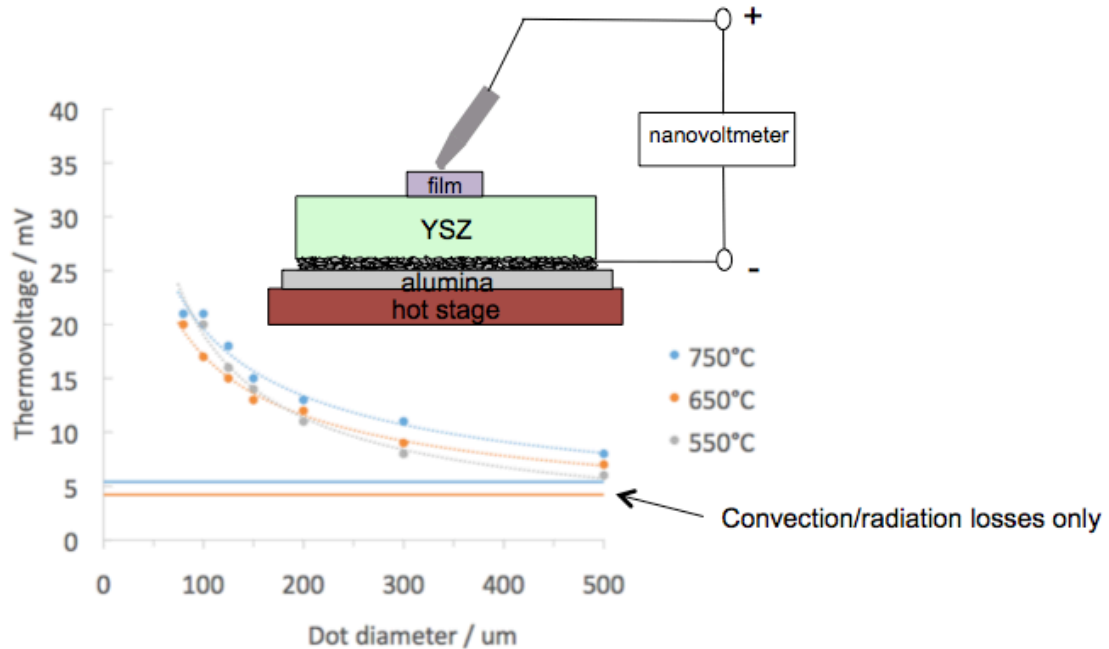


Figure 4.9. Measured voltage drop $V_{\text{film}} - V_{\text{counter electrode}}$ across the YSZ substrate using an $\text{La}_{0.5}\text{Sr}_{0.5}\text{CoO}_{3-d}$ microelectrode and a tip made of Paliney7 (a noble metal alloy containing primarily palladium).

The precise amount of tip cooling varies between measurements depending on the thermal conductivities of the sample and tip and the thermal resistance at the tip contact. Also, the temperature profile did not always instantly reach steady state; it typically took 5 s - 180 s for the thermovoltage to stabilize, with the faster times corresponding to higher temperatures or larger diameters. To correct for tip cooling, the scanning impedance probe waits for a user-specified time after contacting the sample, measures the thermovoltage, and then proceeds with the impedance measurement. The temperature drop across the sample can then be estimated from the measured thermovoltage if the substrate Seebeck coefficient is known. For example, the Seebeck coefficient of YSZ is $\sim 0.5 \text{ mV/K}$.³⁶

The ability to measure the thermovoltage immediately prior to acquiring each impedance spectrum had not yet been implemented when the data in this thesis were taken, so all reported film temperatures are corrected based on the set of thermovoltages reported in Figure 4.9. The error introduced by this approximated correction is not expected to be severe.

4.5.2 Tip scratching

Some tips easily scratch some films. The extent of scratching depends on the tip hardness, film hardness, and the contact force, which in turn depends on the geometry and stiffness of the probe. In this work it was found that Paliney7 probes (20 mm - 35 mm length, 0.5 mm shank diameter, 40 μm tip diameter) are able to repeatedly probe both oxide and metal films with negligible scratching. Paliney7 is a palladium-based noble metal alloy that exhibits good oxidation resistance, and probe tips made of Paliney7 are sold commercially for probing applications at high temperatures.

Literature reports of microelectrode measurements typically use PtIr or Pt-plated tungsten, however the former were found to frequently scratch both metal films (*e.g.*, Pt) and oxide films (*e.g.*, LaSrMnO₃), while with the latter, the plating appeared to scrape off over time, leading to tungsten oxide growth and distorted measurements.

4.5.3 Electronic noise and artifacts

The control thermocouple (spot-welded to the underside of the stage) acts as a pathway for electrical noise to enter the chamber, which otherwise acts as a Faraday cage. The impact of this noise can be minimized by: (1) installing samples such that the counter-electrode is electrically insulated from the stage; (2) increasing the applied perturbation voltage; (3) not connecting multiple thermocouples to the stage; and (4) electrically shielding the thermocouple wire exiting the bottom of the chamber.

Temperature fluctuations can also add noise to the measured impedance spectra, and in particular, the chamber heating control is sensitive to fluctuations in electrical voltage in the heater power supply. For example, plugging a small chiller into the same outlet as the heater can cause temperature fluctuations of several degrees that add significant noise to the measured impedance spectra, particularly at low frequencies. It is recommended that the heater power cable be given a power conditioner and a dedicated outlet.

The Solartron Modulab impedance analyzer has software flaws that can cause it to violate its accuracy specifications. First, at high frequencies the Modulab "auto-current-ranging" algorithm typically chooses a suboptimal current range, which leads to spurious inductance that distorts high frequency features, as shown at left in Figure 4.10. At the time of writing, the manufacturer claimed to be working on a solution. In the meantime, a custom auto-ranging algorithm was implemented in

Labview which eliminates this spurious inductance by dividing a single impedance spectrum into several scans at different current ranges. However, a second flaw in the Modulab software makes it impossible to avoid switching to open circuit between scans, which causes spurious "jumps" when the circuit under test has a small capacitance. An example of such a jump is shown at right in Figure 4.10. Also, briefly switching to open circuit between scans has the effect of turning off and on any d.c. bias that is applied, which can introduce artifacts into impedance measurements under d.c. bias. Until the manufacturer produces a revised software driver, bias measurements and measurements on samples with low capacitance should use the Modulab auto-ranging algorithm, with a correction at high frequencies to account for the spurious inductance. For all other measurements, the custom auto-ranging is probably more accurate.

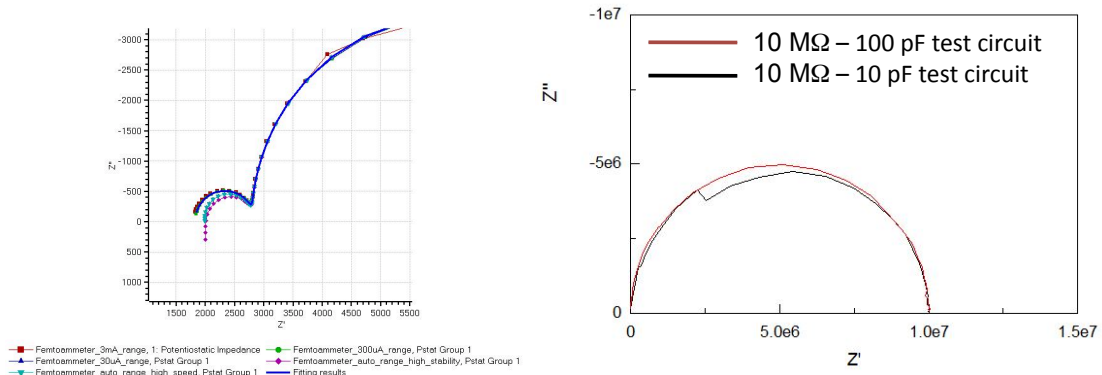


Figure 4.10. Left: Spurious inductance at high frequencies, caused by improper choice of current range. Right: Spurious jump in the data upon changing current ranges for low capacitance samples.

4.5.4 Contamination

Molybdenum contamination has been observed on some films after prolonged testing in the scanning impedance probe at elevated temperatures. Specifically, MoO_3 particles were detected on LaSrMnO_3 films by XPS, SEM, and EDS after 130 h testing at $T_{\text{stage}} = 840^\circ\text{C}$. The particles were not observed on the surrounding YSZ substrate. Films tested for a similar time no higher than $T_{\text{stage}} = 750^\circ\text{C}$ exhibited no such contamination. The chamber has a MoSi_2 heating element and a stage made of Inconel 625 (a nickel superalloy that contains Mo), and these are likely responsible for the contamination. For operation above $T_{\text{stage}} = 750^\circ\text{C}$, blocking gaps to the heating element and switching to a Mo-free stage (*e.g.*, Inconel 600) are recommended.

Silver contamination has also been observed on some films after testing. Specifically, silver particles were detected by XPS, SEM, and EDS after testing up to $T_{\text{stage}} = 675^\circ\text{C}$ for samples prepared with a silver paste counter electrode. Evidently silver is quite mobile in oxygen-containing atmospheres, and although the film's bulk properties are likely unaffected, the presence of silver may have an impact on catalytic activity.⁵¹ As such, the use of silver should probably be avoided in most surface studies. Some of the results reported in the next chapter are preliminary in nature and used a silver counter electrode for expediency.

4.5.5 Sheet resistance

Sheet resistance may contribute to the impedance spectra of microelectrodes that are sufficiently thin with sufficiently large diameter and low electronic conductivity. This contribution can distort the impedance spectra at high frequencies, while typically leaving the low frequency fit parameters largely unaffected.¹⁵ In this work, owing to the high electronic conductivity of the film materials studied, sheet resistance made a small contribution to the measured offset resistance and was otherwise negligible.

CHAPTER 5 BULK PROPERTIES OF SCN

5.1 Summary

Here begins the second half of this thesis, focusing on bulk defect chemistry. Section 5.2 reviews the motivation presented in Chapter 1 for studying bulk defect chemistry in perovskites containing strontium and cobalt. Section 5.3 gives experimental details, Section 5.4 gives the results, and Section 5.5 reviews the findings.

5.2 Why study the bulk defect chemistry of $\text{SrCo}_{0.9}\text{Nb}_{0.1}\text{O}_{3-\delta}$ (SCN)?

In this chapter the oxygen nonstoichiometry, bulk impedance behavior, and expansion behavior of SCN are characterized. The oxygen nonstoichiometry and electronic behavior are clearly relevant to the catalytic behavior, while the expansion behavior is also interesting both from a theoretical perspective (since expansion is directly related to vacancy formation, electronic redistribution, etc.) and from an application perspective (since in applications, larger expansion typically leads to higher stresses and greater likelihood of crack formation at the cathode/electrolyte interface). SCN represents a reasonable choice of a "model material" for fundamental studies of SOFC catalysts with the perovskite structure that contain Sr and Co.

5.3 Experimental details

Phase-pure SCN powder was synthesized by conventional solid state reaction. Stoichiometric quantities of SrCO_3 , Co_3O_4 , and Nb_2O_5 (all from Alfa Aesar, > 99.7% purity) were mixed, attritor-milled at 500 rpm for 30 min with 3 mm yttria-stabilized zirconia beads in acetone or isopropanol, removed from the milling media, dried at 110°C, and calcined for 15 h in stagnant air at 1200°C. In some cases, powders were milled again and recalcined at 1200°C an additional 10 h. For comparison, phase-pure powders with the nominal compositions $\text{Ba}_{0.5}\text{Sr}_{0.5}\text{Co}_{0.8}\text{Fe}_{0.2}\text{O}_{3-\delta}$ and SrCoO_3 were synthesized by a chemical solution method reported previously.³⁷ X-ray diffraction (XRD) (Philips X'Pert Pro, Cu Ka) confirmed that the calcined powders were cubic perovskites. To assess phase stability, a sample of this SCN powder was placed in an alumina boat in a quartz tube and subject to anneals in stagnant air for 750°C for 4 days, then 750°C for 6 more days, then 1200°C for 10 h, with XRD patterns acquired after each of these anneals.

Dense compacts were prepared from powders to which 1.25 wt% polyvinylpyrrolidone was added to serve as a binder. The powders were subjected to uniaxial pressure under 2 tons for 10 min followed by isostatic pressure under 350 MPa for 20 min. Sintering was carried out at 1100°C for 10 h in stagnant air. Prior to further characterization, the compact surfaces were polished using a final grit size of 0.3 mm. Electron microprobe (JEOL JXA-8200) analysis was employed for chemical analysis from a representative pellet of each composition, using BaTiO_3 , SrTiO_3 , Co, Fe, and Nb standards. At least six locations were probed, and the results were averaged. The relative cation amounts measured in the samples were converted into chemical formulas by assuming no interstitial cations and minimizing the number of cation vacancies. The resulting chemical formulas were $\text{Ba}_{0.50}\text{Sr}_{0.49\pm 0.01}\text{Co}_{0.77\pm 0.01}\text{Fe}_{0.21\pm 0.01}\text{O}_{3-\delta}$ and $\text{SrCo}_{0.91\pm 0.01}\text{Nb}_{0.09\pm 0.01}\text{O}_{3-\delta}$. Micrographs taken using the same instrument indicated that the BSCF compacts had very little porosity; however, the SCN compacts were typically 30% - 55% porous. Accordingly all measured bulk resistances of SCN were multiplied by a correction factor to account for this porosity.

In all the measurements described below, the gas atmosphere was achieved by flowing premixed gases with various amounts of O_2 and N_2 ; the oxygen partial pressure of each gas composition was verified using a zirconia-based oxygen sensor (Setnag); measurements were typically made over an oxygen partial pressure range of 10^{-4} atm - 1 atm and over the temperature range 500°C - 1000°C (except 600°C - 900°C was used for the impedance measurements); and for each material and gas composition, the temperature was changed in 100°C increments and measurements were taken continuously until equilibrium was reached. Equilibration times were 0.5 h - 2.5 h for powder samples and 0.5 h - 4 h for bar samples. BSCF exhibits a slow partial decomposition to a mixture of cubic and hexagonal phases⁶¹⁻⁶⁴, so samples of this material were frequently annealed at 1000°C during the measurement sequence to restore the pure cubic phase.

Thermogravimetry (TG) measurements were performed on powder samples with a typical mass of 220 mg in a Netzsch STA 449C thermal analyzer using a platinum crucible. The equilibrated sample masses were frequently re-measured at a "baseline condition" of 800°C and 0.01 atm O₂ in order to monitor and correct for instrument drift (typically < 10 mg/h). Buoyancy- and drift-corrected mass changes between environmental conditions were attributed to changes in oxygen content; thus the relative oxygen stoichiometry at all conditions was determined. In order to translate the relative oxygen stoichiometries implied by these measurements into absolute stoichiometries, powder samples were heated to a reference state of 1000°C in 0.20 atm O₂, and subsequently fully reduced (Ba,Sr)O + Co + Fe or SrO + Co + SrNbO₃ by exposure to inert gas and then 6-8% H₂. The mass difference at 1000°C between the (equilibrated) reference state and the reduction products provided the absolute oxygen stoichiometry of the reference state. Complete reduction to the indicated products was verified using both *ex situ* XRD (on the reduction products) and *in situ* XRD (probing the reduction of a different sample under equivalent conditions). The reductions were performed twice for each material to verify reproducibility.

Bulk conductivity was measured using an impedance analyzer (Solartron 1260) and right rectangular prism samples of typical dimensions 23.5 mm × 5.4 mm × 0.25 mm. The samples were made thin so as to increase their resistance (thereby improving measurement accuracy) and surface-area-to-volume ratio (thereby decreasing equilibration times). Two sets of measurements were performed. In the first set, data were collected on BSCF over the frequency range 10⁻² Hz to 10⁷ Hz with zero d.c. bias and 10 mV - 40 mV perturbation voltage. Porous platinum ink (BASF A3788) was spread on the distant ends of the compact, fired at 950°C for 2 h, and verified by scanning electron microscopy (SEM, Hitachi S-4100) to be porous and uniform. Electrical contact was made to the platinum using gold wires attached with silver paste (SPI 05063-AB). A second set of measurements was performed on both materials with the platinum paste omitted and at a fixed frequency of 100 Hz (again with zero d.c. bias and 10 mV - 40 mV perturbation voltage). Short circuit measurements were made to measure and correct for the resistance of the experimental apparatus. The total electrical conductivity was calculated from the corrected sample resistance (typically 1 W - 40 W) and the sample geometry.

The expansion behavior of SCN was measured by taking *in situ* x-ray diffraction patterns (Philips X'Pert Pro, Cu Ka) on a bulk powder sample supported by an alumina cup and equilibrated in various environmental conditions in an Anton-Paar HTK 1200 chamber. The lattice parameter a_0 of SCN at each measured condition was determined from the corresponding diffraction pattern using a Nelson-Riley plot⁶⁵. After the experiment, the alumina cup was observed to have a slight bluish tinge, indicating a very minor degree of interfacial reactivity between SCN and the alumina. However, this reactivity could be neglected; the bottom of the alumina cup where the interfacial reaction occurred was two orders of magnitude deeper than the x-ray penetration length.

5.4 Results and discussion

After calcining, SCN was found to have the cubic perovskite crystal structure at 25°C. By contrast, SrCoO₃ was found to have segregated into two phases at 25°C, Sr₆Co₅O₁₅ and Co₃O₄, consistent with literature findings.⁶⁶ Upon annealing at 750°C for 10 d, SCN remained mostly in the cubic perovskite phase, but exhibited additional reflections that were indexable to the phases Sr₆Co₅O₁₅ and Co₃O₄, as shown in Figure 5.1. This decomposition was reversed by re-annealing at 1200°C, as shown. Additional TG measurements (not shown) involving repeated temperature cycles between 1000°C and 750°C found that re-annealing at 1000°C was sufficient to reverse the slow mass change observed at 750°C, and that the mass was stable with time at 1000°C. These results indicate that the 10% niobium doping in SCN successfully stabilizes the cubic perovskite phase at 1000°C, however at lower temperatures this phase is metastable. Similarly, BSCF powder was also found to be stable at 950°C and metastable at 750°C. The impact of the metastability was minimized in the *in situ* studies reported below by frequently annealing the SCN (or BSCF) at 1000°C to restore the cubic phase.

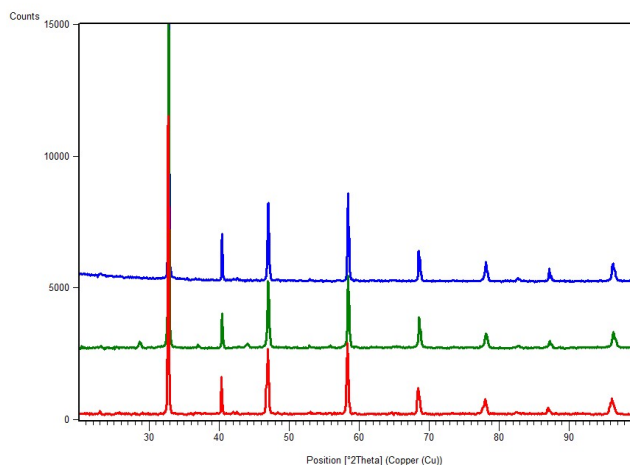


Figure 5.1. X-ray powder diffraction patterns for SCN after calcination at 1200°C (red), after a subsequent anneal at 750°C in air for 10 d (green), and after a subsequent additional anneal at 1200°C in air for 10 h (blue).

The oxygen stoichiometry diagrams deduced from the thermogravimetry results are presented in Figure 5.2. Selected literature data are shown for comparison. The trends with temperature and oxygen partial pressure are quite similar between the two materials, apparently due to the cobalt ion.

Multiple reports of the oxygen stoichiometry phase diagram of BSCF exist in the literature.^{63,67-69} The trends with temperature and oxygen partial pressure are consistent across these reports, but the absolute values differ substantially, apparently due to discrepancies in the reference state measurements. The BSCF reference state obtained in this study using thermogravimetry is identical to that obtained in a recent report by Kriegel *et al.*⁶³ that employed cerimetric titration. By contrast, Mueller *et al.* found a different reference point by a novel coulometric titration method, however it is not clear that their conclusion should be considered

definitive, since it appears to be based on a single data point from a single titration curve.⁶⁹

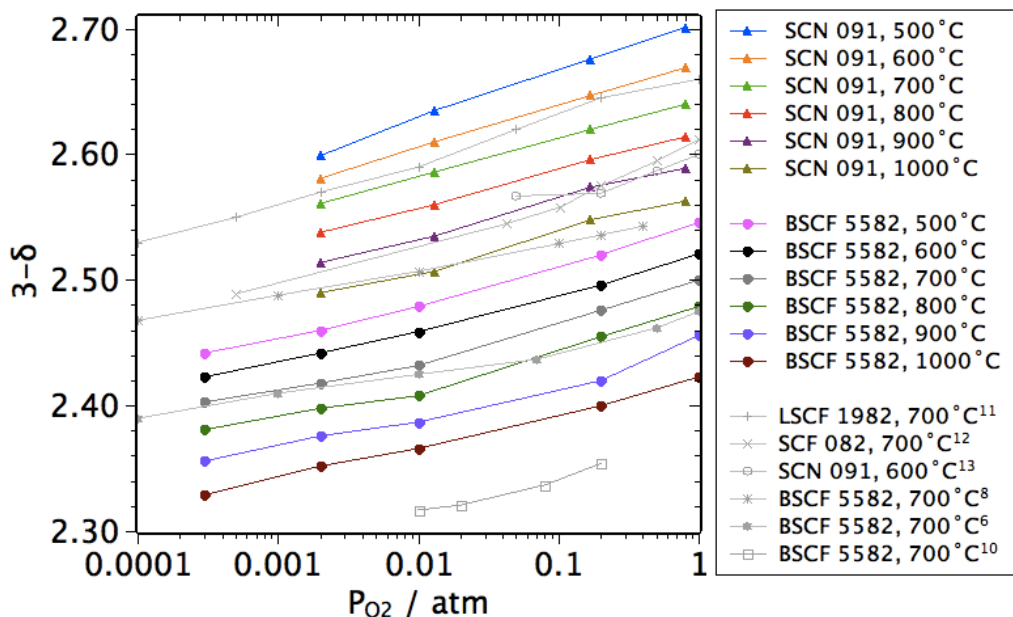


Figure 5.2. Oxygen stoichiometry $3-\delta$ of BSCF and SCN measured by thermogravimetry, plotted for comparison with data from other reports on $\text{La}_{0.1}\text{Sr}_{0.9}\text{Co}_{0.8}\text{Fe}_{0.2}\text{O}_{3-\delta}$ (LSCF 1982)⁷⁰, $\text{SrCo}_{0.8}\text{Fe}_{0.2}\text{O}_{3-\delta}$ (SCF 082)⁷¹, SCN⁷², and BSCF^{63,67,69}.

Mueller *et al.* suggested some plausible sources of error in earlier studies that could account for the reference state discrepancies.⁶⁹ One consideration is worth adding to their excellent discussion: it appears that some earlier studies used a sample at room temperature as a reference point. This practice is potentially unreliable, because differences in oxygen uptake can occur between samples that are cooled to room temperature at different rates or with different geometries, or even between two powder samples taken from the surface and

interior of the same pile of powder. Thus, a metastable reference sample can be non-representative of other metastable test samples. This problem can be solved by choosing a reference state where the material is in stable equilibrium. Additionally, surface carbonates can form during powder storage due to a slow reaction with ambient carbon dioxide, and the subsequent burning off of the carbon during thermogravimetric analysis causes an additional mass loss that may be incorrectly interpreted as oxygen loss, thus leading to a calculated δ value for the reference state that is too large. Again the solution is to choose a high temperature reference state at which carbonates are not present.

Note also that for this type of compound, common chemical analysis techniques have an uncertainty of at least 1% - 2% in determining any given cation ratio, thereby contributing additional uncertainty to the reference state calculation. In the present study, BaTiO_3 and SrTiO_3 were used as elemental standards, since using standards with similar crystal structure as the sample helps to maximize the accuracy of electron probe microanalysis.

Given all these considerations, error bars for the oxygen stoichiometry values measured in this paper are estimated as ± 0.10 (absolute) and ± 0.02 (relative for each material).

Turning to the transport behavior, the complex impedance of the platinum-electroded BSCF compact was constant with negligible imaginary component over the frequency range 10^{-1} Hz - 10^5 Hz. A very small electrode arc was observed in the range 10^{-3} Hz - 10^{-1} Hz, which contributed to the overall DC resistance by less than 3%. These measurements include contributions from both electron and

oxygen ion carriers, but the negligible contribution of the electrode arc and the high total conductivity indicate that electronic transport is dominant with a transference number close to one.²⁶ This result is not surprising; the $\text{La}_{1-x}\text{Sr}_x\text{Co}_{1-x}\text{Fe}_x\text{O}_{3-\delta}$ family of materials also have electronic transference numbers approaching unity.³ Accordingly, the total electrical conductivity can be equated with negligible loss of accuracy to the electronic conductivity, and single frequency measurements are justified.

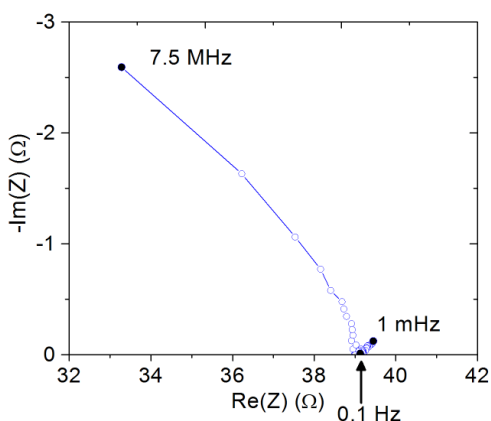


Figure 5.3. Impedance spectrum of $\text{Ba}_{0.5}\text{Sr}_{0.5}\text{Co}_{0.8}\text{Fe}_{0.2}\text{O}_{3-\delta}$ at 600°C in 2×10^{-5} atm O_2 .

The electronic conductivity of BSCF and SCN are plotted in Figure 5.4 as isotherms and isobars. Selected literature data are again included for comparison. As the oxygen partial pressure increases along the isotherms, oxygen atoms are incorporated (Figure 5.2), and in becoming ions they pull electrons from other ions in the material. The electronic conductivities are seen to increase, so holes are the majority carrier; that is, both materials are p-type.

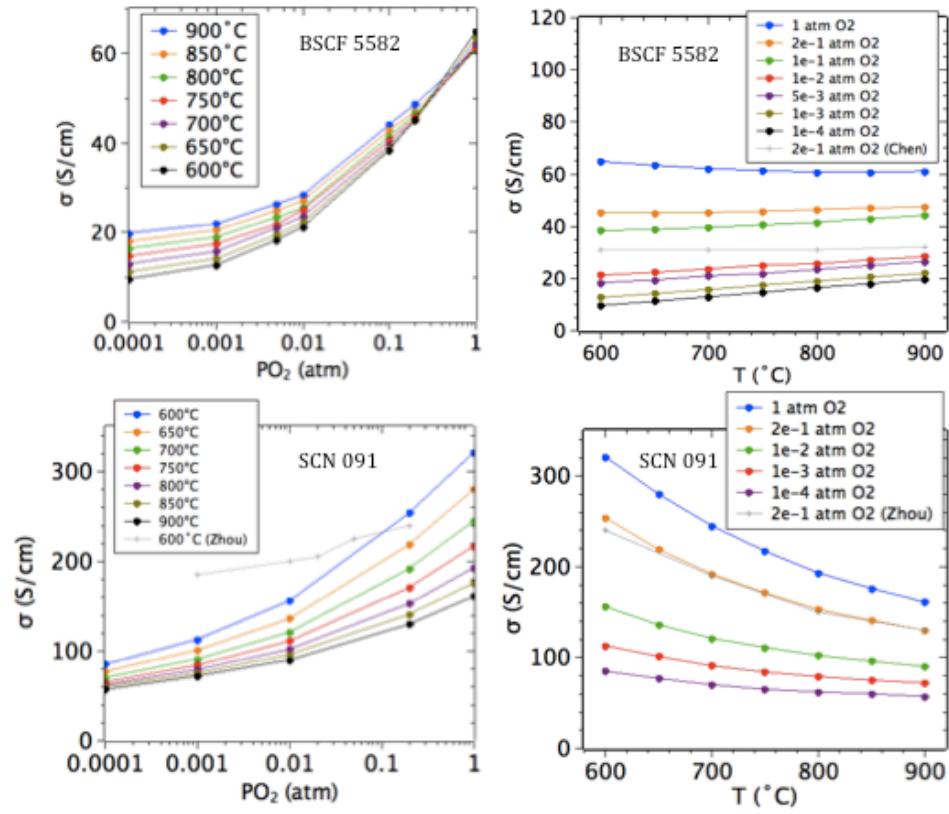


Figure 5.4. Electronic conductivity σ . (a) BSCF isotherms, (b) BSCF isobars, (c) SCN isotherms, and (d) SCN isobars, plotted with comparable literature data.^{72,73}

Along some of the isobars, the electronic conductivity decreases as temperature increases. In many materials such a trend suggests metallic behavior, *i.e.*, itinerant carriers whose mobility is reduced at higher temperatures due to increased phonon scattering. One previous report did indeed claim on the basis of this trend that BSCF exhibits metallic behavior.⁷⁴ In these materials, however, conclusions about mobility and transport mechanisms can only be legitimately drawn after accounting for changes in carrier concentration due to redox reactions. Here we access the desired “iso-stoichiometric” values of conductivity by assuming that fixed oxygen stoichiometry corresponds to fixed carrier concentration. In other words, we neglect changes of the mobile carrier concentration with temperature due to disproportionation reactions (*e.g.*, $2\text{Co}^{3+} \rightarrow \text{Co}^{2+} + \text{Co}^{4+}$) and internal charge transfer reactions (*e.g.*, $\text{Fe}^{3+} + \text{Co}^{4+} \rightarrow \text{Fe}^{4+} + \text{Co}^{3+}$). While this assumption may not be entirely justified, the relatively small temperature range of the analysis limits the associated error; the assumption is a possible source of error for the calculated $\Delta_m H$ values, but it seems unlikely to undermine the overall conclusions drawn below.

It can be shown that materials with hopping conductivity and fixed electronic carrier concentrations exhibit Arrhenius behavior, *i.e.*, satisfy the expression

$$\ln(\sigma T) = \ln(C) + \frac{\Delta_m H}{k_B T} \quad (3)$$

where σ is the electronic conductivity, T is temperature, $\Delta_m H$ is the enthalpy of hole migration (*i.e.*, the activation energy for hole hopping between sites), k_B is

Boltzmann's constant, and C is a constant accounting for the entropy of hole migration $\Delta_m S$ and other terms.⁷⁵ Figure 5.5 shows $\log(\sigma^*T)$ plotted as a function of T^{-1} while keeping δ fixed; this figure combines the oxygen stoichiometry and electronic conductivity results shown earlier. Specifically, linear fits to the isotherms in Figure 5.2 and parabolic fits to the isotherms in Figure 5.4 (all of which showed good agreement with the data) were used to interpolate those data and thereby produce the points in Figure 5.5.

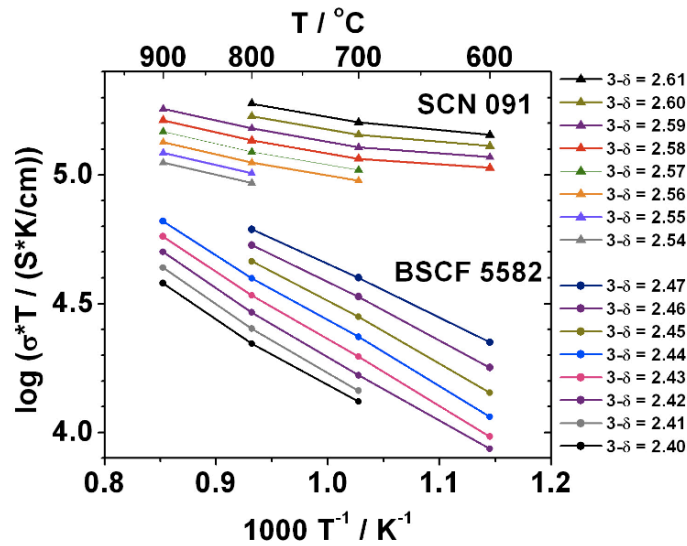


Figure 5.5. Electronic conductivity σ of BSCF and SCN plotted as iso-stoichiometric curves. Lines connect the data points as guides for the eye.

For fixed carrier concentration, conductivity clearly increases with increasing temperature for both SCN and BSCF, indicating that under the conditions studied, these materials are not metallic conductors; rather, they are thermally activated conductors with localized holes. From the slopes in the above plot, the enthalpy of migration $\Delta_m H$ is found to be 0.4 eV - 0.5 eV for BSCF and 0.1 eV - 0.2 eV for SCN.

These values are physically plausible, and for comparison, the enthalpy of electron migration in $\text{Sm}_{0.15}\text{Ce}_{0.85}\text{O}_{1.925-\delta}$ (a material that is well-known to conduct electrons by small polaron hopping) is 0.2 eV.²⁶

Turning finally to the expansion behavior, Figure 5.6 shows the lattice parameter a_0 of SCN measured using *in situ* XRD as a function of temperature and oxygen partial pressure. Comparable literature data for BSCF (taken using *in situ* neutron diffraction) are shown for comparison. The same SCN lattice parameter data are plotted (again alongside comparable literature data for BSCF) in Figure 5.7 as a function of δ and temperature, where the values of δ were determined by interpolating linear fits to the isotherms in Figure 5.2.

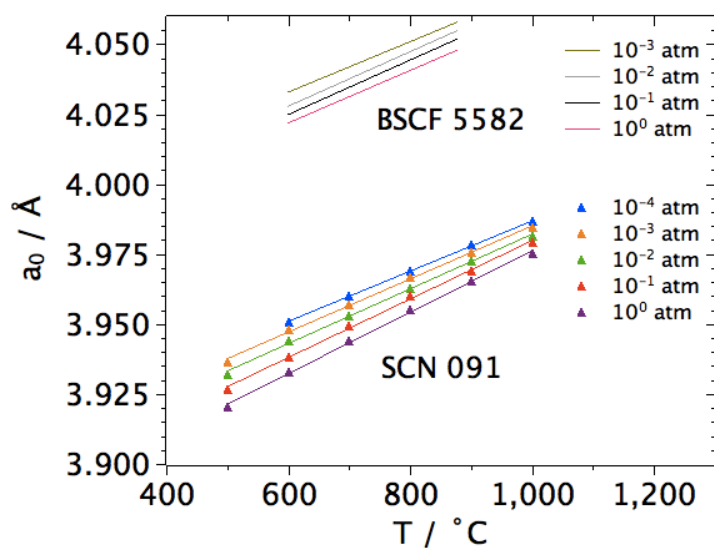


Figure 5.6. Lattice parameter a_0 of equilibrated SCN measured by *in situ* x-ray diffraction. Curves shown are linear fits to the data. Also plotted are comparable literature data for equilibrated BSCF taken by neutron diffraction.⁶⁸

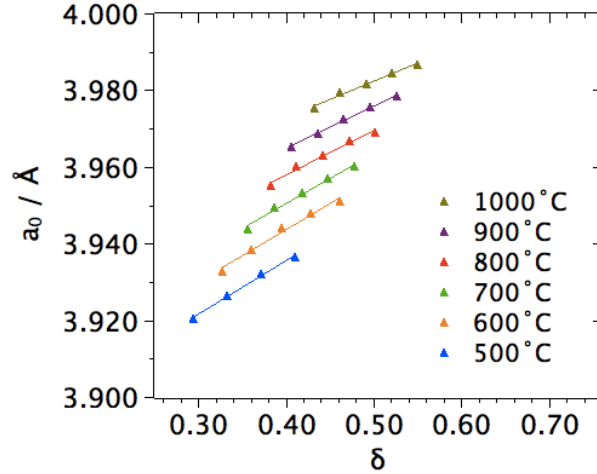


Figure 5.7. Lattice parameter a_0 of equilibrated SCN, plotted as a function of oxygen non-stoichiometry δ . Curves shown are linear fits to the data. Error bars for d are estimated as ± 0.10 (absolute) and ± 0.02 (relative).

From these data the linear expansivity α_l , the linear chemical expansivity α_c , and the linear thermal expansivity α_t can be determined by

$$\alpha_l \equiv \frac{1}{l} \left(\frac{\partial l}{\partial T} \right)_{P_{O_2}} = \frac{1}{a_0} \left(\frac{\partial a_0}{\partial T} \right)_{P_{O_2}} \quad (4)$$

$$\alpha_c \equiv \frac{1}{l} \left(\frac{\partial l}{\partial \delta} \right)_T = \frac{1}{a_0} \left(\frac{\partial a_0}{\partial \delta} \right)_T \quad (5)$$

$$\alpha_t \equiv \frac{1}{l} \left(\frac{\partial l}{\partial T} \right)_\delta = \frac{1}{a_0} \left(\frac{\partial a_0}{\partial T} \right)_\delta \approx \left(\frac{\Delta(\ln a_0)}{\Delta T} \right)_\delta \quad (6)$$

where a_0 and l are the lattice parameter and macroscopic length. The first definition is standard;⁷⁶ the latter two definitions are linear versions of the volumetric expansivities described by Adler.⁷⁷ Note that linear expansivity includes the effects of both thermal and chemical expansion, and thus is sometimes

referred to as the total expansion coefficient. Note also that the unit cell is assumed to be uniform throughout the sample, so that macroscopic expansion (changes in l) and unit cell expansion (changes in a_0) can be taken as equivalent. Thus it is possible to calculate a_l from the slopes of the isobars in Figure 5.6, a_c from the slopes of the isotherms in Figure 5.7, and a_t from applying Equation 6 to adjacent points with the same δ in Figure 5.7. The results for a_l and a_c are shown in Figure 5.8 and Figure 5.9, and a_t for SCN was determined to be $a_t = (18 \pm 2) \cdot 10^{-6} \text{ K}^{-1}$ over the range of conditions studied; it showed no clear trend with temperature or δ . For comparison, the thermal expansivity of BSCF is reported to be $(20 \pm 1) \cdot 10^{-6} \text{ K}^{-1}$ over a comparable range of conditions.⁶⁸

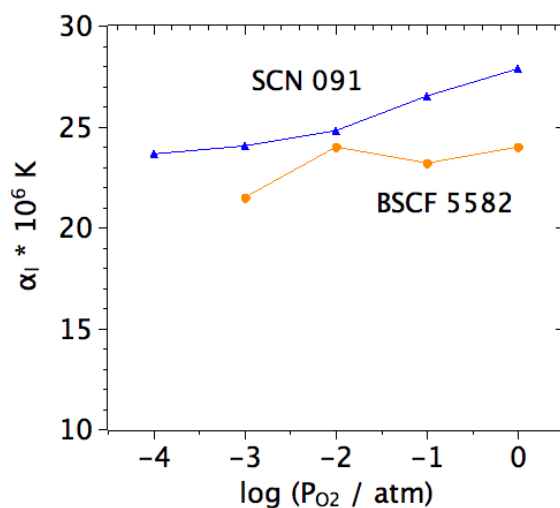


Figure 5.8. Linear expansivity a_l of SCN plotted with comparable literature data for BSCF.⁶⁸

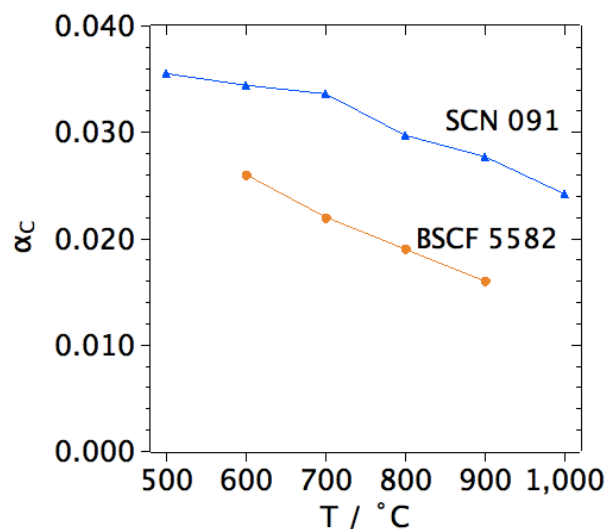


Figure 5.9. Linear chemical expansivity α_c of SCN plotted with comparable literature data for BSCF.⁶⁸

These results indicate that the thermal expansivities of the two materials are comparable, and that SCN has a larger chemical expansivity and thus a slightly larger total expansivity than BSCF.

As an aside, a recent computational study on $\text{CeO}_{2-\delta}$ and $\text{BaCeO}_{3-\delta}$ suggested that materials with smaller degree of charge localization have smaller α_c .⁷⁸ However the comparison of SCN and BSCF appears to provide a counterexample, since SCN has a smaller degree of charge localization (smaller $\Delta_m H$) but a larger α_c than BSCF.

5.5 Conclusions

SCN is metastable at fuel cell operating temperatures. The kinetics of decomposition are fairly slow, however, and contribute minimal error on the time scale of many laboratory measurements. SCN is a thermally activated hole

conductor, and in comparison with the current state-of-the-art material, $\text{Ba}_{0.5}\text{Sr}_{0.5}\text{Co}_{0.8}\text{Fe}_{0.2}\text{O}_{3-\delta}$ (BSCF), SCN has smaller oxygen nonstoichiometry, five times higher electronic conductivity, lower enthalpy of hole migration, somewhat improved structural stability, comparable thermal expansivity, and slightly larger total and chemical expansivities.

CHAPTER 6 ELECTRONIC BEHAVIOR OF $\text{SrCo}_{0.9}\text{Nb}_{0.1}\text{O}_{3-\delta}$

6.1 Summary

This chapter studies the electronic behavior of $\text{SrCo}_{0.9}\text{Nb}_{0.1}\text{O}_{3-\delta}$ (SCN) using several x-ray techniques. Section 6.2 motivates the sample preparation and experimental techniques used. Section 6.3 provides experimental details. Section 6.4 discusses the findings. It is shown that thermogravimetric quenching enables preparation and simultaneous characterization of SCN pellet samples with a wide range of oxygen stoichiometries. Then, x-ray absorption near-edge spectroscopy (XANES), x-ray diffraction (XRD), and x-ray photoelectron spectroscopy (XPS) are used to characterize these quenched pellets. The results confirm that strontium and niobium in SCN are fixed-valent, and that the average valence of cobalt decreases monotonically with decreasing oxygen content. Finally, *in situ* non-resonant inelastic x-ray scattering (NRIXS) is used to probe the bulk electronic structure in equilibrium at high temperatures. The resulting oxygen K edge structures provide strong evidence that at high temperatures SCN has substantial covalency between the oxygen 2p and cobalt 3d states. The implications of this covalency are discussed.

6.2 Background

Solid state chemists have theorized for decades that the metallic conductivity of stoichiometric $\text{SrCoO}_{3.00}$ is due to covalent character in the bonding, and a number

of experimental and computational studies have reported evidence for this theory at or below room temperature. However, these results are obtained from quenched (thermodynamically unstable but kinetically stable) samples of $\text{SrCoO}_{3.00}$. It is not obvious that such covalency will persist at high temperatures for highly non-stoichiometric oxides in equilibrium. Ideally, a study could probe a non-stoichiometric oxide with varying oxygen contents under both quenched and equilibrium conditions.

Such a study is the subject of this chapter. Samples of $\text{SrCo}_{0.9}\text{Nb}_{0.1}\text{O}_{3-\delta}$ were examined in two forms: *ex situ* in a quenched state at room temperature, and *in situ* in equilibrium at high temperature. First, traditional x-ray photoelectron spectroscopy (XPS) was used *ex situ* to acquire cobalt L_{23} edges. These edge structures exhibited no significant differences between different oxygen contents, however, so in subsequent measurements, x-ray absorption methods were pursued. For the cations, x-ray absorption fine structure (XAFS) edges are measured in the conventional way. For the oxygen ions, the situation is more challenging. Since oxygen 1s electrons have a binding energy of ~ 532 eV, conventional techniques for probing the structure of oxygen edges (EELS, XPS, and soft x-ray absorption) must use lower energy electrons or x-rays that require near-vacuum conditions and that do not penetrate deeply into samples. These limitations are severe, because it becomes impossible to measure edge changes under the atmospheres that are of greatest interest to applications. Moreover, the results are surface sensitive and thus the assignment of edge changes to bulk

chemical effects is clouded. Furthermore, as a result of the vacuum requirement, the samples would need to be "quenched", i.e., metastable and out of equilibrium, when the goal is to probe the equilibrium state.

For these reasons, the oxygen K edges were acquired using a somewhat unconventional technique, non-resonant inelastic x-ray scattering (NRIXS). This technique is described in more detail in the literature.⁷⁹ In brief, NRIXS measures the cross section for inelastic scattering of hard x-rays such that the energy lost by the incident x-ray is equivalent to the excitation energy of the electronic transition of interest. Thus low-energy excitations (like the oxygen K edge) can be probed using high-energy (penetrating) x-rays. This tremendous advantage makes NRIXS compatible with *in situ* controlled atmosphere experiments, and a penetration depth > 10 μm makes NRIXS truly bulk-sensitive.

The disadvantage of NRIXS is that the cross section is extremely small. Acquiring sufficient signal to have meaningful results typically requires an insertion device at a third-generation synchrotron source, an array of detectors, and long acquisition times on the order of 1 h - 8 h per edge.

6.3 Experimental details

6.3.1 Synthesis

SCN powder was synthesized by solid state reaction as described in Chapter 5, except the powder was fired in two stages: first at 1150°C for 15 h, then (a small impurity-phase reflection attributed to incomplete calcination was observed at ~

31° by x-ray diffraction (XRD, Philips X'Pert Pro, Cu K α) the powder was attritor milled for another 45 min, dried at 115°C, fired at 1200°C for 10 h, and gently ground with a mortar and pestle. Single phase cubic perovskite SCN was obtained. La_{0.6}Sr_{0.4}FeO_{3- δ} powder was obtained from a commercial supplier (Praxair, 99.9% pure, 0.4 μ m - 10 μ m particle sizes).

Compacts for the quenched pellet studies described below were prepared by adding 13 mg polyvinylpyrrolidone (dissolved in isopropanol) to 1.3 g of the above SCN powder to serve as binder. The powder was then pressed uniaxially in a 19 mm diameter die at 2.5 tons for 10 min, removed from the press, covered with an upside-down beaker, and left in stagnant air overnight. The compact was heated slowly to 500°C to remove the binder, then sintered at 1200°C for 10 h. An identical powder compact was placed underneath the sample to prevent contamination from the alumina support during sintering. The resulting pellet was polished to a 600 grit level and cut using a Buehler Isomet low-speed saw into six smaller pellets. These pellets were then sonicated sequentially in acetone, distilled water, and isopropanol to remove any residual sandpaper particles or cutting fluid, and dried at 120°C.

6.3.2 Quenching

Pellet quenching and simultaneous thermogravimetry were carried out in a Netzsch STA 449C thermal analyzer using a platinum crucible. The desired gas atmospheres were obtained by flowing premixed gases with various amounts of O₂ and N₂. The first pellet was weighed at 25°C using the thermal analyzer, heated to high temperature, allowed to equilibrate in a certain gas atmosphere, and then cooled at 50°C/min to room temperature. A baseline run with an empty crucible and identical heating and gas profile was carried out immediately prior to the quenching, and this run was subsequently subtracted from the quenching run to correct for mass changes due to buoyancy effects. Two mass differences were extracted from this profile: between the equilibrated high temperature state and the initial unquenched 25°C state, and between the equilibrated high temperature state and the final quenched 25°C state. These mass differences were attributed entirely to changes in oxygen content. The absolute oxygen stoichiometry 3- δ at the equilibrated high temperature state was presumed to be that given by the oxygen content profiles in Figure 5.2, and the mass differences were then used to determine the absolute oxygen stoichiometry 3- δ of the unquenched and quenched states. The entire sequence above was repeated for each of the six pellets. Different oxygen stoichiometries were obtained for each pellet by using different temperatures and oxygen partial pressures for the high temperature equilibration step, and a slower cooling rate of 1°C/min was used for one pellet. After 25 days, one of the pellets (labeled as pellet #1 below) was subject to the same quenching sequence, to verify that the quenching process is repeatable and to verify that the pellets were indeed quenched, *i.e.*, not exchanging noticeable amounts of O₂ with

the ambient air at 25°C. Full details of the quenching conditions are provided below along with the results.

6.3.3 Initial characterization

After the above steps, XRD patterns were measured from each pellet. The six pellets were then embedded together in epoxy with graphite filler (Buehler 20-8128-032 resin, 20-8128-008 hardener, 20-8500 conductive filler) to ensure they were processed identically in subsequent steps. The pellet surfaces were kept exposed, and the pellets were not warmed to any noticeable extent by the epoxy hardening reaction. The epoxy-embedded pellets (hereafter referred to as just 'the pellets') were polished down to 0.3 μm grit using alumina powders (Allied High Tech Products), and cleaned in an ultrasonic bath.

Electron microprobe analysis (EPMA, JEOL JXA-8200) was employed for chemical analysis using SrTiO₃, Co, and Nb standards. A carbon coater (Cressington 108) was used to coat the pellets with ~ 30 nm carbon before the EPMA measurement. The relative cation amounts measured were converted into a chemical formula by assuming no Sr interstitials or Sr vacancies were present. The measured formula (applicable for all 6 pellets) was SrCo_{0.91 \pm 0.01}Nb_{0.09 \pm 0.01}O_{3- δ} , matching the nominal composition within the error of the measurement. Micrographs taken using the same instrument suggested that the compacts were $\sim 50\%$ porous. The carbon coating was polished off after the measurements (again with wet sandpaper and then successive alumina grit sizes down to 0.3 μm), and the pellets were again sonicated in isopropanol.

X-ray photoelectron spectroscopy (XPS, Surface Science Instruments, model M-Probe) was used to acquire niobium 3d_{3/2-5/2} and cobalt 2p_{1/2-3/2} spectra from several pellets. The analyzed area of the samples was 250 μm x 1000 μm . Due to offgassing from the epoxy, the vacuum chamber took unusually long to pump down (many hours), reaching a pressure in the analysis chamber of 3e-8 torr and leading to somewhat reduced count rates. The binding energy scale was calibrated from the carbon contamination using the C 1s peak at 285.0 eV. The pellets were briefly polished shortly before the spectra were taken.

Three months later, none of the pellets had changed color, but nevertheless the pellets were again polished from 240 grit down to 0.3 μm in preparation for the x-ray absorption measurements described below, which took place a few days later. The color of the pellets did not change as a result of this polishing. XRD patterns were retaken to verify that the pellets retained their original lattice parameter (and by correlation, their original oxygen content).

6.3.4 X-ray absorption spectroscopy

X-ray absorption edges were acquired from each of the six pellets by Tim Fister at the Advanced Photon Source on beamline 20BM with a $400\ \mu\text{m} \times 400\ \mu\text{m}$ toroidally focused beam. For each pellet, scans of the Sr, Co, and Nb K-edges were recorded in fluorescence mode. SrO_2 , Co, and Nb standards were measured in transmission mode to provide an energy reference. The background was subtracted and the data normalized. No correction was made for self-absorption.

6.3.5 Non-resonant inelastic x-ray scattering

Non-resonant inelastic x-ray scattering (NRIXS) experiments were performed by the author using the LERIX end-station⁷⁹ at the PNC/XOR insertion device, beamline 20-ID, at the Advanced Photon Source. The experimental setup is shown in Figure 6.1 and Figure 6.2. Guidance in acquiring and analyzing the data was provided by Tim Fister, Kee-Chul Chang, and the staff at beamline 20, especially Mali Balasubramanian. Toroidal focusing of the x-ray beam from the silicon (111) double-crystal monochromator was performed, giving $\sim 10^{13}$ photons/s incident on the samples over a $\sim 1\ \text{mm}$ spot size. The LERIX instrument was configured to have a full array of 19 spherically-bent silicon (555) crystal analyzers able to independently measure scattered photon intensities with momentum transfers ranging from $0.8\ \text{\AA}^{-1}$ to $10.1\ \text{\AA}^{-1}$. Lead tape was applied to portions of the detector slits to reduce the background noise to 10-50 counts/s on all detectors. The oxygen K edge shape was observed to be independent of momentum, similar to what has been found for other oxides, enabling integration over all detectors. The spectra at higher momentum had reduced count rates, however, so the signal-to-noise ratio was improved by integrating only over detectors 4 through 11 ($3.1\ \text{\AA} - 7.7\ \text{\AA}$). The measurements had an energy resolution of $\sim 1.3\ \text{eV}$.

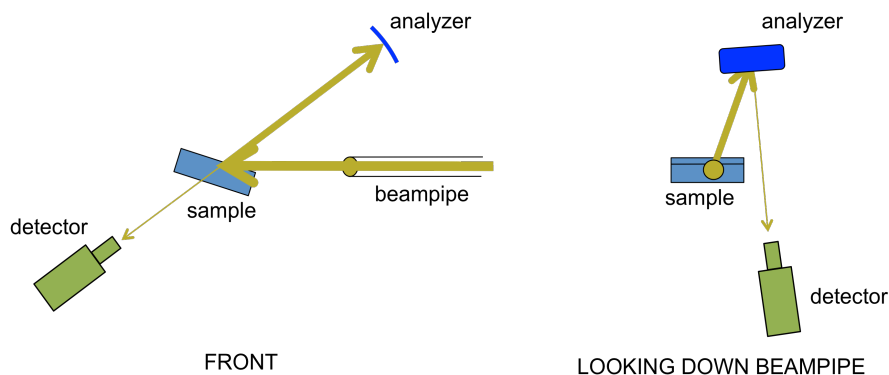


Figure 6.1. Schematic of the beampath in the NRIXS experiment.

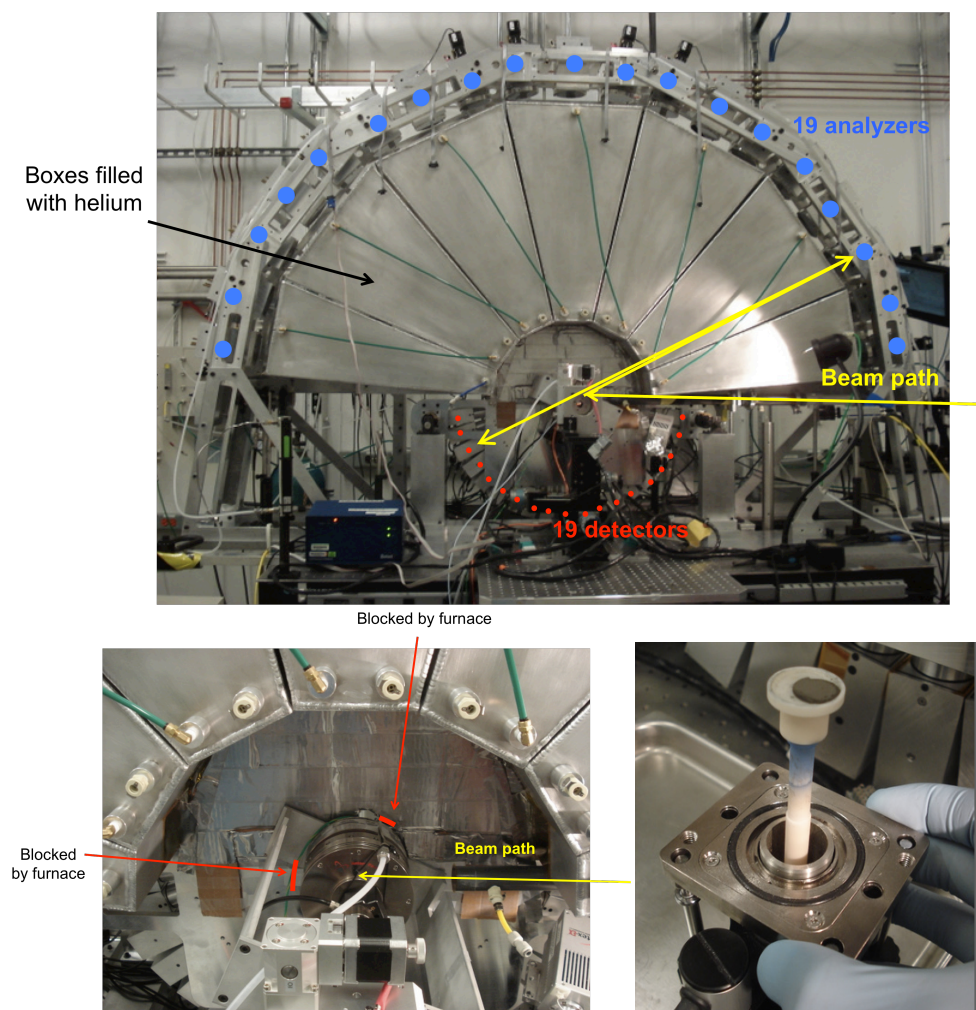


Figure 6.2. The LERIX spectrometer used in the NRIXS measurements and located at Beamline 20-ID at the Advanced Photon Source. Top: Overall configuration. Left: Mounting of the high-temperature chamber during the NRIXS measurement. Right: SCN powder compact used in the measurement, before installation into the high-temperature chamber.

The sample consisted of an unfired powder compact prepared from the SCN powder described above. The powder was pressed uniaxially at 8 tons for 10 min in a 13 mm diameter steel die with no binder or lubricant. The die faces were covered with Kapton tape to avoid contaminating the compact surface during pressing. The resulting compact had no cracks and was ~ 0.5 mm thick. The penetration depth of 10 keV x-rays in dense SCN was calculated to be much less, 25 μm , so the measurement achieved truly bulk-sensitive measurements of SCN with no signal contamination from material underneath the sample.

During the NRIXS measurements, the SCN compact was supported by a shallow alumina cup inside a chamber designed for *in situ* x-ray measurements up to 1200°C (Anton-Paar HTK 1200N) that includes radiative sample heating, high-vacuum-compatible sealing, and x-ray-transparent Kapton-graphite windows. The total pressure in the furnace was 1 atm, and the desired oxygen partial pressures were obtained by flowing pre-mixed gases with the appropriate amounts of O₂ and N₂ through the sample chamber and then, for verification, past a zirconia-based oxygen sensor (Setnag) mounted in a quartz tube in a separate furnace. The *in situ* chamber was mounted such that the x-ray incident angle was 15° relative to the sample surface. This mounting configuration blocked analyzers 1, 2, 3, and 13.

For each condition, the sample was allowed to equilibrate for 1 h - 4 h. These equilibration times were long enough to allow the oxygen content of the metastable cubic phase to stabilize, and short enough such that the very minor extent of phase decomposition could be neglected. The stabilization was verified during the experiment by repeated cobalt K edge scans using a fluorescence detector, as well as prior to the experiment by measurements on analogous samples by TGA, and separately by *in situ* XRD using the same *in situ* chamber. Stabilization was judged to have been reached when enough time had elapsed such that the K edge structure, the mass change, and the diffraction pattern were all constant on a time scale of hours.

After equilibration at each condition, oxygen K, cobalt M₁, and cobalt M_{2,3} scans were acquired for durations of 6 h, 1.5 h, and 1.5 h, along with a survey scan from 9900 eV - 10720 eV to look for anomalous edges (none were observed). To verify repeatability and improve the data quality, the oxygen K edge measurements at 1000°C 1e-4 atm O₂ and 500°C 1 atm O₂ were repeated for another 6 h.

For comparison, additional NRIXS measurements were taken on an unfired powder compact of a second material, La_{0.6}Sr_{0.4}FeO_{3-δ} (LSF 640). The same experimental parameters were used, except for the following: the thickness of the measured compact was ~ 1 mm (as compared to an absorption length of 13 μm), the x-ray incident angle was 10°-12°, and the energy resolution was ~1.7 eV.

6.4 Results and discussion

6.4.1 Quenching

A typical profile from the thermogravimetric pellet quenching is shown in Figure 6.3. Stable mass values (drift < 20 μg/h) were reached for all pellets, both during the high temperature equilibration step and after the low temperature quenching.

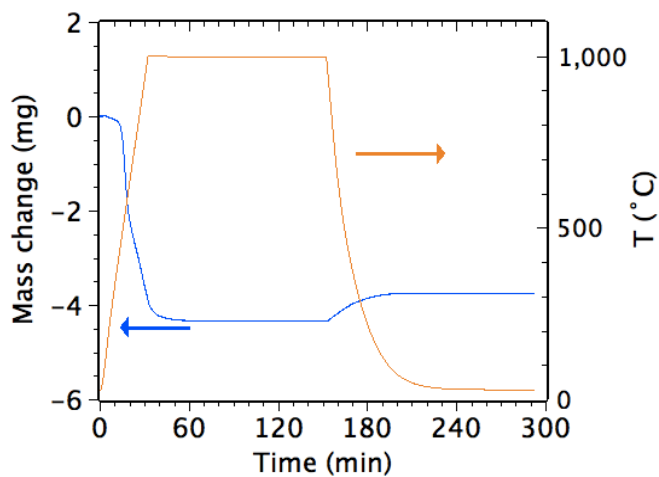


Figure 6.3. Typical mass profile of an SCN pellet equilibrated in the TGA at high temperature and then quenched. See pellet #5 in Table 6.1 for processing parameters.

The equilibration temperatures, oxygen partial pressures, and cooling rates that were used are summarized in Table 6.1, along with the calculated values for the initial, equilibrium, and final oxygen stoichiometries of the quenched pellet. The precision of the measurements is supported by the fact that the measured initial $3-\delta$ values were identical for all six pellets, which is expected since the pellets were all cut from same larger pellet. Pellet 1 was quenched twice; column 1a corresponds to the first quenching, column 1b to the second quenching performed 21 days later. For this pellet, the final $3-\delta$ measured in the first quenching run precisely matched the initial $3-\delta$ measured in the second run, providing further evidence that the measurements are repeatable and precise, and that the pellet oxygen exchange kinetics are truly quenched.

pellet #	3	2	4	6	1a	1b	5
T (°C)	400	700	800	850	900	900	1000
PO ₂ (atm)	1	1E-01	5E-03	3E-03	1E-03	1E-03	3E-04
cooling rate (°C/min)	1	50	50	50	50	50	50
initial 3- δ	2.73	2.73	2.73	2.73	2.73	2.55	2.73
equilibrium 3- δ	2.64	2.62	2.55	2.53	2.51	2.51	2.47
quenched 3-δ	2.79	2.73	2.63	2.60	2.55	2.56	2.51
quenched average Co valence	3.41	3.30	3.07	3.01	2.90	2.91	2.79
quenched a ₀ (Å)	3.864	3.871	3.890	3.900	3.914	3.911	3.920

Table 6.1. Summary of parameters from the pellet quenching runs.

X-ray diffraction patterns taken from the pellets shortly after quenching are shown in Figure 6.4. They show several reflections indexable to the cubic perovskite phase, and these reflections exhibit a small but noticeable peak shift to lower angles for lower oxygen contents, as expected. Additional low-intensity reflections around 42°, 48.5°, and 64° are increasingly apparent at lower oxygen contents and are not indexable to the cubic perovskite. To check the possibility that these reflections are caused by segregation of a second phase within the host SCN phase, these reflections were compared with XRD patterns found in the Inorganic Crystal Structure Database (ICSD) for several other plausible phases, including SrO, CoO, Co₃O₄, SrCO₃, and all Sr-Co-O compounds listed in the ICSD. No correspondence was observed. Furthermore, these three low-intensity reflections also appear to exhibit a peak shift to lower angles for lower oxygen contents, suggesting that they do not arise from an impurity phase with fixed lattice parameter. Quasi-cubic lattice parameters were extracted from the indexed peaks by the Nelson-Riley method and are included in Table 6.1.

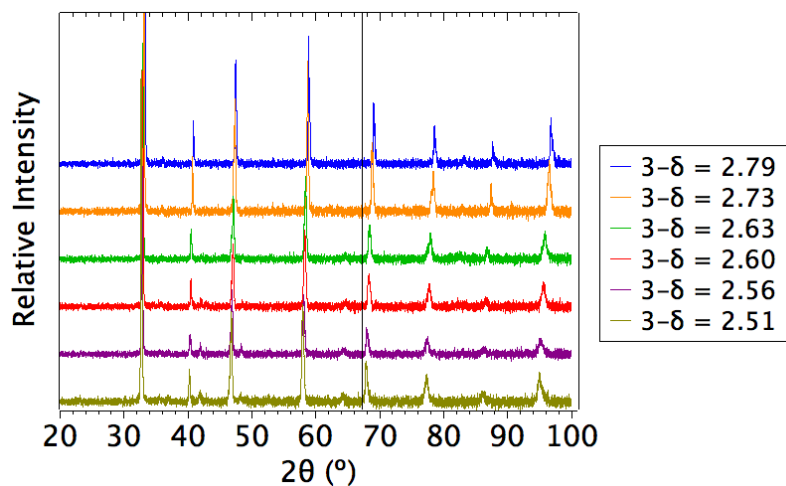


Figure 6.4. XRD patterns taken from the six pellets shortly after quenching. A vertical black line was added at 67° to make the peak shifts between spectra easier to see.

6.4.2 X-ray photoelectron spectra

While the focus in the current study is on the bulk valence behavior, as a brief aside, surface-sensitive x-ray photoelectron spectra (XPS) of the niobium 3d and cobalt 2p edges acquired from the quenched pellets are shown in Figure 6.5. Niobium spectra were only acquired from the lowest and highest oxygen content pellets; cobalt spectra were acquired from all pellets. The cobalt spectrum corresponding to $3-\delta = 2.63$ appeared anomalous and was discarded. No significant change in binding energy, relative intensity, or width is observed between the peaks at different oxygen stoichiometries.

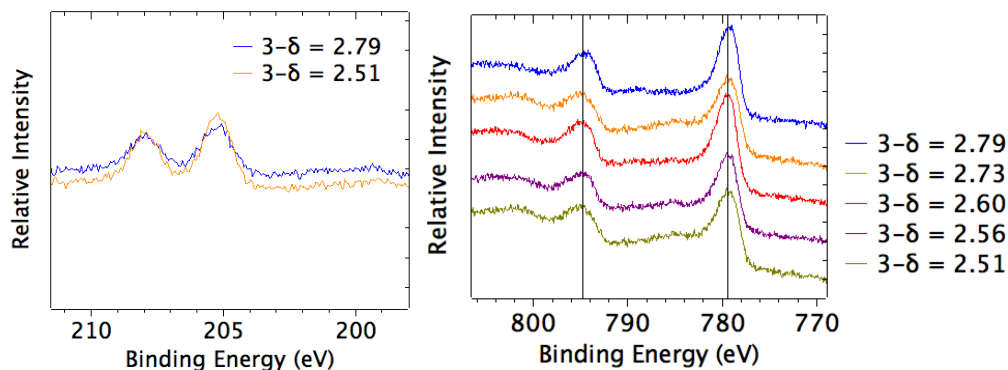


Figure 6.5. X-ray photoelectron spectra measured from SCN quenched pellets with various oxygen stoichiometries $3-\delta$, showing the niobium $3d_{3/2-5/2}$ peaks (left) and cobalt $2p_{1/2-3/2}$ peaks (right).

A similar XPS study was conducted on Li_xCoO_2 samples with the lithium content x varied from 1.0 to 0.0 by electrochemical delithiation.⁸⁰ The cobalt 2p peaks measured in that study were seen to peak at nearly identical binding energies as in the current study, but were somewhat sharper. The authors claimed that "the binding energy and the relative area of the satellite peak [at 790 eV] are a more efficient tool to access the oxidation state of cobalt than the binding energy of the main peak itself". However, the satellite peak seen at 790 eV in the Li_xCoO_2 study is not observed here for SCN. These data indicate that the cobalt 2p XPS spectra are not a sensitive probe of valence in SCN, and may not be for cobalt perovskites in general.

6.4.3 X-ray absorption fine structure

Turning to the x-ray absorption fine structure (XAFS) measurements, since the penetration depth in SCN of x-rays at the energies used is 20 μm - 90 μm , the

measurements are expected to be bulk-sensitive. The K edges of strontium, cobalt, and niobium are shown in Figure 6.6. A key result here is that the niobium and strontium edges show little change over the range of oxygen stoichiometries studied, indicating that those ions are well-approximated as fixed-valent.

On the other hand, the features of the cobalt K edge vary significantly with oxygen content. Specifically, the threshold energy of the cobalt K edges (defined as the energy at which the absorption intensity reaches half its peak value) exhibits a monotonic shift to lower energies upon reduction of SCN. The most reduced pellet has a 2 eV lower threshold energy than the most oxidized pellet.

Decreases in formal oxidation state have long been correlated with edge shifts to lower energy.⁸¹ The correlation may originate from a direct screening effect: an added valence electron screens the final (continuum) state from the positive nucleus more than it does the initial (core) state from the positive nucleus; thus an added valence electron could directly decrease the energy difference between the initial and final states. The correlation may also originate indirectly from bond length changes; an added valence electron increases the average bond length to an ion's nearest neighbors, which increases the electron wavelength (and decreases the energy) at which constructive interference is maximized between the outgoing electron wave and the backscattered wave from the neighbor, and the result is a decrease in the absorption edge energy. As Bunker notes, "it is difficult to experimentally distinguish between the direct correlation (formal-charge --> edge-

shift) and the indirect one (formal-charge --> bond distance --> edge shift)."⁸¹ Thus the shift in threshold energy of the cobalt K edges is a strong indicator of increased electron density in the cobalt-oxygen bond, but the shift cannot tell us whether the electron density is being added to the cobalt, to the oxygen, or to both.

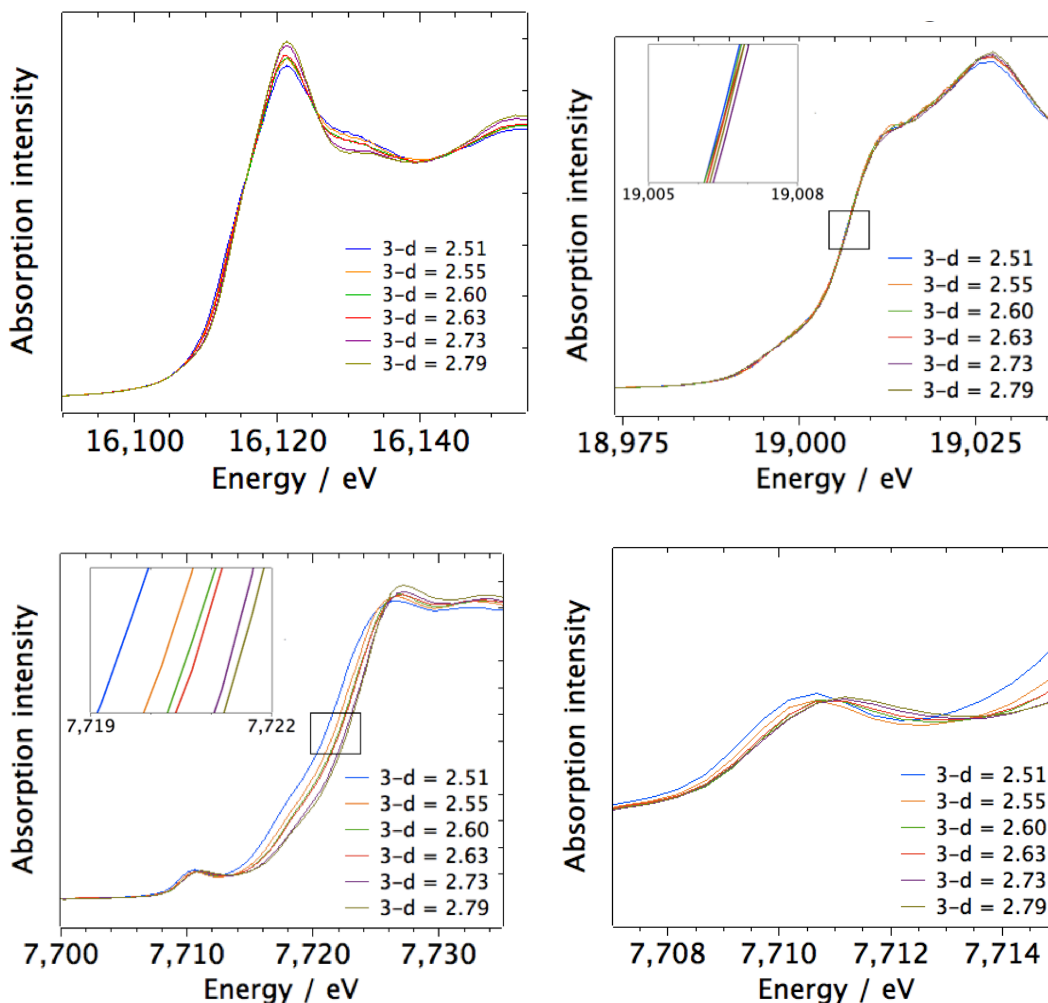


Figure 6.6. Strontium (upper left), niobium (upper right), and cobalt (lower left and right) K edges for SCN pellets quenched with various oxygen stoichiometries. Inset plots show an enlarged view of the edges at threshold.

Although we have not yet been able to extract reliable information from the extended (EXAFS) structure, we measured the quasi-cubic lattice parameter in the quenched pellets to test whether the cobalt edge shifts are associated with bond length changes. The results are shown in Figure 6.7 below. An excellent correlation is observed for all pellets, except for the pellet with the lowest oxygen content. However, a few days after the XANES measurement that pellet was observed to have changed to a darker color, so, on this evidence, we tentatively attribute the high cobalt edge energy in this most highly quenched pellet to a phase instability.

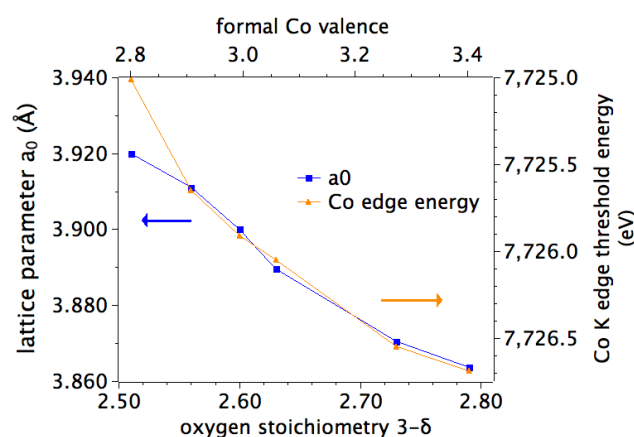


Figure 6.7. Quasi-cubic lattice parameter a_0 and cobalt K edge threshold energy as a function of oxygen stoichiometry.

Note that the cobalt K pre-edge centroid also exhibits a monotonic shift to lower energies upon reduction, by a total of 0.6 eV over the valence range studied here. In iron compounds, the pre-edge centroid energy has been shown to be a clear indicator of valence; essentially, over a wide range of compounds and coordination numbers, the Fe^{2+} centroid energy was found to be consistently $1.4 \text{ eV} \pm 0.1 \text{ eV}$

lower than the Fe^{3+} centroid energy.⁸² An analogous study of Co compounds has not been reported, so here we merely observe that the pre-edge shifts observed for cobalt in SCN are slightly smaller, *e.g.*, 0.6 eV per 0.6 change in formal oxidation state of cobalt in SCN, versus 1.4 eV per 1.0 change in formal oxidation state of iron.

6.4.4 Non-resonant inelastic x-ray scattering

We turn now to the oxygen K edges acquired by NRIXS. In general for a K edge, dipole-allowed final bound states have p orbital symmetry.⁸³ In a purely ionic model for oxygen ions, the configuration is $1s^2 2s^2 2p^6$, the valence shell is fully occupied, there are no unoccupied bound p states, and we would expect to observe no pre-edge beyond perhaps a weak quadrupole-allowed transition. Conversely, substantial oxygen K pre-edge intensity can be related to the extent of covalency, *i.e.*, the extent to which bound states are available owing to a sharing of electron density with neighboring ions.⁸³ For example, in the case that the oxygen 2p states are hybridized with 3d states centered on the neighboring transition metal ions, we expect, in a first approximation, to observe molecular-orbital states of t_{2g} and e_g symmetry separated by a ligand-field splitting. Furthermore, since the t_{2g} orbitals are π -bonded to the oxygen 2p states whereas the e_g orbitals are σ -bonded, if electron density is removed from the covalent bond (*e.g.*, by oxidizing the crystal), it should be removed preferentially from the e_g orbitals, and the ratio $e_g:t_{2g}$ of the peak intensities should increase upon oxidation.

The measured edge structures are shown in Figure 6.8. The pre-edge is indeed two-peaked, and the ratio of the peak intensities increases as predicted from the ligand field model. Additionally, the magnitude of the $e_g:t_{2g}$ peak splitting is seen to be approximately 2.4 eV, a reasonable value that is comparable to peak splittings in transition-metal octahedral complexes determined from optical measurements.⁸³ Taken together, these data are strong evidence that in this compound there is significant metal 3d - oxygen 2p hybridization at high temperatures.

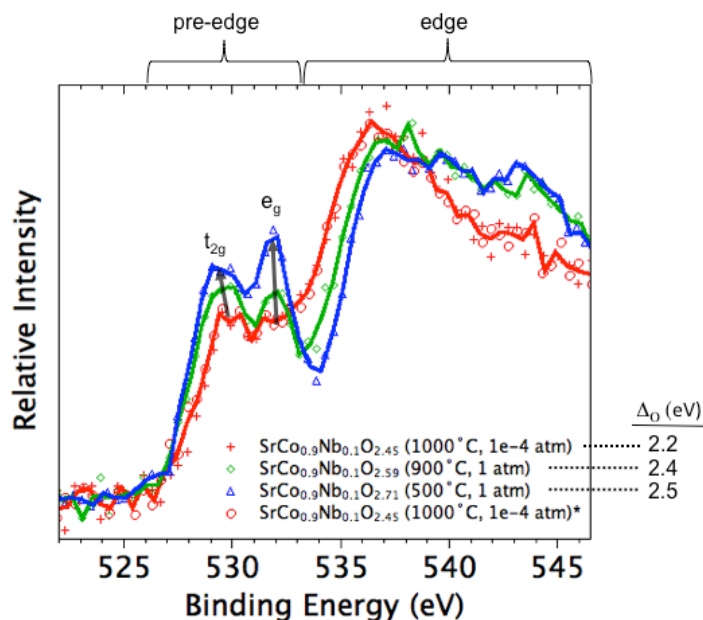


Figure 6.8. Oxygen K edges taken by non-resonant inelastic x-ray scattering (NRIXS) on SCN. Data indicated by circles are a repeat run.

Note that the long penetration length of the hard x-rays used ($\sim 20 \mu\text{m}$ for SCN) and the bulk nature of the sample (particle size $\sim 1 \mu\text{m} - 20 \mu\text{m}$) implies this is a bulk chemical effect. Also note the most reducing condition was measured twice,

before and after the most oxidizing condition, to demonstrate repeatability and rule out irreversible effects like hard x-ray damage.

In Figure 6.9, we compare the quenched cobalt K edges described above with high temperature cobalt K edges that were acquired in the NRIXS experiment. The data quality in the latter edges was unfortunately suboptimal; the fast scan rate resulted in somewhat increased noise, and the energy calibration scans (performed on Co metal foil) were inadvertently not all saved. Nevertheless, a qualitative visual comparison is possible. The green and red curves are cobalt K edges acquired from quenched samples at 25°C; the blue and purple scans are the same edges acquired at 1000°C. In contrast to the large changes in intensity seen in the LSF 640 oxygen K edges shown below, the edge differences evident here are limited to shifting or small changes in intensity of existing features.

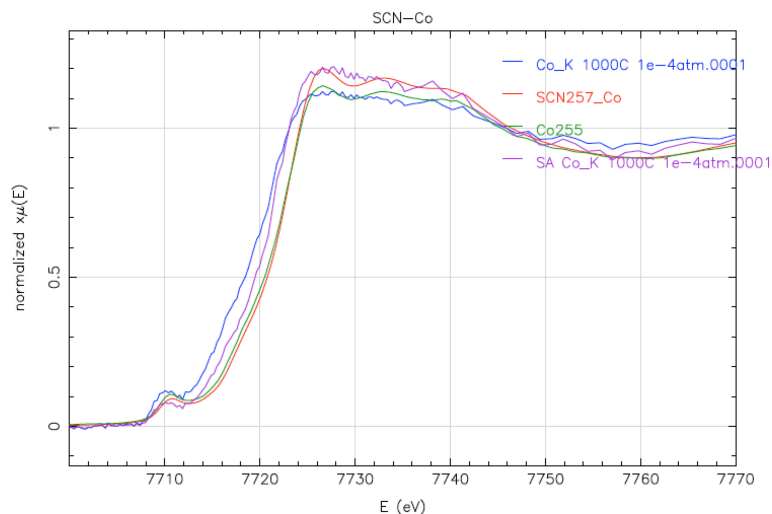


Figure 6.9. Cobalt K edges for SCN taken using XAFS. Green = quenched pellet at 25°C with $3-\delta$ of 2.55, red = quenched powder at 25°C with $3-\delta$ of 2.57, purple/blue = powder compact equilibrated at 1000°C with $3-\delta$ of 2.45.

6.5 Discussion

Most oxides are insulators, with values of electronic conductivity that are orders of magnitude lower than observed in this work for SCN. The above findings suggest the hypothesis that covalent bonding between the Co and O atoms is responsible for the unusually high electronic conductivity and low enthalpy of migration values measured in Chapter 5. The large degree of covalent character in the Co-O bond may also be responsible for the high surface activity. In other words, if oxygen p-orbital character leads to facile electron hopping between atoms already incorporated into the crystal, it may also lead to facile electron hopping onto neutral oxygen atoms that are dissociatively adsorbed on the surface.

To test this hypothesis in future studies, it would be very useful to have a quantitative metric for the degree of covalency. A recent report suggested the possibility of using the integrated intensity under the oxygen K pre-edge as a proxy for the degree of covalency.⁸⁴ An *in situ* ambient pressure XAFS study of oxygen K edges, combined with simultaneously measurements of surface activity, could be a nice test of the possible quantitative correlation between activity and covalency.

6.5.1 Appendix: $\text{La}_{0.6}\text{Sr}_{0.4}\text{FeO}_{3-\delta}$

Oxygen K edge spectra acquired by NRIXS from an LSF 640 powder compact are shown in Figure 6.10. Although the signal-to-noise ratio and energy resolution are not good enough to resolve the pre-edge structure in detail, the overall trends are clear. The structure can be separated into three regions: pre-edge at 528 eV - 533 eV, a "threshold peak" at 533 eV - 539 eV, and an additional peak at 539 eV - 546 eV. Previous literature⁸⁵ supports the assignment of these three regions as follows: pre-edge is primarily bound Fe 3d character with some O p character, threshold is primarily La 5d and Sr 4d character with some O p character, and the additional peak is primarily O p character.

Remarkably, the pre-edge intensity grows substantially upon cooling from 500°C to 25°C, suggesting a significant increase in the degree of covalency. This trend appears to originate purely from thermal contraction of the lattice, since thermogravimetry confirmed that the oxygen stoichiometry was virtually unchanged from the cooling. A Mössbauer spectrum taken on powder cooled in identical manner shows no evidence of magnetic ordering (Figure 6.11). A spin-state transition upon cooling is possible, however. In any case, this substantial change between the equilibrium and quenched conditions underscores the importance of *in situ* studies of such materials.

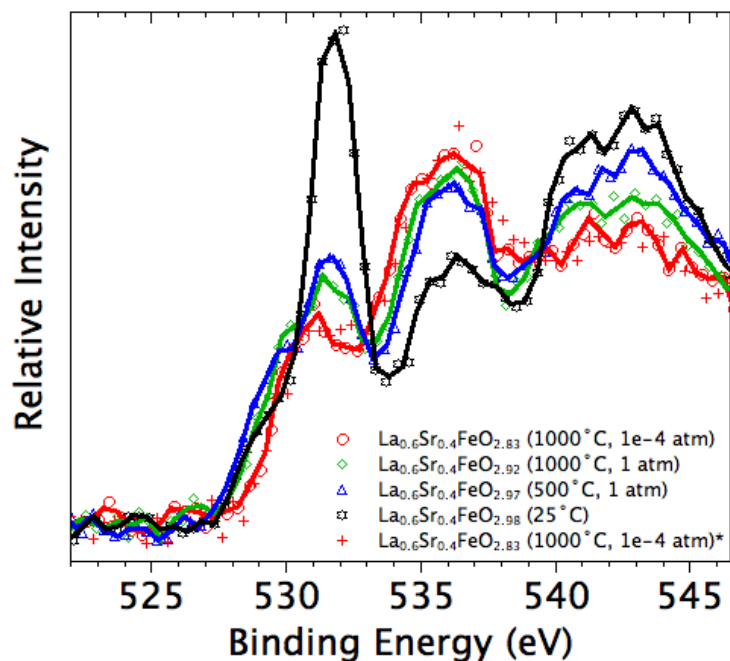


Figure 6.10. Oxygen K edges acquired from $\text{La}_{0.6}\text{Sr}_{0.4}\text{FeO}_{3-\delta}$ by non-resonant inelastic x-ray scattering (NRIXS). Oxygen stoichiometries listed in the legend were calculated from literature data⁸⁶ and in-house thermogravimetry.

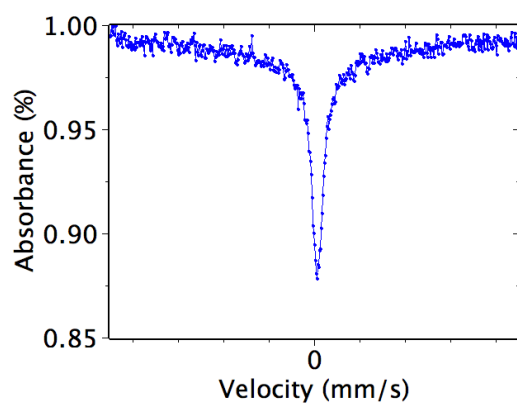


Figure 6.11. ^{57}Fe Mössbauer spectrum from $\text{La}_{0.6}\text{Sr}_{0.4}\text{FeO}_{2.98}$ powder at 25°C.

References

- 1 Singhal, S. C. & Kendall, K. High Temperature Solid Oxide Fuel Cells. *Elsevier*, 1-22 (2003).
- 2 Fuel Cell Handbook, Seventh Edition. *U.S. Department of Energy* (2004).
- 3 Adler, S. Factors governing oxygen reduction in solid oxide fuel cell cathodes. *Chemical reviews* (2004).
- 4 Kuklja, M. M., Kotomin, E. A., Merkle, R., Mastrikov, Y. A. & Maier, J. Combined theoretical and experimental analysis of processes determining cathode performance in solid oxide fuel cells. *Physical Chemistry Chemical Physics* **15**, 5443-5471, doi:Doi 10.1039/C3cp44363a (2013).
- 5 Chueh, W. C. & Haile, S. M. Electrochemistry of Mixed Oxygen Ion and Electron Conducting Electrodes in Solid Electrolyte Cells. *Annu Rev Chem Biomol* **3**, 313-341, doi:Doi 10.1146/Annurev-Chembioeng-073009-101000 (2012).
- 6 Bessler, W. G. *et al.* Model anodes and anode models for understanding the mechanism of hydrogen oxidation in solid oxide fuel cells. *Physical Chemistry Chemical Physics* **12**, 13888-13903, doi:Doi 10.1039/C0cp00541j (2010).
- 7 Adler, S. B. Reference Electrode Placement in Thin Solid Electrolytes. *Journal of the Electrochemical Society* **149**, E166-E172 (2002).
- 8 Sasaki, K. A., Hao, Y. & Haile, S. M. Geometrically asymmetric electrodes for probing electrochemical reaction kinetics: a case study of hydrogen at the Pt-C₅H₂PO₄ interface. *Physical Chemistry Chemical Physics* **11**, 8349-8357 (2009).
- 9 Brichzin, V., Fleig, J., Habermeier, H. U. & Maier, J. Geometry dependence of cathode polarization in solid oxide fuel cells investigated by defined Sr-doped LaMnO₃ microelectrodes. *Electrochem Solid St* **3**, 403-406, doi:Doi 10.1149/1.1391160 (2000).
- 10 Fleig, J., Kim, H. R., Jamnik, J. & Maier, J. Oxygen Reduction Kinetics of Lanthanum Manganite (LSM) Model Cathodes: Partial Pressure Dependence and Rate-Limiting Steps. *Fuel Cells* **8**, 330-337, doi:Doi 10.1002/Fuce.200800025 (2008).
- 11 la O', G. J. *et al.* Catalytic Activity Enhancement for Oxygen Reduction on Epitaxial Perovskite Thin Films for Solid-Oxide Fuel Cells. *Angew Chem Int Edit* **49**, 5344-5347, doi:Doi 10.1002/Anie.201001922 (2010).
- 12 De Souza, R. A. & Kilner, J. A. Oxygen transport in La_{1-x}Sr_xMn_{1-y}Co_yO₃ +/- delta perovskites part II. Oxygen surface exchange. *Solid State Ionics* **126**, 153-161, doi:Doi 10.1016/S0167-2738(99)00228-3 (1999).
- 13 Wang, L., Merkle, R. & Maier, J. Surface Kinetics and Mechanism of Oxygen Incorporation Into Ba_{1-x}Sr_xCo_yFe_{1-y}O₃-delta SOFC Microelectrodes. *Journal of the Electrochemical Society* **157**, B1802-B1808, doi:Doi 10.1149/1.3494224 (2010).

- 14 Jung, W. & Tuller, H. L. A New Model Describing Solid Oxide Fuel Cell Cathode Kinetics: Model Thin Film SrTi_{1-x}Fe_xO_{3-d} Mixed Conducting Oxides—a Case Study. *Adv. Energy Mater.* **1**, 1184-1191, doi:10.1002/aenm.201100164 (2011).
- 15 Wedig, A., Lynch, M. E., Merkle, R., Maier, J. & Liu, M. Sheet Resistance in Thin Film Solid Oxide Fuel Cell Model Cathodes: A Case Study on Circular Bi_{1-x}Sr_xFeO_{3-δ} Microelectrodes. *Ionic and Mixed Conducting Ceramics* **8** **45**, 213-224, doi:10.1149/1.3701311 (2012).
- 16 Nagai, T., Ito, W. & Sakon, T. Relationship between cation substitution and stability of perovskite structure in SrCoO_{3-δ}-based mixed conductors. *Solid State Ionics* **177**, 3433-3444, doi:10.1016/j.ssi.2006.10.022 (2007).
- 17 Zhou, W., Shao, Z., Ran, R., Jin, W. & Xu, N. A novel efficient oxide electrode for electrocatalytic oxygen reduction at 400–600 °C. *Chem. Commun.*, 5791, doi:10.1039/b813327a (2008).
- 18 Usiskin, R. E. & Haile, S. M. *to be published*.
- 19 Brichzin, V., Fleig, J., Habermeier, H. U., Cristiani, G. & Maier, J. The geometry dependence of the polarization resistance of Sr-doped LaMnO₃ microelectrodes on yttria-stabilized zirconia. *Solid State Ionics* **152**, 499-507, doi:10.1016/S0167-2738(02)00379-X (2002).
- 20 Ioroi, T., Hara, T., Uchimoto, Y., Ogumi, Z. & Takehara, Z. Preparation of perovskite-type La_{1-x}Sr_xMnO₃ films by vapor-phase processes and their electrochemical properties. *Journal of the Electrochemical Society* **144**, 1362-1370, doi:10.1149/1.1837597 (1997).
- 21 Koep, E., Mebane, D. S., Das, R., Compson, C. & Liu, M. L. Characteristic thickness for a dense La_{0.8}Sr_{0.2}MnO₃ electrode. *Electrochem Solid St* **8**, A592-A595, doi:10.1149/1.2050607 (2005).
- 22 la O', G. J. & Shao-Horn, Y. Thickness Dependence of Oxygen Reduction Reaction Kinetics on Strontium-Substituted Lanthanum Manganese Perovskite Thin-Film Microelectrodes. *Electrochem Solid St* **12**, B82-B85, doi:10.1149/1.3095681 (2009).
- 23 la O', G. J., Yildiz, B., McEuen, S. & Shao-Horn, Y. Probing oxygen reduction reaction kinetics of Sr-doped LaMnO₃ supported on Y₂O₃-stabilized ZrO₂. *Journal of the Electrochemical Society* **154**, B427-B438, doi:10.1149/1.2508887 (2007).
- 24 Jung, W., Dereux, J. O., Chueh, W. C., Hao, Y. & Haile, S. M. High electrode activity of nanostructured, columnar ceria films for solid oxide fuel cells. *Energy Environ. Sci.* **5**, 8682-8689, doi:10.1039/C2ee22151a (2012).
- 25 Ferguson, J. D., Arikian, G., Dale, D. S., Woll, A. R. & Brock, J. D. Measurements of Surface Diffusivity and Coarsening during Pulsed Laser Deposition. *Phys Rev Lett* **103**, doi:10.1103/Physrevlett.103.256103 (2009).
- 26 Lai, W. & Haile, S. M. Impedance Spectroscopy as a Tool for Chemical and Electrochemical Analysis of Mixed Conductors: A Case Study of Ceria. *J*

- American Ceramic Society* **88**, 2979-2997, doi:10.1111/j.1551-2916.2005.00740.x (2005).
- 27 Jamnik, J. & Maier, J. Treatment of the impedance of mixed conductors - Equivalent circuit model and explicit approximate solutions. *Journal of the Electrochemical Society* **146**, 4183-4188, doi:Doi 10.1149/1.1392611 (1999).
- 28 Newman, J. Resistance for Flow of Current to a Disk. *Journal of the Electrochemical Society* **113**, 501-&, doi:Doi 10.1149/1.2424003 (1966).
- 29 Bak, T., Nowotny, J., Rekas, M., Sorrell, C. C. & Vance, E. R. A manometric method for the determination of chemical diffusion in non-stoichiometric oxides: Example of (La,Sr)MnO₃. *Solid State Ionics* **135**, 557-561, doi:Doi 10.1016/S0167-2738(00)00636-6 (2000).
- 30 Mizusaki, J. *et al.* Oxygen nonstoichiometry and defect equilibrium in the perovskite-type oxides La_{1-x}Sr_xMnO_{3+d}. *Solid State Ionics* **129**, 163-177, doi:Doi 10.1016/S0167-2738(99)00323-9 (2000).
- 31 De Souza, R. A., Kilner, J. A. & Walker, J. F. A SIMS study of oxygen tracer diffusion and surface exchange in La_{0.8}Sr_{0.2}MnO_{3+delta}. *Materials Letters* **43**, 43-52, doi:Doi 10.1016/S0167-577x(99)00228-1 (2000).
- 32 Jiang, S. P. & Love, J. G. Origin of the initial polarization behavior of Sr-doped LaMnO₃ for O₂ reduction in solid oxide fuel cells. *Solid State Ionics* **138**, 183-190, doi:Doi 10.1016/S0167-2738(00)00806-7 (2001).
- 33 Cai, Z. H., Kubicek, M., Fleig, J. & Yildiz, B. Chemical Heterogeneities on La_{0.6}Sr_{0.4}CoO_{3-delta} Thin Films-Correlations to Cathode Surface Activity and Stability. *Chemistry of Materials* **24**, 1116-1127, doi:Doi 10.1021/Cm203501u (2012).
- 34 Chueh, W. C., Hao, Y., Jung, W. & Haile, S. M. High electrochemical activity of the oxide phase in model ceria-Pt and ceria-Ni composite anodes. *Nature Materials* **11**, 155-161, doi:Doi 10.1038/Nmat3184 (2012).
- 35 Opitz, A. K. & Fleig, J. Investigation of O₂ reduction on Pt/YSZ by means of thin film microelectrodes: The geometry dependence of the electrode impedance. *Solid State Ionics* **181**, 684-693, doi:Doi 10.1016/J.Ssi.2010.03.017 (2010).
- 36 Ahlgren, E. O. & Poulsen, F. W. Thermoelectric power of stabilized zirconia. *Solid State Ionics* **82**, 193-201, doi:Doi 10.1016/0167-2738(95)00201-3 (1995).
- 37 Shao, Z. & Haile, S. M. A high-performance cathode for the next generation of solid-oxide fuel cells. *Nature* **431**, 170-173 (2004).
- 38 Lee, J. G., Park, J. H. & Shul, Y. G. Tailoring gadolinium-doped ceria-based solid oxide fuel cells to achieve 2 W cm⁻² at 550 °C. *Nat Commun* **5**, doi:10.1038/ncomms5045 (2014).
- 39 Yan, J. W., Enoki, M., Matsumoto, H. & Ishihara, T. An intermediate temperature solid oxide fuel cell using a La(Sr)Ga(Mg)O₃ thin film prepared by pulsed laser deposition as electrolyte. *Electrochemistry* **73**, 945-950 (2005).

- 40 Han, F. *et al.* Novel high-performance solid oxide fuel cells with bulk ionic conductance dominated thin-film electrolytes. *Journal of Power Sources* **218**, 157-162, doi:Doi 10.1016/J.jpowsour.2012.06.087 (2012).
- 41 Park, S., Choi, S., Shin, J. & Kim, G. A collaborative study of sintering and composite effects for a PrBa_{0.5}Sr_{0.5}Co_{1.5}Fe_{0.5}O_{5+delta} IT-SOFC cathode. *Rsc Adv* **4**, 1775-1781, doi:Doi 10.1039/C3ra45296d (2014).
- 42 Zhu, Y. L. *et al.* An A-Site-Deficient Perovskite offers High Activity and Stability for Low-Temperature Solid-Oxide Fuel Cells. *Chemsuschem* **6**, 2249-2254, doi:Doi 10.1002/Cssc.201300694 (2013).
- 43 Ahn, J. S. *et al.* High-performance bilayered electrolyte intermediate temperature solid oxide fuel cells. *Electrochemistry Communications* **11**, 1504-1507, doi:Doi 10.1016/J.Elecom.2009.05.041 (2009).
- 44 Baumann, F. S. *et al.* Quantitative comparison of mixed conducting SOFC cathode materials by means of thin film model electrodes. *Journal of the Electrochemical Society* **154**, B931-B941, doi:10.1149/1.2752974 (2007).
- 45 Baumann, F., Fleig, J., Habermeier, H. & Maier, J. Impedance spectroscopic study on well-defined (La, Sr)(Co, Fe) O_{3-δ} model electrodes. *Solid State Ionics* **177**, 1071-1081 (2006).
- 46 Baumann, F., Fleig, J., Habermeier, H. & Maier, J. Ba_{0.5}Sr_{0.5}Co_{0.8}Fe_{0.2}O_{3-δ} thin film microelectrodes investigated by impedance spectroscopy. *Solid State Ionics* **177**, 3187-3191 (2006).
- 47 Crumlin, E. J. *et al.* Oxygen Reduction Kinetics Enhancement on a Heterostructured Oxide Surface for Solid Oxide Fuel Cells. *J Phys Chem Lett* **1**, 3149-3155, doi:Doi 10.1021/Jz101217d (2010).
- 48 Mutoro, E., Crumlin, E. J., Biegalski, M. D., Christen, H. M. & Shao-Horn, Y. Enhanced oxygen reduction activity on surface-decorated perovskite thin films for solid oxide fuel cells. *Energy Environ. Sci.* **4**, 3689-3696, doi:Doi 10.1039/C1ee01245b (2011).
- 49 Wang, L., Merkle, R., Maier, J., Acarturk, T. & Starke, U. Oxygen tracer diffusion in dense Ba_{0.5}Sr_{0.5}Co_{0.8}Fe_{0.2}O_{3-delta} films. *Applied Physics Letters* **94**, doi:Artn 071908
Doi 10.1063/1.3085969 (2009).
- 50 Kawada, T. *et al.* Determination of oxygen vacancy concentration in a thin film of La_{0.6}Sr_{0.4}CoO_{3-delta} by an electrochemical method. *Journal of the Electrochemical Society* **149**, E252-E259, doi:Doi 10.1149/1.1479728 (2002).
- 51 Jacobson, A. J. Materials for Solid Oxide Fuel Cells. *Chemistry of Materials* **22**, 660-674, doi:Doi 10.1021/Cm902640j (2010).
- 52 Sun, C. W., Hui, R. & Roller, J. Cathode materials for solid oxide fuel cells: a review. *Journal of Solid State Electrochemistry* **14**, 1125-1144, doi:Doi 10.1007/S10008-009-0932-0 (2010).
- 53 Verkerk, M. J., Hammink, M. W. J. & Burggraaf, A. J. Oxygen-Transfer on Substituted ZrO₂, Bi₂O₃, and CeO₂ Electrolytes with Platinum-Electrodes .1. Electrode Resistance by Dc Polarization. *Journal of the Electrochemical Society* **130**, 70-78, doi:Doi 10.1149/1.2119686 (1983).

- 54 Dumélié, M., Nowogrocki, G. & Boivin, J. C. Ionic conductor membrane for oxygen separation. *Solid State Ionics* **28–30, Part 1**, 524-528, doi:[http://dx.doi.org/10.1016/S0167-2738\(88\)80095-X](http://dx.doi.org/10.1016/S0167-2738(88)80095-X) (1988).
- 55 Takahashi, T., Iwahara, H. & Esaka, T. High Oxide Ion Conduction in Sintered Oxide of System Bi₂O₃-M₂O₅. *Journal of the Electrochemical Society* **124**, 1563-1569, doi:Doi 10.1149/1.2133111 (1977).
- 56 Takahashi, T., Iwahara, H. & Arao, T. High Oxide Ion Conduction in Sintered Oxides of System Bi₂O₃-Y₂O₃. *J Appl Electrochem* **5**, 187-195, doi:Doi 10.1007/Bf01637268 (1975).
- 57 Boivin, J. C. & Mairesse, G. Recent material developments in fast oxide ion conductors. *Chemistry of Materials* **10**, 2870-2888, doi:Doi 10.1021/Cm980236q (1998).
- 58 Fister, T. T. *et al.* In situ characterization of strontium surface segregation in epitaxial La_{0.7}Sr_{0.3}MnO₃ thin films as a function of oxygen partial pressure. *Appl. Phys. Lett.* **93**, 151904, doi:10.1063/1.2987731 (2008).
- 59 Mizusaki, J., Mima, Y., Yamauchi, S., Fueki, K. & Tagawa, H. Nonstoichiometry of the perovskite-type oxides La_{1-x}Sr_xCoO_{3-δ}. *Journal of Solid State Chemistry* **80**, 102-111 (1989).
- 60 Koinuma, H. & Takeuchi, I. Combinatorial solid-state chemistry of inorganic materials. *Nature Materials* **3**, 429-438, doi:Doi 10.1038/Nmat1157 (2004).
- 61 Švarcová, S., Wiik, K., Tolchard, J., Bouwmeester, H. & Grande, T. Structural instability of cubic perovskite Ba_xSr_{1-x}Co_{1-y}Fe_yO_{3-δ}. *Solid State Ionics* **178**, 1787-1791 (2008).
- 62 Mueller, D. N. *et al.* A kinetic study of the decomposition of the cubic perovskite-type oxide Ba_xSr_{1-x}Co_{0.8}Fe_{0.2}O_{3-δ} (BSCF) (x=0.1 and 0.5). *Phys Chem Chem Phys* **12**, 10320-10328, doi:10.1039/c0cp00004c (2010).
- 63 Kriegel, R., Kircheisen, R. & Töpfer, J. Oxygen stoichiometry and expansion behavior of Ba_{0.5}Sr_{0.5}Co_{0.8}Fe_{0.2}O_{3-δ}. *Solid State Ionics* **181**, 64-70, doi:10.1016/j.ssi.2009.11.012 (2010).
- 64 Arnold, M., Gesing, T. & Martynczuk, J. Correlation of the Formation and the Decomposition Process of the BSCF Perovskite at *Chemistry of Materials* (2008).
- 65 Nelson, J. B. & Riley, D. P. AN EXPERIMENTAL INVESTIGATION OF EXTRAPOLATION METHODS IN THE DERIVATION OF ACCURATE UNIT-CELL DIMENSIONS OF CRYSTALS. *Proceedings of the Physical Society of London* **57**, 160-177, doi:10.1088/0959-5309/57/3/302 (1945).
- 66 Harrison, W. T. A., Hegwood, S. L. & Jacobson, A. J. A Powder Neutron-Diffraction Determination of the Structure of Sr₆Co₅O₁₅, Formerly Described as the Low-Temperature Hexagonal Form of SrCoO_{3-X}. *J Chem Soc Chem Comm*, 1953-1954, doi:Doi 10.1039/C39950001953 (1995).
- 67 Bucher, E., Egger, A., Ried, P., Sitte, W. & Holtappels, P. Oxygen nonstoichiometry and exchange kinetics of Ba_{0.5}Sr_{0.5}Co_{0.8}Fe_{0.2}O_{3-δ}. *Solid State Ionics* **179**, 1032-1035 (2008).

- 68 McIntosh, S., Vente, J., Haije, W., Blank, D. & Bouwmeester, H. Oxygen stoichiometry and chemical expansion of $\text{Ba}_{0.5}\text{Sr}_{0.5}\text{Co}_{0.8}\text{Fe}_{0.2}\text{O}_{3-\delta}$ measured by in situ neutron diffraction. *Chemistry of Materials* **18**, 2187-2193 (2006).
- 69 Mueller, D. N., De Souza, R. A., Yoo, H. I. & Martin, M. Phase Stability and Oxygen Nonstoichiometry of Highly Oxygen-Deficient Perovskite-Type Oxides: A Case Study of $(\text{Ba,Sr})(\text{Co,Fe})\text{O}_{3-\delta}$. *Chemistry of Materials* **24**, 269-274, doi:10.1021/cm2033004 (2012).
- 70 Yang, Z. & Lin, Y. A semi-empirical equation for oxygen nonstoichiometry of perovskite-type ceramics. *Solid State Ionics* **150**, 245-254 (2002).
- 71 Liu, L., Lee, T., Qiu, L., Yang, Y. & Jacobson, A. A thermogravimetric study of the phase diagram of strontium cobalt iron oxide, $\text{SrCo}_{0.8}\text{Fe}_{0.2}\text{O}_{3-\delta}$. *Materials Research Bulletin* **31**, 29-35 (1996).
- 72 Zhou, W., Jin, W., Zhu, Z. & Shao, Z. Structural, electrical and electrochemical characterizations of $\text{SrNb}_{0.1}\text{Co}_{0.9}\text{O}_{3-\delta}$; as a cathode of solid oxide fuel cells operating below 600°C. *International Journal of Hydrogen Energy* **35**, 1356-1366, doi:10.1016/j.ijhydene.2009.11.092 (2010).
- 73 Chen, Z., Ran, R., Zhou, W., Shao, Z. & Liu, S. Assessment of $\text{Ba}_{0.5}\text{Sr}_{0.5}\text{Co}_{1-y}\text{Fe}_y\text{O}_{3-\delta}$ ($y=0.0-1.0$) for prospective application as cathode for IT-SOFCs or oxygen permeating membrane. *Electrochimica Acta* **52**, 7343-7351 (2007).
- 74 Yang, Z., Harvey, A. S., Infortuna, A., Schoonman, J. & Gauckler, L. J. Electrical conductivity and defect chemistry of $\text{Ba}_x\text{Sr}_{1-x}\text{Co}_y\text{Fe}_{1-y}\text{O}_{3-\delta}$ perovskites. *Journal of Solid State Electrochemistry* **15**, 277-284, doi:10.1007/s10008-010-1208-4 (2011).
- 75 Tilley, R. J. D. Defect Crystal Chemistry. *Defect Crystal Chemistry*, 128 (1987).
- 76 E.R. Cohen, T. C., J.G. Frey, B. Holmström, K. Kuchitsu, R. Marquardt, I. M., F. Pavese, M. Quack, J. Stohner, & H.L. Strauss, M. T., and A.J. Thor. *Quantities, Units and Symbols in Physical Chemistry, IUPAC Green Book, 3rd Edition, 2nd Printing.* (IUPAC & RSC Publishing, 2008).
- 77 Adler, S. Chemical expansivity of electrochemical ceramics. *J American Ceramic Society* **84**, 2117-2119 (2001).
- 78 Marrocchelli, D., Bishop, S. R., Tuller, H. L., Watson, G. W. & Yildiz, B. Charge localization increases chemical expansion in cerium-based oxides. *Physical Chemistry Chemical Physics* (2012).
- 79 Seidler, G. T., Fister, T. T., Cross, J. O. & Nagle, K. P. The LERIX User Facility. **882**, 911-913, doi:10.1063/1.2644702 (2007).
- 80 Daheron, L. *et al.* Electron transfer mechanisms upon lithium deintercalation from LiCoO_2 to CoO_2 investigated by XPS. *Chemistry of Materials* **20**, 583-590, doi:10.1021/Cm702546s (2008).
- 81 Bunker, G. Introduction to XAFS: A Practical Guide to X-ray Absorption Fine Structure Spectroscopy. (2010).
- 82 Wilke, M., Farges, F., Petit, P. E., Brown, G. E. & Martin, F. Oxidation state and coordination of Fe in minerals: An FeK-XANES spectroscopic study. *Am Mineral* **86**, 714-730 (2001).

- 83 de Groot, F. M. F. *et al.* Oxygen 1s X-Ray-Absorption Edges of Transition-Metal Oxides. *Physical Review B* **40**, 5715-5723, doi:Doi 10.1103/Physrevb.40.5715 (1989).
- 84 Suntivich, J. *et al.* Design principles for oxygen-reduction activity on perovskite oxide catalysts for fuel cells and metal-air batteries. *Nat. Chem.* **3**, 546-550, doi:10.1038/nchem.1069 (2011).
- 85 Abbate, M. *et al.* Controlled-Valence Properties of La_{1-x}Sr_xFeO₃ and La_{1-x}Sr_xMnO₃ Studied by Soft-X-Ray Absorption-Spectroscopy. *Physical Review B* **46**, 4511-4519, doi:Doi 10.1103/Physrevb.46.4511 (1992).
- 86 Mizusaki, J., Yoshihiro, M., Yamauchi, S. & Fueki, K. Thermodynamic quantities and defect equilibrium in the perovskite-type oxide solid solution La_{1-x}Sr_xFeO_{3-δ}. *Journal of Solid State Chemistry* **67** (1987).